Polyelectrolyte stars meet hard planar and curved walls: confinement, demixing, collapse

Inaugural–Dissertation
zur
Erlangung des Doktorgrades der
Mathematisch-Naturwissenschaftlichen Fakultät
der Heinrich-Heine-Universität Düsseldorf

vorgelegt von

MARTIN KONIECZNY

aus Mülheim a. d. Ruhr

Düsseldorf, März 2007

Aus dem Institut für Theoretische Physik II
der Heinrich-Heine-Universität Düsseldorf

Gedruckt mit Genehmigung der
Mathematisch-Naturwissenschaftlichen Fakultät
der Heinrich-Heine-Universität Düsseldorf

Referent:	Prof. Dr. C. N. Likos
1. Koreferent:	Prof. Dr. K.-H. Spatschek
2. Koreferent:	Prof. Dr. C. Dellago (Universität Wien)

Tag der mündlichen Prüfung: 14. Juni 2007

This thesis is based on the following original papers:

Chapter 2

M. Konieczny and C. N. Likos,
Polyelectrolyte stars in planar confinement,
J. Chem. Phys. **124**, 214904 (2006).

M. Konieczny and C. N. Likos,
Computer simulations of polyelectrolyte stars near walls,
Macromol. Symp. **245-246**, 276-286 (2006).

Chapter 3

M. Konieczny and C. N. Likos,
Fluid–fluid demixing transitions in colloid–polyelectrolyte star mixtures,
J. Phys.: Condens. Matter **19**, 076105 (2007).

Chapter 4

M. Konieczny and C. N. Likos,
From sea-urchins to starfishes: controlling the adsorption of star-branched polyelectrolytes on charged walls,
(submitted) (2007).

M. Konieczny, A. Jusufi, and C. N. Likos,
Complexation of polyelectrolyte stars with planar and curved oppositely charged walls,
(in preparation) (2007).

M. Konieczny and C. N. Likos,
Effective interactions between polyelectrolyte stars and oppositely charged substrates,
(in preparation) (2007).

Summary

Polyelectrolyte (PE) stars have emerged as a model of soft colloids interacting by means of electro-steric repulsions, caused by a combination of electrostatic forces acting between the constituent particles and an additional, counterion-induced entropic repulsion. In a first step, we study dilute solutions of such aggregates and confine the geometry by placing the PE-stars within a pair of parallel, flat walls. In this stage, we neglect any additional external forces. We analyze the conformations of PE-stars close to one of the walls and examine the effective star–wall interactions as a function of the center-to-surface distance. Thereto, we employ both extensive monomer-resolved molecular dynamics (MD) simulations and theoretical considerations. In addition to the aforementioned electrostatic-entropic contributions to the repulsive star–wall force akin to the well-understood PE-star–PE-star case, we identify a third, novel mechanism arising from the compression of the stiff PE-chains approaching the wall. This compression effect is a direct consequence of the impenetrable character of the wall.

Based on these effective PE-star–wall interactions, we perform a Derjaguin-type approximation to derive the cross-interactions between PE-stars and hard, spherical colloids of larger diameter. Subsequently, we use the received potentials as an input quantity to an integral equation theory approach, yielding information about the structural and phase behavior of binary PE-star–colloid mixtures. Thereby, the results allow us to investigate in detail the influence of contributions to the PE-star–colloid potentials stemming from chain compression on the possible occurrence of a fluid–fluid demixing transition.

In a third and last step, we enhance the previous models of PE-stars in a slab-like arrangement as well as in the vicinity of curved walls by bringing surface charges onto the substrates. In doing so, we introduce electric fields which favor adsorption of the PE-stars. We perform systematic MD simulation studies of the formed complexes' conformations and analyze quantitatively how these conformations can be tuned by altering characterizing properties of the PE-stars, e.g., the functionality, or the strength of the electric field. We discover a wide range of different morphologies for the PE-stars, depending on the particular choice of parameters. The possibility to precisely and easily steer the configurations renders the adsorbed PE-stars a convenient system for practical applications, e.g., as tunable microlenses.

Zusammenfassung

Polyelektrolyt-Sterne (PE) haben sich als ein geeignetes Modell für Kolloide mit weicher Wechselwirkung erwiesen, wobei diese Wechselwirkung im Wesentlichen durch eine Kombination elektrostatischer Kräfte zwischen den geladenen Monomeren und einer von den Gegenionen vermittelten, entropischen Abstoßung herrührt. Im Rahmen dieser Dissertation untersuchen wir in einem ersten Schritt verdünnte Lösungen solcher mesoskopischer Teilchen, wobei das zur Verfügung stehende Volumen durch zwei parallele, planare Wände begrenzt ist. Zusätzliche externe Kräfte seien dabei zunächst vernachlässigt. Wir analysieren die typischen Konfigurationen der PE-Sterne für kleine Abstände zu einer der Wände mit Hilfe von Molekulardynamik-Simulationen (MD) und eines theoretischen Ansatzes. Weiterhin bestimmen wir unter Verwendung der gleichen Methoden die effektiven Kräfte, die eine Wand auf die geladenen Sternpolymere ausübt, als Funktion des Abstandes zwischen Stern und Wand. Dabei zeigt sich, dass neben den erwarteten elektrostatischen und entropischen Beiträgen analog der bekannten Wechselwirkung zwischen zwei PE-Sternen zusätzlich noch ein völlig neuer Mechanismus zum Tragen kommt. Die Tatsache, dass die Wände undurchdringbar für die Monomere der Arme sind, führt zu deutlichen Kompressionseffekten und einer zusätzlichen, dieser Kompression entgegenwirkenden Abstoßung.

Auf Basis der so gewonnenen Erkenntnisse und mittels einer Derjaguin-artigen Näherung können wir dann die effektive Wechselwirkung zwischen PE-Sternen und harten Kugel mit deutlich größerem Durchmesser herleiten. Im Anschluss dient diese Wechselwirkung als Eingangsgröße für eine Integralgleichungs-Theorie, um so die Struktur und das Phasenverhalten binärer Mischungen von Sternen und Kugeln zu berechnen und insbesondere den Einfluss der genannten Kompressionseffekte auf eine mögliche spontane Entmischung zu ermitteln.

Als dritten und letzten Schritt erweitern wir die vorangegangenen Modelle, indem wir Oberflächenladungen auf den planaren oder gekrümmten Wänden zulassen und somit elektrische Felder einführen, die eine Adsorption der PE-Sterne auf dem jeweiligen Substrat zur Folge haben. Es kommt zu einer Komplexbildung, die wir wiederum im Rahmen von MD-Simulationen systematisch untersuchen. Es zeigt sich, dass eine Vielzahl verschiedener Konformationen der adsorbierten Sterne beobachtet werden kann und dass außerdem eine gezielte Beeinflussung möglich ist, wenn Parameter wie die Funktionalität der Sterne oder die Oberflächenladungsdichte geeignet gewählt werden. Dies ist eine notwendige Voraussetzung für potenzielle Anwendungen, z.B. als Mikrolinsen-Systeme in der Optik.

Contents

Chapter 1

Introduction

Soft matter is a term describing an enormously rich variety of different materials with the common characteristic that they are composed of mesoscopic particles, i.e., molecular aggregates with typical sizes ranging from about 1 nm up to 1 μm. Thereby, these entities are dispersed in a solvent whose constituents are of much smaller extension, i.e., they have atomic dimensions. Soft matter systems are synonymously referred to as complex fluids, colloidal suspensions, or colloidal dispersions [1–4]. Here, the terminology 'colloid' stems from the Greek language, combining the words $\kappa\acute{o}\lambda\lambda\alpha$ (glue) and $\varepsilon\acute{\imath}\delta o\varsigma$ (kind), and goes back to Thomas Graham, a pioneer in this field of research in the second half of the 19th century. Note that, despite the somewhat misleading denotation as complex fluids introduced to explicitly distinguish them from atomic systems, we do not necessarily deal with solutions which are found exclusively in the fluid state. Indeed, although within the framework of the thesis at hand we are mainly interested in the case of solid spherical colloids or more fractal and diffuse objects like polymers (see below) dissolved in liquid solvents, both the disperse phase and the dispersion medium can in principle adopt any of the three possible states of matter. Examples are aerosols (solid or liquid in gas), emulsions (liquid in liquid), or foams (gas in liquid). Dispersions with a solid dispersion phase are also becoming increasingly important, especially within the realm of material science for the design of new composites [1], but this area of research is beyond the scope of conventional soft matter physics.

The reason for the literal softness of soft matter, i.e., the essential property to have a rigidity against applied stress or shear that is several orders of magnitude smaller compared to atomic materials, can be understood by means of the decisive structural length scales. Clearly, these length scales are of mesoscopic order, lying somewhere in-between the microscopic domain and the opposite limit of macroscopic objects as familiar from everyday life. In general, a material is the harder the larger its shear modulus is. As is known, for crystalline phases the shear modulus simply scales as the inverse cube of the typical edge length of an elementary cell

of the lattice[1]. For colloidal crystals, this edge length is three to four orders of magnitude larger compared to their atomic counterparts. Assuming a perfect lattice, we obtain a ratio between the elastic constants of colloidal and atomic systems that is extremely small, namely only 10^{-12} to 10^{-9} [4]. While considerable shear stresses of about 10^{11} dyn/cm^2 must be applied to shear, e.g., a metallic work piece, one can deform or even destroy colloidal solids very easily. For non-crystalline states, the above arguments are obviously not applicable anymore. But in such cases, the softness of complex fluids can be explained in terms of the low particle density or of network-forming configurations of polymeric components mechanically stabilizing the system [4, 5].

In general, complex fluids are of great biological, technical, and industrial relevance. In nature, an abundant number of examples for structures with characteristic length scales in the mesoscopic regime can be found. Viruses, proteins, and DNA are prominent representatives, whereby for the latter two cases charges also come into play. Further soft matter systems are blood, milk, mayonnaise, shaving foam, soap, hair spray, several other cosmetic products, rubber, or ink [1]. In case of paint one makes practical use of the phenomenon of shear thinning, i.e., the non-linear dependence of the viscosity of colloidal dispersions on the shear rate. Special types of mesoscopic molecules with appropriate geometry can be used as viscosity modifiers in modern engine oils. So-called hydrogels can efficiently absorb and store huge amounts of water. In the medical and pharmaceutical sector, charged colloids of specific architecture can be used for drug delivery, for protein encapsulation, and as immobilization agents [6–9]. Besides the mentioned applications plenty others could be added immediately.

In typical soft matter systems there exists a broad span of different length and time scales relevant for the particle species that are involved. From a theoretical point of view, this pronounced asymmetry between large (slow) colloids and small (fast) solvent molecules together with the huge number of (internal) degrees of freedom for the mesoscopic constituents renders a full treatment as a complicated mixture impractical with conventional instruments of statistical mechanics [10, 11] or simulational methods [12–14]. Before being able to apply such tools in order to gain insight into the macroscopic properties of complex fluids, we need to bridge the gap between the microscopic and the mesoscopic regimes. In practice, the complexity is even further increased due to the nearly always occurring polydispersity in size, mass or charge within the different species. In this sense, the task to actually find ways to adequately describe the physics of colloidal dispersions with sufficient accuracy is the fundamental challenge in colloid science. A common and extremely powerful strategy is based on the fact that we are usually interested in the static

[1]This holds since the typical cohesive interaction energies per particle are of the same order for colloidal and atomic crystals and thus become irrelevant for a comparison of their shear moduli [4].

and dynamic behavior of the largest, macromolecular aggregates as a whole only, whereas we do not care about any details concerning the influence of the solvent molecules or the internal structure of the mesoscopic particles, although they indeed play an import role. Thus, we may carry out a so-called coarse graining procedure, whereby we trace out all but the significant degrees of freedom. In doing so, we come to an effective description with only a reduced number of components considered (typically a single one) [4, 15, 16]. All atomistic details are hidden, but they are still included implicitly in an averaged fashion.

Thereby, the definition of a corresponding Hamiltonian for the effective interaction between the large colloids (including all indirect effects mediated by, e.g., smaller species present in the system, solvent molecules, internal degrees of freedom of the colloids, or added salt) beyond their simple, direct interactions can in general be achieved in an exact manner. This holds at least as long as all the many-body terms are included. Approximations are necessary only for practical, but not for intrinsic reasons. Introducing such effective potentials is not only beneficial in simplifying theoretical approaches. It allows for a comparison with experimental results, too, since in experiments one normally also focuses on the measurement of quantities reflecting the static or dynamic properties of the mesoscopic particles only. For the static case, by using refractive index matching techniques in optical microscopy experiments or conveniently adjusting the neutron scattering lengths when performing corresponding measurements, the colloids are visible alone, whereas all remaining constituents play the role of a virtually homogeneous background. Hence, scattering data obtained in this way has to be construed by dint of effective interactions. And when performing experiments to investigate dynamic problems, the small particles' degrees of freedom are almost automatically averaged out due to the remarkable difference in the typical time scales for their rather rapid movement on the one hand and the experimental observation time on the other hand. What can be seen is mainly the colloids' thermal or so-called Brownian motion, induced by frequent random collisions with the smaller solvent molecules [17]. Altogether, these facts clearly support the appropriateness of coarse graining strategies.

Besides their practical importance, colloidal dispersions are of great scientific interest since they exhibit special features rendering them excellent model systems for fundamental research. While for atoms and small molecules the ensuing interactions are determined by the electronic structure and are thus fixed, the effective interactions between colloidal particles can be tuned by changing, e.g., the shape or architecture of the colloids, the solvent, the temperature, or the mixture composition of the solution. In this sense, their properties can be tuned specifically and systematically almost at will [1–3]. Moreover, such systems offer experimental advantages. In addition to scattering techniques, mesoscopic aggregates can also be studied directly in real space, e.g., by confocal microscopy. Furthermore, their dynamical time scales are comparable to experimental ones (see above). Therefore, experiments can

give immediate insight into the real space behavior of complex fluids.

Polymers are a special type of mesoscopic particles which are composed of a large number N of repeating building blocks, called the monomers. These monomers are usually hydrocarbon units, which must interact by means of short-ranged steric repulsions due to Pauli's principle. N is normally referred to as the degree of polymerization. Several different architectures can be realized, the simplest one among them is a linear, chain-like arrangement, where the monomeric segments are attached sequentially to each other. Chemically anchoring f such chains to a colloidal core of finite radius R_{d} gives rise to spherical polymer brushes (SPB's). In the limit in which the brush height R_{s} greatly exceeds R_{d}, one talks about star polymers instead [18, 19]. A lot of work has been performed to understand the properties, conformations, and effective interactions of such star-branched polymers in detail. For good solvent conditions, the effective star–star potential was derived theoretically some time ago [20, 21] and its validity could be verified by means of both computer simulations [22] and scattering experiments [21, 23]. It is ultra-soft and purely repulsive and features a logarithmic shape for overlapping distances followed by an exponentially decaying tail. The softness of the potential can be altered by modifying the number f of polymer chains, also called the functionality: while for small values of f the stars are diffuse objects, they behave like spherical hard colloids in the opposite high-f limit. In this sense, they mark a class of colloidal particles easily allowing for the aforementioned tuning of their mutual effective interactions and can be viewed as an excellent example of soft, tunable colloids. Accordingly, they were found to have an extremely rich and versatile equilibrium and dynamical phase behavior [24].

Polyelectrolytes (PE's) are a special sub-class of polymers [25]. Akin to the latter, they can also adopt various geometries, but in addition they carry ionizable groups along their backbones which dissociate upon dissolution in a polar solvent like, e.g., water, leaving behind polyvalent macroions[2] and corresponding counterions in the solution. The latter assure electroneutrality and screen the electric field induced by the PE's. Thus, from the point of view of fundamental research, they combine aspects from two different parts of soft matter physics: polymer theory and the theory of charged suspensions. The presence of charges and (screened) long-ranged Coulombic interactions between them crucially influences the static and dynamic properties of both isolated PE's and respective solutions. Accordingly, a decisive new parameter emerges, namely the degree of charging (often also referred to as charging fraction) α of the PE's. The vast number of additional phenomena arising in case of PE's of different architecture clearly motivates systematic studies.

Consequently, as for neutral polymer brushes and star polymers, a great deal

[2]We restrict ourselves to the case of macroions carrying charges of the same sign only. We will not consider so-called polyampholites, where both positive and negative charges are present.

of theoretical [26–42] and experimental [43–52] effort has been invested in the recent past in order to qualitatively and quantitatively understand the conformations and the interactions of spherical PE-brushes (SPEB's) and PE-stars. As already suggested, the reasons are many-fold. A distinguishing feature of PE-stars is their ability to absorb the majority of the released counterions into their interior, thereby creating an inhomogeneous cloud of entropically trapped particles that strongly hinders coagulation [26–29, 32–35, 53]. PE's are of great biological relevance, since typical proteins and DNA molecules belong to this class, even though their geometry is not star-branched. Grafted PE-chains can provide an electro-steric barrier against flocculation of the colloidal particles on which the chains are grafted, rendering such systems very interesting from the point of view of colloidal stabilization. Moreover, they can act as control agents for gelation, lubrication and flow behavior. Since PE-stars inherit the neutral stars' property to bridge between ultra-soft and stiff behavior, depending on their functionality, the derivation of the effective interactions between them has again led to their description as soft colloids and to theoretical predictions on their structural and phase behavior with emphasis on crystallization [33, 36, 54] that have received already partial experimental confirmation [55]. Moreover, certain similarities in the structural and phase behavior of PE-stars and ionic microgels have been established, demonstrating the close relationship between the two systems [56, 57].

By and large, the theoretical investigations involving PE-stars have been limited to the study of either single PE-stars or bulk solutions of the same. However, a new field of promising applications and intriguing physics is arising when PE-stars or spherical PE-brushes are mixed with hard colloids or brought in contact with planar walls. Although the effects of confinement on linear PE-chains have been intensely studied theoretically [1, 58–68], experimentally [69–77], and by computer simulations [78–90], to our best knowledge only little work probing the same for PE-stars was done up to now. Thus, the goal of the thesis at hand is to fill this gap.

The rest of this work is organized as follows. In chapter 2, we bring a PE-star in close vicinity to a neutral, planar, and purely repulsive wall and analyze the physical mechanisms giving rise to effective wall–PE-star interactions. In chapter 3, we focus on the influence of wall curvature and derive effective potentials between PE-stars and hard, spherical colloids of larger size. Based on these interaction potentials, we proceed to the full many-body problem of colloid–PE-star mixtures and investigate the fluid structure. In chapter 4, we take the consequential next step and allow for the planar or curved walls to carry charges. Subsequently, we examine the induced adsorption of the PE-stars to the substrate, the complexation characteristics, and the resulting complex morphologies. In chapter 5, we summarize, conclude, and give an outlook to possible future work. Finally, in the Appendix we present some calculations omitted in the main text for sake of clarity and brevity.

Chapter 2

Polyelectrolyte stars in planar confinement

In this chapter, we employ monomer-resolved molecular dynamics (MD) simulations and theoretical considerations to analyze the conformations of multi-arm polyelectrolyte (PE) stars close to planar, uncharged walls. We identify three mechanisms that contribute to the emergence of a repulsive star–wall force, namely: the confinement of the counterions that are trapped in the star interior, the increase in electrostatic energy due to confinement as well as a novel mechanism arising from the compression of the stiff PE-chains approaching the wall. The latter is not present in the case of interactions between two PE-stars and is a direct consequence of the impenetrable character of the planar wall.

2.1 Introduction

As already stated in the introductory chapter 1, to our knowledge almost all theoretical investigations involving PE-stars have been restricted to the study of either isolated PE-stars or bulk solutions of the same, while the influence of confinement was not looked at. However, for PE-stars or spherical PE-brushes (SPEB's) which are in contact to planar walls or mixed with hard, spherical colloids, a vast range of fascinating new phenomena and promising novel applications is arising. Indeed, PE-stars can be used to model cell adhesion and are also efficient drug delivery and protein encapsulation and immobilization agents [6–9]. On the other hand, hydrogels, which are physically similar to PE-stars, adsorbed on planar walls, form arrays of dynamically tunable, photo-switchable or bioresponsive microlenses [91–94]. The encapsulation properties as well as the characteristics of the microlenses depend sensitively on the interactions between the PE-stars and the colloidal particles or the wall, respectively. Therefore, there exists a need to undertake a systematic

effort in trying to understand these interactions physically and make quantitative predictions about the ways to influence them externally. In this chapter, we take a first step in this direction by considering a PE-star in the neighborhood of a planar, uncharged, and purely repulsive wall. We analyze the mechanisms that give rise to an effective star–wall repulsion and identify the counterion entropy and the chain compression against the planar wall as the major factors contributing to this force. Our findings are corroborated by comparisons with MD simulation results for a wide range of parameters that structurally characterize the stars. These results provide the foundation for examining effects of wall curvature and charge.

This chapter is organized as follows: Sec. 2.2 is devoted to the description of the system we are investigating, the simulation model, and the simulation techniques used. Moreover, we specify the physical quantities of interest. Our theoretical approach is addressed in detail in Sec. 2.3. In Sec. 2.4, we quantitatively compare and discuss the respective results. Finally, we summarize and conclude in Sec. 2.5.

2.2 Simulation model

We start with a definition of the system under consideration including its relevant parameters and a description of the simulation model used. We study a dilute, salt-free solution of PE-stars confined between two hard walls parallel to the (x, y)-plane at positions $z = \pm\tau/2$, resulting in an overall wall-to-wall separation τ. We assume a good solvent that is only implicitly taken into account via its relative dielectric permittivity $\epsilon \approx 80$, i.e., we are dealing with an aqueous solution. Fig. 2.1 illustrates the situation. To avoid the appearance of image charges [90, 95], we assume the dielectric constants to be the same on both sides of the respective confining walls. It turns out, however, that this is not a severe assumption, because the effective charge of a PE-star is drastically reduced compared to its bare value, due to the strong absorption of neutralizing counterions [28, 32, 33, 96]. Hence, the influence of image charges can be expected to be of minor importance.

Clearly, the PE-stars themselves consist of f PE-chains, all attached to a common colloidal core of radius R_d, whose size is comparable to the monomer size and is therefore much smaller than the typical center-to-end length of the chains for all parameter combinations. The introduction of such a core particle is necessary to place the arms in the vicinity of the center, where the monomer density can take very high values. The theoretical approach pertains to the limit of vanishingly small core size. In order to remove effects arising from the small (but finite) value of the core in the simulation model and to provide a comparison with theory, we will henceforth employ a consistent small shift of the simulation data by R_d. This standard approach has been applied already, e.g., to the measurement of the interactions between neutral [22] and charged stars [32, 33], in order to isolate the direct core–core

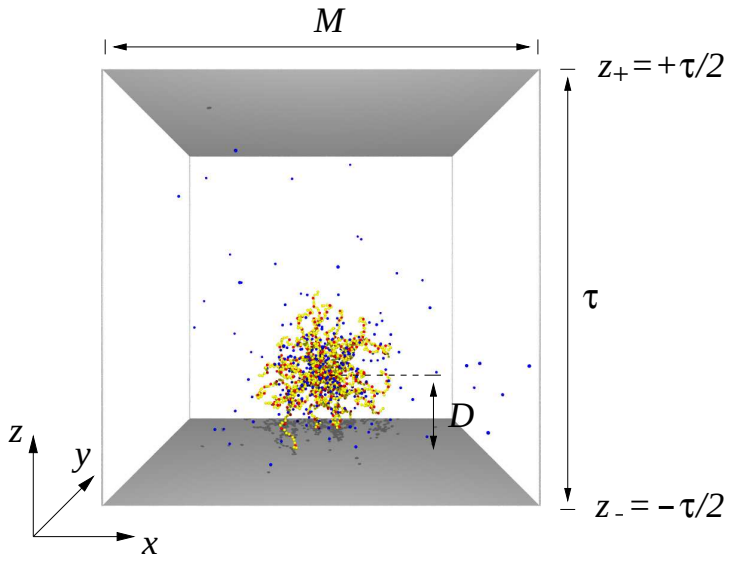

Figure 2.1: Sketch illustrating the geometry of the system: single PE-star (here with $f = 18$ arms) in planar confinement. Yellow balls symbolize neutral monomers, whereas the red spheres along the chain backbones denote monomer ions carrying a positive charge $+e$. The dark blue spheres are freely moving counterions, charge $-e$, neutralizing the total bare charge of the star.

interaction effects from the scaling laws valid at small inter-star separations.

The PE-chains are modeled as bead-spring chains of N Lennard-Jones (LJ) particles. This approach was first used in investigations of neutral polymer chains and stars [97–99] and turned out to be reasonable. The method was also already successfully applied in the case of polymer–colloid mixtures [100] or polyelectrolyte systems [32, 33, 96]. To mimic the above-mentioned good solvent conditions, a shifted and truncated LJ potential is introduced to depict the purely repulsive excluded volume interaction between the monomers,

$$V_{\mathrm{LJ}}(r) = \begin{cases} 4\varepsilon_{\mathrm{LJ}} \left[\left(\frac{d}{r}\right)^{12} - \left(\frac{d}{r}\right)^{6} + \frac{1}{4} \right] & r \leq 2^{1/6} d \\ 0 & r > 2^{1/6} d. \end{cases} \tag{2.1}$$

Here, r is the spatial distance of two interacting particles, d denotes the typical monomer diameter, and $\varepsilon_{\mathrm{LJ}}$ sets the basic energy scale for the system. In what follows, we fix the temperature of the system to the value $T = 1.2\varepsilon_{\mathrm{LJ}}/k_{\mathrm{B}}$, where k_{B} denotes Boltzmann's constant. The PE-chain connectivity is modeled by employing

a standard finite extension nonlinear elastic (FENE) potential [98, 99]:

$$V_{\mathrm{FENE}}(r) = \begin{cases} -\frac{k_{\mathrm{FENE}}}{2}\left(\frac{R_0}{d}\right)^2 \ln\left[1-\left(\frac{r}{R_0}\right)^2\right] & r \leq R_0 \\ \infty & r > R_0, \end{cases} \tag{2.2}$$

with a spring constant $k_{\mathrm{FENE}} = 7.0\varepsilon_{\mathrm{LJ}}$. The divergence length R_0 limits the maximum relative displacement of two neighboring monomers and is set to $R_0 = 2.0d$ in the scope of this work. The described set of parameters determines the equilibrium bond length, in our case resulting in a value $l_0 = 0.97d$.

When modeling the interactions between the monomers and a star's colloidal core, the finite radius R_{d} of the latter has to be taken into account. All monomers experience a repulsive interaction with the central particle, in analogy to Eq. (2.1) reading as

$$V_{\mathrm{LJ}}^{\mathrm{c}}(r) = \begin{cases} \infty & r \leq R_{\mathrm{d}} \\ V_{\mathrm{LJ}}(r - R_{\mathrm{d}}) & r > R_{\mathrm{d}}. \end{cases} \tag{2.3}$$

In addition, there is an attraction between the innermost monomers in the chain sequence of the arms and the core which is of FENE-type and can be written as follows [cf. Eq. (2.2)]:

$$V_{\mathrm{FENE}}^{\mathrm{c}}(r) = \begin{cases} \infty & r \leq R_{\mathrm{d}} \\ V_{\mathrm{FENE}}(r - R_{\mathrm{d}}) & r > R_{\mathrm{d}}. \end{cases} \tag{2.4}$$

The chains are charged in a periodic fashion by a fraction α in such a way that every $(1/\alpha)$-th monomer carries a monovalent charge $+e$, with $e > 0$ denoting the absolute value of the unit charge. Consequently, there is a total number of $N_- = \alpha f N$ monomer ions per PE-star. To ensure electroneutrality of the system as a whole, we include the same amount of oppositely charged, monovalent counterions in our considerations. Since the latter are able to freely move, they have to be simulated explicitly. Furthermore, they are of particular importance because they are expected to crucially affect the physics of the system. One example is the aforementioned fact that they induce a reduction of the stars' bare total charges.

Two charged beads with spatial distance r_{ij} interact by a full Coulomb potential, i.e., the electrostatic interaction energy is

$$\beta V_{\mathrm{Coul}}(r_{ij}) = \beta \frac{Z_i Z_j e^2}{\epsilon r_{ij}} \equiv \lambda_{\mathrm{B}} \frac{Z_i Z_j}{r_{ij}}. \tag{2.5}$$

Thereby, $Z_i, Z_j = \pm 1$ are the valencies of monomer ions and counterions, respectively, and $\beta = 1/k_{\mathrm{B}}T$ is the inverse temperature. In the above equation, the so-called Bjerrum length

$$\lambda_{\mathrm{B}} = \frac{\beta e^2}{\epsilon} \tag{2.6}$$

was introduced. It is defined as the distance at which the electrostatic energy equals the thermal energy. Thus, it characterizes the interaction strength of the Coulomb coupling. In the case of water at room temperature, one obtains $\lambda_\mathrm{B} = 7.1\,\text{Å}$. In our simulations, we fix the Bjerrum length to $\lambda_\mathrm{B} = 3.0d$, thus corresponding to an experimental particle diameter $d = 2.4\,\text{Å}$. This is a realistic value for typical polyelectrolytes [101].

For the purpose of completing the set of interaction potentials needed to describe the system at hand, we have to define particle–wall interactions. For technical reasons (see below), we do not regard the walls as true hard walls, as common in Monte-Carlo (MC) simulation studies [88, 102]. Following the course of our above modeling and based on Eq. (2.1), we assume them to be of truncated-and-shifted LJ-type instead, leading to the following monomer–wall interaction:

$$V_\mathrm{LJ}^\mathrm{w}(z) = V_\mathrm{LJ}\left(\frac{\tau}{2} - z\right) + V_\mathrm{LJ}\left(\frac{\tau}{2} + z\right), \tag{2.7}$$

whereas z refers to the z-component of the position vector of the particular bead. Likewise, the potential function for a star's core interacting with the confining walls is yielded by combining Eqs. (2.3) and (2.7):

$$V_\mathrm{LJ}^\mathrm{wc}(z) = V_\mathrm{LJ}\left(\frac{\tau}{2} - R_\mathrm{d} - z\right) + V_\mathrm{LJ}\left(\frac{\tau}{2} - R_\mathrm{d} + z\right). \tag{2.8}$$

To finalize this section, we present a short summary of the simulation techniques used. We perform monomer-resolved molecular dynamics (MD) simulations in the canonical ensemble, employing a rectangular simulation box of total volume $\Omega = M^2\tau$ that contains a single PE-star. We apply periodic boundary conditions in the x- and y-directions, while the box is confined with respect to the z-direction. Here, we always fix $M = \tau = 120d$. This provides a sufficiently large simulation box to suppress any undesirable side-effects *a priori* and emulates a dilute solution of PE-stars (cf. above description of the physical problem under investigation). For the numerical integration of the equations of motion, we adopt a so-called Verlet algorithm in its velocity form [12–14]. In order to stabilize the system's temperature, we make use of a Langevin thermostat [12–14] that introduces additional friction and random forces with appropriately balanced, temperature-dependent amplitudes. Due to the periodic boundary conditions and the long-range character of the Coulombic forces, a straight-forward calculation of the latter pursuant to Eq. (2.5) is not feasible. Therefore, we have to evaluate the forces using Lekner's well-established summation method [103] in its version for quasi two-dimensional geometries. Thereby, the convergence properties of the sums occurring during the computation are enhanced by a mathematically accurate rewriting, allowing a proper cut-off. For performance reasons, the forces have to be tabulated.

The typical time step is $\Delta t = 0.002 t_0$, with $t_0 = \sqrt{md^2/\varepsilon_{\rm LJ}}$ being the associated time unit and m the monomer mass. In our case, the counterions are taken to have the same mass and size as the (charged) monomers.

In our simulations, we measure the effective core–wall forces as a function of the center-to-wall distance D. Furthermore, we examine various other static quantities and their D-dependence, namely the center-to-end distance $R_{\rm s}$, the number of condensed counterions, and the density profiles of all particle species involved. For this purpose, for every particular value of D the system is equilibrated for about 5×10^5 time steps. After this equilibration period, we perform production runs lasting between 1×10^6 and 2×10^6 time steps. We carry out the above described measurements for a variety of arm numbers f (f =10, 18, 30) and charging fractions α (α =1/5, 1/4, 1/3) in order to make systematic predictions for the f- and α-dependencies of all theoretical parameters. In all cases, we fix the degree of polymerization, i.e., the number N of monomers per arm, to a value $N = 50$.

2.3 Theory of the effective PE-star–wall interaction

A PE-star in the neighborhood of a planar, impenetrable wall, undergoes conformational changes that modify its (free) energy in comparison to the value it has when the wall is absent or far away from the star. This separation-dependent difference between the free energies is precisely the effective interaction between the PE-star and the wall. There are three distinct mechanisms that give rise to an effective interaction in our case: the change in the electrostatic energy of the star, the change in the counterion entropy arising from the presence of the geometric confinement as well as contributions from a compression of the stiff PE-chains against the flat wall. The former two are intricately related to each other, as the counterion distribution is dictated by the strong Coulomb interactions, hence they will be examined jointly, the latter is a distinct phenomenon arising in the presence of impenetrable walls.

2.3.1 The electrostatic and entropic contributions

To obtain theoretical predictions for the electrostatic-entropic contribution to the free energy for a PE-star close to a flat, hard wall, we employ a mean-field approach, inspired by and akin to that developed in Refs. [28, 32, 33, 96]. Let $\rho_{\rm s} = N_{\rm s}/\Omega$ be the density of the solution of PE-stars, where $N_{\rm s}$ denotes the total number of PE-stars in the macroscopic volume Ω. In general, a single PE-star of total charge $Q_{\rm s}$ is envisioned as a spherical object of radius $R_{\rm s}$, embedded in an also spherical Wigner-Seitz cell of radius $R_{\rm W}$. Additionally, the latter contains N_- counterions, restricted to move in the Wigner-Seitz cell only and forming an oppositely charged

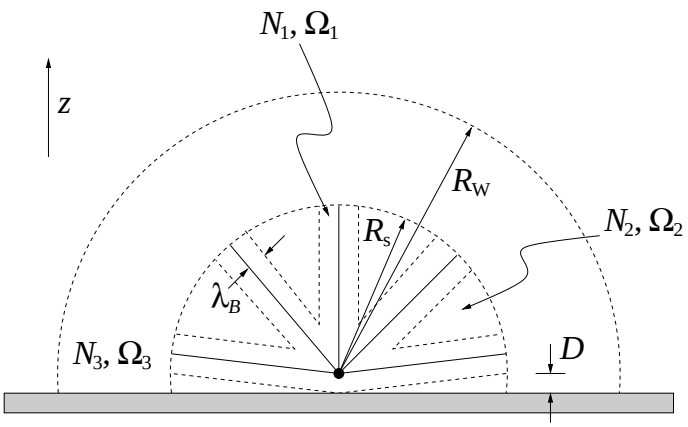

Figure 2.2: Sketch visualizing the physical situation at hand, namely showing a PE-star of typical spatial extent R_s, and its counterion background of radius R_W. The three possible counterion states are illustrated: Condensed, trapped, and free.

background of total charge $-Q_\mathrm{s}$. The cell's radius is connected to the star density via $R_\mathrm{W} = (4\pi\rho_\mathrm{s}/3)^{1/3}$. In the case of center-to-wall separations smaller than R_W and/or R_s, we simply cut the counterion cloud and/or the star itself at the confining wall and treat them as chopped spheres instead of full spheres. Obviously, the compound system composed of a PE-star and its counterions is electroneutral as a whole. Since we are interested in the case of dilute PE-solutions only, we can limit ourselves to the consideration of a single PE-star. Clearly, for center-to-wall distances $D > R_\mathrm{W}$ there is no interaction between a PE-star and the wall within the framework of our theory. Accordingly, we will deal with the case $D \leq R_\mathrm{W}$ only. Fig. 2.2 sketches the physical situation and visualizes the decisive length scales of the problem.

A mechanism crucially influencing the physics of PE-systems is the so-called Manning condensation of counterions [104–111]. The dimensionless fraction $\xi = \lambda_\mathrm{B} N\alpha/R_\mathrm{s}$ indicates whether or not such a condensation effect will occur. If it exceeds unity, counterions will condense on the arms of the stars [104–106]. In our case, this condition is true for all parameter combinations examined (see below). Hence, the condensation effect has to be taken into account in our theoretical modeling. For that reason, we partition the counterions in three different states, an ansatz already put forward in Refs. [32, 33, 112]: N_1 of the N_- counterions are in the condensed state, i.e., they are confined in imaginary hollow tubes of outer radius λ_B and inner radius d around the arms of the star. The total volume[1] accessible for the counterions in this state is $\Omega_1 = \pi(\lambda_\mathrm{B}^2 - d^2)R_\mathrm{s} f$. A number of N_2 counterions is considered to

[1]Here, the tube overlap in the vicinity of the colloidal core is not taken into account. Accordingly, the resulting reduction of the volume Ω_1 with respect to the value given in the main text is neglected. Anyway, this simplification does not considerably affect the theoretical results.

be trapped in the interior of the star. These ions are allowed to explore the overall volume $\Omega_{\rm in} = \Omega_{\rm cs}(D, R_{\rm s})$ of the (possibly chopped) star except the tubes introduced above, i.e., $\Omega_2 = \Omega_{\rm in} - \Omega_1$. Thereby, the volume $\Omega_{\rm cs}$ of a chopped sphere can be derived by straight-forward calculations. With $\Omega_{\rm s}(R_{\rm s}) = 4\pi R_{\rm s}^3/3$, one obtains:

$$\frac{\Omega_{\rm cs}(D, R_{\rm s})}{\Omega_{\rm s}(R_{\rm s})} = \begin{cases} \frac{1}{2} + \frac{3}{4}\left(\frac{D}{R_{\rm s}}\right) - \frac{1}{4}\left(\frac{D}{R_{\rm s}}\right)^3 & D \le R_{\rm s} \\ 1 & D > R_{\rm s}. \end{cases} \tag{2.9}$$

Note that the total volume of the star is big compared to the volume of the tubes surrounding the arms, $\Omega_{\rm in} \gg \Omega_1$. Thus, we will make use of the approximation $\Omega_2 \approx \Omega_{\rm in}$ in all steps to come. The remaining $N_3 = N_- - N_1 - N_2$ counterions are able to move freely within the outer shell of volume $\Omega_{\rm out} = \Omega_3 = \Omega_{\rm cs}(D, R_{\rm W}) - \Omega_{\rm in}$ surrounding the star, where $\Omega_{\rm cs}(D, R_{\rm W})$ is the total volume of the Wigner-Seitz cell. The subdivision of counterions in the three different states is also depicted in Fig. 2.2, showing a star with five arms that are assumed to be fully stretched for demonstration.

The electrostatic and entropic part $V_{\rm ee}(D)$ of the effective interaction $V_{\rm eff}(D)$ between the PE-star and the wall, kept at center-to-wall distance D, results after taking a canonical trace over all but the star center degree of freedom. With $\mathcal{F}_{\rm ee}(D; R_{\rm s}, \{N_i\})$ being the variational Helmholtz free energy for a system where a single star faces the confining wall, and which contains just the electrostatic and entropic parts, it is defined as [4]:

$$V_{\rm ee}(D) = \min_{R_{\rm s}, \{N_i\}} \mathcal{F}_{\rm ee}(D; R_{\rm s}, \{N_i\}). \tag{2.10}$$

Basically, the equilibrium values of $R_{\rm s}$ and $\{N_i\}$ are determined by the above minimization. We will discuss this point in more detail shortly. Note that we neglected a second, D-independent term on the right-hand side of Eq. (2.10) representing the contribution to the free energy for an infinitely large center-to-wall separation. Since it makes up a constant energy shift only, it does not influence the effective forces between the star and the wall we are mainly interested in. The electrostatic-entropic force contributions are obtained by differentiating with respect to D:

$$F_{\rm ee}(D) = -\frac{\partial V_{\rm ee}(D)}{\partial D} \tag{2.11}$$

Now, we derive expressions for the terms of which $\mathcal{F}_{\rm ee}(D; R_{\rm s}, \{N_i\})$ is built-up, whereby we want to include both the counterions' entropic contributions and the electrostatic energy. To keep our theory as simple as possible, we will omit other thinkable contributions, like elastic energies of the chains [113] or Flory-type terms arising through self-avoidance [113, 114]. As we will see in Sec. 2.4, our theoretical

results in combination with chain compression terms to be deduced in what follows, are capable of producing very good agreement between the theory and the corresponding simulational data; these simplifications are therefore *a posteriori* justified. Consequently, the free energy $\mathcal{F}_{\mathrm{ee}}(D; R_{\mathrm{s}}, \{N_i\})$ reads as:

$$\mathcal{F}_{\mathrm{ee}}(D; R_{\mathrm{s}}, \{N_i\}) = U_{\mathrm{es}} + \sum_{i=1}^{3} S_i. \tag{2.12}$$

The electrostatic mean-field energy U_{es} is assumed to be given by a so-called Hartree-type expression. Let $\rho_{\mathrm{m}}(\mathbf{r})$ and $\rho_i(\mathbf{r})$ denote the number densities of the monomers and the three different counterion species, respectively, measured with respect to the star's geometrical center. These density profiles then determine the overall local charge density $\varrho(\mathbf{r})$ of our model system. Therewith, we have:

$$U_{\mathrm{es}} = \frac{1}{2\epsilon} \iint \mathrm{d}^3 r \; \mathrm{d}^3 r' \; \frac{\varrho(\mathbf{r})\varrho(\mathbf{r}')}{|\mathbf{r} - \mathbf{r}'|}. \tag{2.13}$$

It is convenient to separate the total charge density $\varrho(\mathbf{r})$ into two contributions: $\varrho_{\mathrm{in}}(\mathbf{r})$ in the interior of the star, i.e., the volume Ω_{in}, and $\varrho_{\mathrm{out}}(\mathbf{r})$ in the outer region, i.e., the volume Ω_{out}. Let $\Phi_{\mathrm{in}}(\mathbf{r})$ and $\Phi_{\mathrm{out}}(\mathbf{r})$ be the contributions to the electrostatic potential at an arbitrary point $\mathbf{r}$ in space caused by the respective charge densities. Using this definitions, we can rewrite Eq. (2.13) and get

$$\begin{aligned} U_{\mathrm{es}} =& \frac{1}{2} \left\{ \int_{\Omega_{\mathrm{in}}} \mathrm{d}^3 r \; \left[\Phi_{\mathrm{in}}(\mathbf{r}) + \Phi_{\mathrm{out}}(\mathbf{r})\right] \varrho_{\mathrm{in}}(\mathbf{r}) \right. \\ & \left. + \int_{\Omega_{\mathrm{out}}} \mathrm{d}^3 r \; \left[\Phi_{\mathrm{in}}(\mathbf{r}) + \Phi_{\mathrm{out}}(\mathbf{r})\right] \varrho_{\mathrm{out}}(\mathbf{r}) \right\}. \end{aligned} \tag{2.14}$$

On purely dimensional grounds, we expect a result having the general form

$$\begin{aligned} \beta U_{\mathrm{es}} =& \frac{N_3 \lambda_{\mathrm{B}}}{R_{\mathrm{s}}} \cdot h\left(\frac{R_{\mathrm{W}}}{R_{\mathrm{s}}}, \frac{D}{R_{\mathrm{s}}}\right) \\ =& \frac{N_3 \lambda_{\mathrm{B}}}{R_{\mathrm{s}}} \left[h_{\mathrm{in-in}}\left(\frac{D}{R_{\mathrm{s}}}\right) + 2h_{\mathrm{in-out}}\left(\frac{R_{\mathrm{W}}}{R_{\mathrm{s}}}, \frac{D}{R_{\mathrm{s}}}\right) \right. \\ & \left. + h_{\mathrm{out-out}}\left(\frac{R_{\mathrm{W}}}{R_{\mathrm{s}}}, \frac{D}{R_{\mathrm{s}}}\right) \right], \end{aligned} \tag{2.15}$$

where we introduced dimensionless functions h and $h_{\alpha-\beta}$ arising from the integrations of the products $\Phi_\alpha(\mathbf{r})\varrho_\beta(\mathbf{r})$ in Eq. (2.14) [with $\alpha, \beta = \mathrm{in}, \mathrm{out}$]. Here, one should remember that N_3 is the number of uncompensated charges of the star and characterizes its effective valency. The specific shape of the h-functions depends on the underlying charge distributions $\varrho_{\mathrm{in}}(\mathbf{r})$ and $\varrho_{\mathrm{out}}(\mathbf{r})$ alone.

In Eq. (2.12), the terms S_i represent the ideal entropic free energy contributions of the different counterion species. They take the form

$$\beta S_i = \int_{\Omega_i} \mathrm{d}^3 r \; \rho_i(\mathbf{r}) \left[\ln\left(\rho_i(\mathbf{r}) d^3\right) - 1 \right] + 3N_i \ln\left(\frac{\Lambda}{d}\right), \tag{2.16}$$

where Λ is the thermal de-Broglie wavelength. In writing the sum in Eq. (2.12), the respective last terms in Eq. (2.16) yield an trivial additive constant only, namely $3N_- \ln(\Lambda/d)$, which will be left out in what follows.

Now, we have to quantitatively address the electrostatic and entropic terms pursuant to Eqs. (2.13) to (2.16). For that purpose, we first of all need to specify the above introduced number densities[2], $\rho_\mathrm{m}(\mathbf{r})$ and $\rho_i(\mathbf{r})$. Here, we model the arms of the PE-star to be fully stretched, or to put it in other words, the monomer density profile inside the star to fall of as $\rho_\mathrm{m}(\mathbf{r}) = \rho_\mathrm{m}(r) \sim r^{-2}$ [28–30, 32]. This is a good approximation, as measurements yield a scaling behavior with an only somewhat smaller exponent $\cong -1.8$, indicating an almost complete stretching of the chains [32, 33, 109, 115–117]. Since the monomer ions are placed on the backbone of the chains in a periodical manner (cf. Sec. 2.2), their density within the interior of the star must obviously show an identical r-dependence. Moreover, the profile for the trapped counterions exhibits the same scaling, due to the system's tendency to achieve local electroneutrality [118]. Therefore, it seems to be a good choice to use an ansatz $\rho_2(r) = A/r^2$ for the trapped counterions and $\varrho_\mathrm{in}(r) = B/r^2$ for the overall charge density in the inner region. Clearly, these distributions have to be normalized with respect to the total number of trapped counterions N_2 and the effective charge of the star $Q_\mathrm{s}^*/e = (N_- - N_1 - N_2) = N_3$ by integrating over the related volumes, Ω_2 and Ω_in. In doing so, we obtain $A = N_2/(2\pi R_\mathrm{s} C)$ and $B = Q_\mathrm{s}^*/(2\pi R_\mathrm{s} C)$, with

$$C = 1 + \frac{D}{R_\mathrm{s}} \left[1 - \ln\left(\frac{D}{R_\mathrm{s}}\right) \right]. \tag{2.17}$$

We presume the condensed counterions to be uniformly distributed within the tubes surrounding the PE-chains, i.e., we use $\rho_1 = N_1/\Omega_1$. This approach is supported by simulation results on single PE-chains [108] and was successfully put forward in previous studies of PE-star systems [32, 33]. In a similar fashion, we assume an also uniform distribution of the free counterions within the outer shell $R_\mathrm{s} < r < R_\mathrm{W}$, i.e., $\rho_3 = N_3/\Omega_3$, implying an associated charge density $\varrho_\mathrm{out} = -Q_\mathrm{s}^*/\Omega_3$.

On this basis, we are able to explicitly calculate the variational free energy in virtue of Eqs. (2.12) to (2.16). As far as the entropic contributions are concerned,

[2]Note that, compared to the isolated star case, any influence of the wall to the density profiles besides a chopping of the volumes available for monomers, monomer ions, and counterions will be omitted. We will model all densities similar to the approach used in Refs. [32, 33].

an analytical computation is feasible in a straight-forward manner. For reasons of clarity, we leave out any intermediate steps and present our final results only:

$$\frac{\beta S_1}{N_1} = \ln\left[\frac{N_1 d^3}{\pi(\lambda_\mathrm{B}^2 - d^2) R_\mathrm{s} f}\right] - 1, \tag{2.18}$$

$$\frac{\beta S_2}{N_2} = \ln\left(\frac{N_2}{2\pi C}\right) + \frac{D}{R_\mathrm{s} C}\ln^2\left(\frac{D}{R_\mathrm{s}}\right) - 3\ln\left(\frac{R_\mathrm{s}}{d}\right) + 1, \tag{2.19}$$

$$\frac{\beta S_3}{N_3} = \ln\left\{\frac{N_3}{\frac{2\pi}{3}\left[\left(\frac{R_\mathrm{W}}{R_\mathrm{s}}\right)^3 - 1\right] + \frac{\pi D}{R_\mathrm{s}}\left[\left(\frac{R_\mathrm{W}}{R_\mathrm{s}}\right)^2 + 1\right]}\right\} - 3\ln\left(\frac{R_\mathrm{s}}{d}\right) - 1. \tag{2.20}$$

Now, we want to investigate the electrostatic term U_es in more detail. To begin with, we have to derive expressions for the potential functions $\Phi_\mathrm{in}(\mathbf{r})$ and $\Phi_\mathrm{out}(\mathbf{r})$. This computations are rather technical, and within the main text we will therefore outline the course of action only. For a detailed presentation and explicit description of the procedure, we refer the reader to Appendices A and B, respectively. In general, the electrostatic potential $\Phi(\mathbf{r})$ due to a charge density $\varrho(\mathbf{r})$ in a dielectric medium of permittivity ϵ is given by the expression

$$\Phi(\mathbf{r}) = \frac{1}{\epsilon}\int \mathrm{d}^3 r' \, \frac{\varrho(\mathbf{r}')}{|\mathbf{r}' - \mathbf{r}|}. \tag{2.21}$$

In order to calculate the integral above for a chopped sphere, yielding the function $\Phi_\mathrm{in}(\mathbf{r})$, we decompose it in infinitesimally thin disks which are oriented perpendicular to the z-axis and cover the whole sphere. The radii of these disks obviously depend on their position with respect to the center of the sphere. Afterwards, each disk is object to further decomposition into concentric rings. Provided that the charge density is spherical symmetric, as is in the case under consideration, the charge carried by each ring can be easily calculated. The electrostatic potential of a charged ring is known from literature [119,120], therefore the potential of a disk can be derived by integrating over all corresponding rings. An analytical determination of this integral is possible. The potential of the chopped sphere itself can then be obtained by another integration over all disks. The latter cannot be performed analytically, thus one has to resort to a simple, one-dimensional numerical integration. So far, the potential $\Phi_\mathrm{out}(\mathbf{r})$ caused by the hollow chopped sphere of volume Ω_out containing the free counterions remains to be acquired. Thereto, we employ the

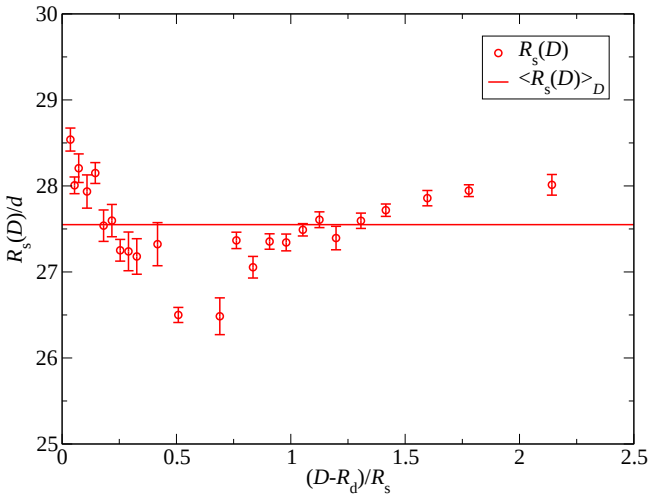

Figure 2.3: Star radii vs. the star–wall separation D as obtained by MD simulations, referring to parameters $f = 10$, $\alpha = 1/3$. The mean value, averaged with respect to D, is shown as a horizontal line for comparison.

superposition principle. The hollow region of uniform charge density ϱ_{out} can be apprehended as a superposition of two chopped spheres with radii R_{s} and R_{W}, and charge densities $-\varrho_{\text{out}}$ and ϱ_{out}, respectively. In doing so, the problem is reduced to the calculation of the electrostatic potential of a chopped sphere with uniform charge density, which can be computed following the method described above for the inner sphere of volume Ω_{in}. Clearly, with knowledge of both $\Phi_{\text{in}}(\mathbf{r})$ and $\Phi_{\text{out}}(\mathbf{r})$, the dimensionless functions $h_{\alpha-\beta}$ and thus the electrostatic energy U_{es} can be obtained according to Eqs. (2.14) and (2.15) using numerical techniques.

In principle, the electrostatic-entropic interaction potential $V_{\text{ee}}(D)$ is obtained by adding up the entropic and electrostatic contributions following Eq. (2.12) and minimizing the Helmholtz free energy $\mathcal{F}_{\text{ee}}(D; R_{\text{s}}, \{N_i\})$ with respect to R_{s} and $\{N_i\}$ [cf. Eq. (2.10)]. However, the star radii are in good approximation unaffected by the center-to-wall separation D, as confirmed by our simulations. The physical reason lies in the already almost complete stretching of the chains due to their charging. In the simulations, the arm-averaged center-to-end radius R_{s} of a star was measured according to

$$R_{\text{s}}^2 = \frac{1}{f}\left\langle \sum_{i=0}^{f-1} (\mathbf{r}_{i,N} - \mathbf{r}_{\text{core}})^2 \right\rangle , \tag{2.22}$$

where $\mathbf{r}_{i,N}$ stands for the position vector of the N-th (last) monomer of the i-th arm ($0 \leq i < f$) of the star and $\mathbf{r}_{\text{core}}$ the core position. Fig. 2.3 illustrates the weak D-dependence of R_{s} for an exemplarily chosen parameter combination. Therefore,

f	α	N_-	$(R_s/d)^a$	$(N_1)^a$	$(N_1)^b$	$(R_s/d)^c$	$(N_1)^c$
10	1/5	100	24.0	32	53	–	–
10	1/4	120	24.8	44	68	25.3	46
10	1/3	170	27.5	76	107	27.4	72
18	1/5	180	24.6	78	80	–	–
18	1/4	216	25.4	104	111	26.6	107
18	1/3	306	28.0	163	183	28.3	159
30	1/5	300	25.1	161	113	–	–
30	1/4	360	25.9	208	170	27.2	213
30	1/3	510	28.4	315	294	28.6	309

Table 2.1: Conformational properties as obtained from MD simulations and corresponding fit parameters used in our theoretical approach for different arm numbers and charging fractions. In addition, results from Ref. [33] are presented for comparison. The chain length is fixed to $N = 50$. For our data, the Wigner-Seitz radius is $R_W/d = 74.44$. Legend for the symbols: [a]Values as obtained from our MD simulations, averaged with respect to D (cf. Sec. 2.3); [b]Fit parameter used when calculating theoretical predictions for star–wall forces; [c]Simulation results for isolated PE-stars, taken from Ref. [33] and shown for comparison (note that there are in part insignificant discrepancies concerning the parameters).

it is convenient not to determine R_s through the variational calculation, but to use average values $\langle R_s \rangle_D$ as obtained from MD simulations instead. The latter are comparable to the corresponding radii for isolated PE-stars according to Ref. [33], see Table 2.1.

The amount of condensed counterions N_1 was measured by counting the number of such particles separated from the monomer ions by a distance smaller than λ_B and performing a statistical average. The total number of captured counterions, $N_{in} = N_1 + N_2$, was measured by counting all counterions within a sphere having the instantaneous, arm-averaged center-to-end distance as radius and again taking a time average. Since the $\{N_i\}$ are related through the equation $N_- = N_1 + N_2 + N_3$, only two independent variational parameters remain, say N_1 and N_2. In our simulations, we have found that the number of condensed counterions, N_1, is also approximately constant with respect to D (see Fig. 2.4). Hence, we will treat N_1 as a fit parameter, held constant for all D and chosen in such a way to achieve optimal agreement with simulation results. Therefore, $\mathcal{F}_{ee}(D; R_s, \{N_i\})$ is minimized with respect to the number of trapped counterions, N_2, only, reflecting the possibility of redistribution of counterions between inside/outside the stars as the distance to the wall is varied.

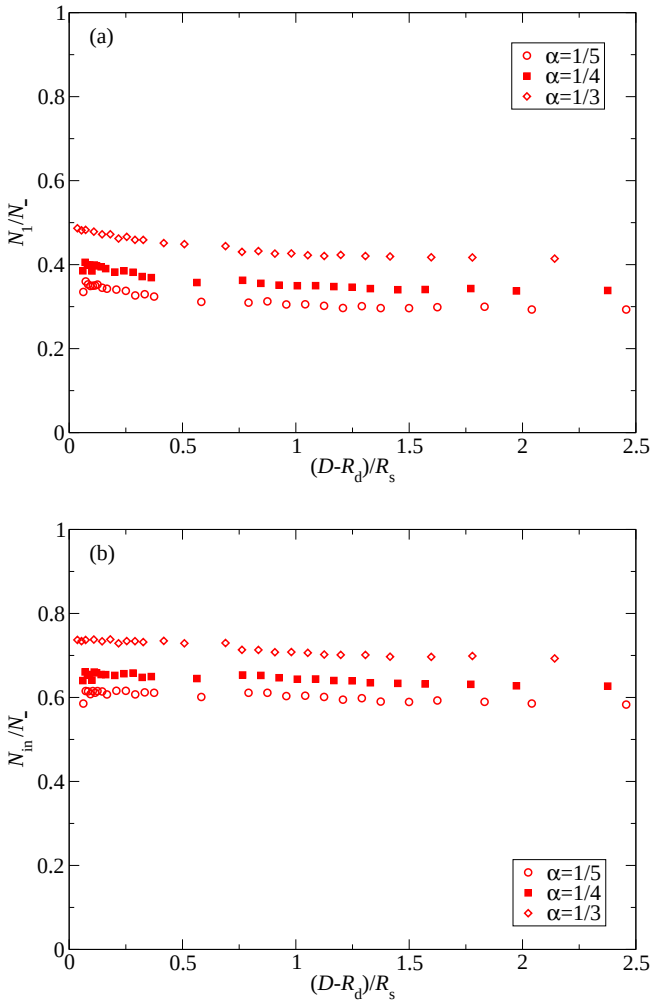

Figure 2.4: Fractions of (a) condensed counterions N_1/N_- and (b) captured counterions $N_{\rm in}/N_- = (N_1 + N_2)/N_-$ for PE-stars with $f = 10$ arms and various values of α. As one can see from the plots, both quantities are in very good approximation independent on D and the majority of counterions is captured within the interior of the star.

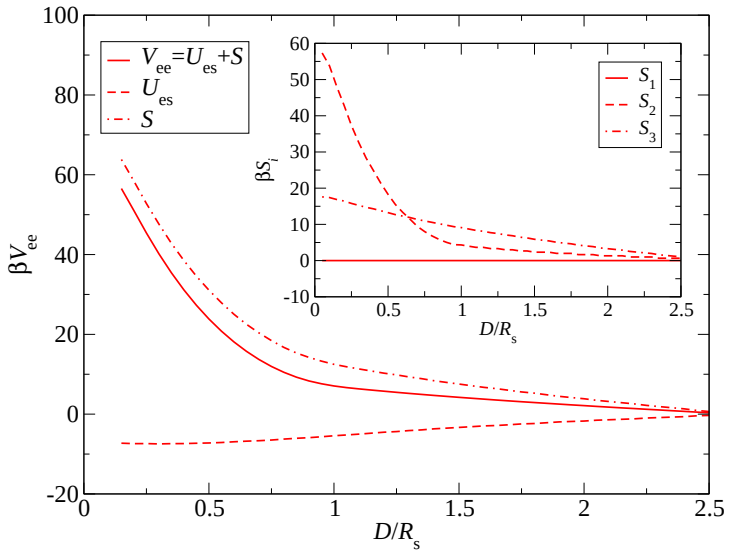

Figure 2.5: Comparison of the entropic and the electrostatic contributions S and $U_{\rm es}$ to the electrostatic-entropic part of the effective potential, $V_{\rm ee}$, exemplarily shown for $f = 10$, $\alpha = 1/3$, and $N_1 = 107$. Obviously, the entropic contribution dominantly determines the D-dependence of $V_{\rm ee}$. In the inset, S is decomposed into the different counterion species' contributions S_i, illustrating that the term S_2 governs the functional form of the total entropy. Note that the different contributions in both main plot and inset were shifted by constants to enhance the readability.

Fig. 2.5 shows a comparison of the entropic and the electrostatic contributions S and $U_{\rm es}$ to the electrostatic-entropic effective potential, $V_{\rm ee}$. As one can see from the exemplary plot, the total entropic term S is the major contribution to $V_{\rm ee}$ and therefore determines the functional form of the latter, while the electrostatic term is of minor importance. At first glance, this may seem to be counterintuitive in a PE-system, but electrostatics do, in fact, indirectly affect the interaction potential. Due to the presence of charges, the conformations and thus the radii of PE-stars are strongly changed compared to the neutral star case, leading to an increased range of the interaction. In the inset of Fig. 2.5 it can be seen that total entropy of the system at hand is mainly determined by the contribution S_2 of the trapped counterions. As one can recognize, S_3 is only weakly influenced by the star-to-wall separation D, and S_1 is even completely independent of D, as was evident already from Eq. (2.18). We have to emphasize, however, that even though S_1 contributes a constant value only and therefore does not influence the effective force $F_{\rm ee}(D)$ at all, the number of condensed counterions N_1 nevertheless plays a fundamental role in our problem. Since $N_2 = N_{\rm in} - N_1$ set the overall scale for of the term S_2, N_1 becomes relevant

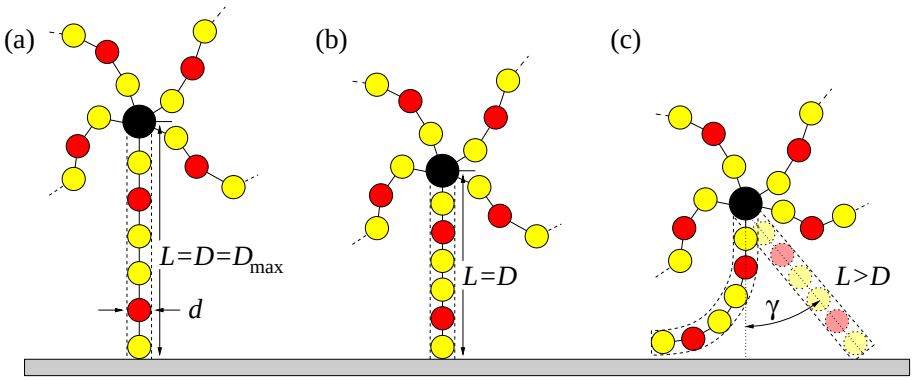

Figure 2.6: Schematic illustrating the physical mechanism leading to the necessity to introduce the energy contribution V_c. In analogy to Fig. 2.1, yellow circles denote neutral monomers and red balls are monomer ions. The bigger black ball is the colloidal core of the star. Counterions are omitted in the depiction for reasons of clarity. In part (c) of the figure, the dashed rod replacing the chain bent to the left is shown mirror-reflected to the right to avoid crowding. For a more detailed discussion of the compression effect, see main text.

in renormalizing the effective interaction. The treatment of N_1 and the net charge, consequently, as a fit parameter is a common approach for charged systems, known as charge renormalization [121–123].

2.3.2 The chain compression contribution

In anticipation of Sec. 2.4, we want to point out that significant deviations arise between the effective star–wall forces as obtained by our computer simulations and their theoretical counterparts F_{ee} calculated using the formalism presented in Sec. 2.3.1 for intermediate center-to-surface distances $0.6 \lesssim D/R_s \lesssim 1.3$. Now, we want to elucidate the physical mechanism leading to these deviations and derive simple expressions for additional contributions to both the total effective forces and potentials, F_c and V_c. Therewith, we will complete the development of our theoretical approach.

The need to introduce these supplementary contributions is due to so far unconsidered conformational changes enforced by the presence of the confining wall. During the construction of the mean-field part of our theory, we neglected such changes by assuming density profiles of monomers and counterions which are undisturbed compared to the case of isolated stars in fully three-dimensional geometries. The influence of the wall became manifest in a truncation of the spheres representing star and associated counterion cloud, only. But in reality, for D in the order of the typical

length of an arm of the star, the star will undergo strong configurational variations to avoid the wall since the monomers are not able to interpenetrate it. Thereby, due to the presence of neighboring arms, it can be energetically favorable for chains directing towards the wall to compress instead of bending away from the surface, although this compression leads to an extra cost in electrostatic energy. The latter obviously originates from a decrease of the ion–ion distances along the backbones of the chains. Figs. 2.6(a) and 2.6(b) depict the situation. Once a critical value of the chain length is reached, a further shortening of the chains under consideration becomes disadvantageous. Electrostatic repulsions and excluded volume interaction increase more and more strongly, the chains will preferably curve and start to relax in length, see Fig. 2.6(c). The occurrence of such compression–decompression processes is proven by our simulation runs.

In what follows, we will use a simplified picture and model the affected arms as rigid, uniformly charged rods of common length L and diameter d for both the compressed and the bent regime. In the former case, we assume the rods to have orientations perpendicular to the wall surface. In the latter case, we will account for the bending only via the re-lengthening of the rods and their change in orientation with respect to the z-axis. Fig. 2.6(c) visualizes this approximation, whereby the shaded straight chain represents the imaginary rod that replaces the bent arm within the framework of our modeling. With $Z = +1$ being the valency of the monomer ions, the total charge of one such rod is just $Ze\alpha N$, leading to an L-dependent linear charge density, η, given by $\eta = Ze\alpha N/L$. We consider the self-energy of one rod, as a function of its respective length L, to be made up of a purely repulsive contribution which is electrostatic in nature and arises due to like-charge repulsions, and a second harmonic term with an effective spring constant k_{eff} describing the binding of the chain monomers in a coarse-grained fashion. Thus, we have [124]:

$$\begin{aligned}\beta U_{\text{rod}}(L) &= \beta U_{\text{rep}}(L) + \beta U_{\text{attr}}(L) \\ &= \beta\frac{\eta^2}{\epsilon} L \ln\left(\frac{L}{d}\right) - \beta\frac{k_{\text{eff}}}{2}L^2 \\ &= \frac{Z^2\alpha^2 N^2 \lambda_{\text{B}}}{L}\ln\left(\frac{L}{d}\right) - \beta\frac{k_{\text{eff}}}{2}L^2. \end{aligned} \tag{2.23}$$

From Eq. (2.23), we then obtain the corresponding force $F_{\text{rod}}(L) = -\partial U_{\text{rod}}/\partial L$ that acts on the ends of the rod parallel to its direction (a negative/positive sign of $F_{\text{rod}}(L)$ corresponds to a force that tends to compress/stretch the rod.) The competition of a repulsive and an attractive part results in a finite equilibrium length L_0 of the rod, i.e., F_{rod} vanishes for $L = L_0$. Clearly, L_0 is related to the above introduced spring constant k_{eff} by the following condition:

$$k_{\text{eff}} = \frac{1}{L_0}\left.\frac{\partial U_{\text{rep}}}{\partial L}\right|_{L_0}. \tag{2.24}$$

Now, let $D_{\min}$ and $D_{\max}$ determine the range of center-to-surface distances for which the above described processes take place. Moreover, D_0 denotes the critical length for which the transition from the compressing to the bending regime is observed. According to our MD results, we will fix $D_{\max}/R_{\mathrm{s}} = 1.3$, $D_0/R_{\mathrm{s}} = 0.9$, and $D_{\min}/R_{\mathrm{s}} = (2D_0 - D_{\max})/R_{\mathrm{s}} = 0.5$. In addition, we require $L_0 = D_{\max}$ in what follows. We know from our simulation runs that it is a reasonable first-order approximation to assume the length of the affected chains as a function of D to be:

$$L(D) = \begin{cases} D_{\max} & D \in [0, D_{\min}[\\ 2D_0 - D & D \in [D_{\min}, D_0[\\ D & D \in [D_0, D_{\max}[\\ D_{\max} & D \in [D_{\max}, \infty[. \end{cases} \tag{2.25}$$

By using this empirical fact, we implicitly include effects due to chain bending and entropic repulsions of neighboring chains, even if we did not consider corresponding energy contributions explicitly in Eq. (2.23). Therewith, a promising estimate for the chain compression contribution to the total effective force is:

$$F_{\mathrm{c}}(D) = \begin{cases} f_{\mathrm{eff}} \frac{D}{L(D)} F_{\mathrm{rod}}(L(D)) & D \in [D_{\min}, D_{\max}] \\ 0 & \text{else.} \end{cases} \tag{2.26}$$

Here, f_{eff} is the total number of affected chains. Assuming that the chains are regularly attached to the colloidal core, we expect a linear relation between f_{eff} and f, namely $f_{\mathrm{eff}} = f/f_0$. Simulation data indicate $f_0 = 4$ to be a good choice for all parameter combinations under investigation. Since F_{rod} is always directed parallel to the corresponding rod, the pre-factor $D/L(D) = \cos\gamma$ results from simple geometrical considerations [cf. Fig. 2.6(c)].

Based on Eq. (2.26), we obtain the corresponding energy term V_{c} by a simple integration:

$$V_{\mathrm{c}}(D) = \int_{\infty}^{D} F_{\mathrm{c}}(D')\, \mathrm{d}D'. \tag{2.27}$$

Finally, the total effective forces and interaction potentials are obtained as the sum of the electrostatic-entropic and compression terms: $F_{\mathrm{eff}} = F_{\mathrm{ee}} + F_{\mathrm{c}}$ and $V_{\mathrm{eff}} = V_{\mathrm{ee}} + V_{\mathrm{c}}$, respectively. Fig. 2.7 shows a concluding comparison of the full effective potential $V_{\mathrm{eff}}(D)$ and the same without the inclusion of the compression term $V_{\mathrm{c}}(D)$. According to the plot, the theoretically predicted total potential is purely repulsive and ultra-soft. As we will see in Sec. 2.4, the total effective forces show a striking step-like shape for intermediate distances. This is in contrast to the well-known case of star–star interactions [32, 33].

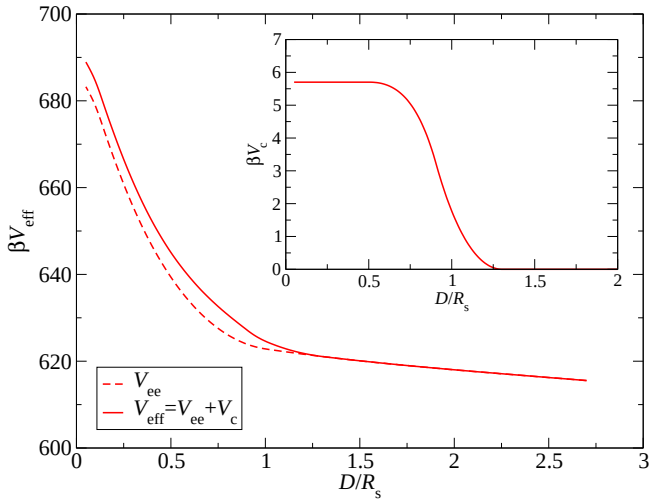

Figure 2.7: Comparison of the total and the electrostatic-entropic contributions to the effective potential, $V_{\rm eff}(D)$ and $V_{\rm ee}(D)$, for $f = 10$, $\alpha = 1/3$, and $N_1 = 107$. The inset shows the functional form of the compression term $V_{\rm c}(D)$. The main text provides an explanation for the need of the latter contribution and contains an explicit derivation.

2.4 Comparison and discussion

In this section, we test our theoretical model against corresponding simulation results to confirm its validity. Using standard MD techniques, a straight-forward measurement of (effective) interaction potentials is not possible. Thereto, one would have to apply more sophisticated methods [24]. But since the mean force acting on the center of a PE-star can be easily received from computer experiments [4,22], we will focus on a comparison of such effective forces and corresponding theoretical predictions. To be more precise, when choosing the colloidal center of a star at a fixed position $\mathbf{r}_{\rm core}$ as effective coordinate in our simulations, the effective force can be measured as the time average over all instantaneous forces $\mathbf{f}_{\rm core}$ acting on the core (cf. also the simulation model in Sec. 2.2) by means of the expression

$$\mathbf{F}(\mathbf{r}_{\rm core}) = -\nabla_{\mathbf{r}_{\rm core}} V_{\rm eff}(\mathbf{r}_{\rm core}) = \langle \mathbf{f}_{\rm core} \rangle \,. \tag{2.28}$$

In all considerations to come, we will deal with absolute values of the forces only. It is obvious from the chosen geometry that the effective forces are on average directed perpendicular to the confining wall, i.e., parallel to the z-axis. Thus, the mean values of the x- and y-components vanish, leading to the relation $F_{\rm eff} = |\mathbf{F}_{\rm eff}| = F_{{\rm eff},z}$. For symmetry reasons, the effective forces and potentials depend on the z-component of $\mathbf{r}_{\rm core}$ alone, whereas $r_{{\rm core},z} = D$. Consequently, the forces are

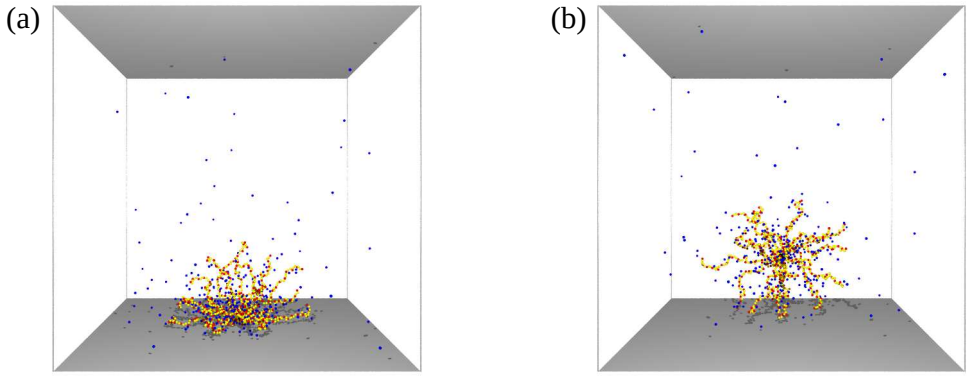

Figure 2.8: Simulation snapshots of a PE-star with functionality $f = 18$ and charging fraction $\alpha = 1/3$. The center-to-wall distances are (a) $D/R_\mathrm{s} = 0.107$ and (b) $D/R_\mathrm{s} = 1.07$. The color coding for the particles is the same as in Fig. 2.1.

connected to the potential by the following simple equation:

$$F_\mathrm{eff}(\mathbf{r}_\mathrm{core}) = F_\mathrm{eff}(D) = -\frac{\partial V_\mathrm{eff}}{\partial D}. \tag{2.29}$$

Therewith, predictions for the effective forces can be computed starting from theoretical results for the corresponding potential (see Sec. 2.3, Fig. 2.7). This allows for the desired comparison to MD data.

Fig. 2.8 shows typical simulation snapshots for two different values of the center-to-surface separation D, illustrating the conformational changes a star undergoes due to the presence of the confining wall. In part (b) of the figure, one may particularly note the PE-chains directed perpendicular to the wall. These arms are object to the compression–decompression mechanism described in detail in Sec. 2.3.2 and sketched in Fig. 2.6. Moreover, the snapshots qualitatively visualize our quantitative finding that the majority of counterions is captured within the interior of a PE-star (cf. Fig. 2.4). We want to point out that, compared to the bulk case [32, 33], the counterion behavior in this regard is not significantly changed by introducing (hard) walls. In this context, we also refer to Table 2.1, where the number of condensed counterions N_1 as obtained from our MD runs is shown for different parameter combinations together with corresponding values for isolated PE-stars in unconfined geometries.

Fig. 2.9 is the core piece of this chapter and finally presents both our simulational and theoretical results for the effective star–wall forces. As can be seen from the plots, we find a very good agreement for all combinations of arm numbers and charging fractions. The theory lines exhibit a remarkable step-like shape for intermediate values of the center-to-surface distance D arising due to the introduction of the

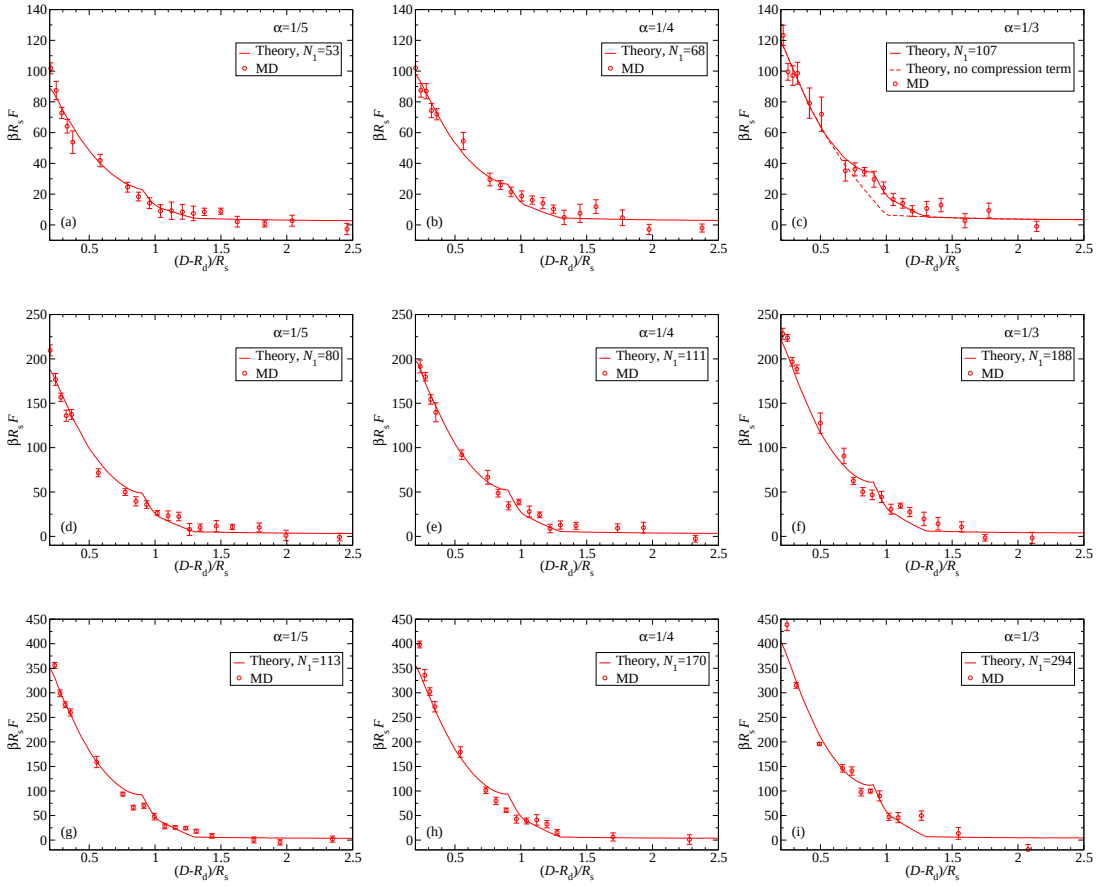

Figure 2.9: Effective star–wall forces with the colloidal core of the respective stars taken as effective coordinate, obtained from both computer simulations and our theoretical approach. The fit parameters N_1 used are specified in the legend boxes. Here, we show results for stars with functionalities $f = 10$ (first row), $f = 18$ (second row), and $f = 30$ (third row). In all cases, we are considering charging fractions $\alpha = 1/5$ (first column), $\alpha = 1/4$ (second column), and $\alpha = 1/3$ (third column). In the rightmost picture of the first row, we additionally included a theoretic line calculated without taking the compression term V_c into account to illustrate the need of such a contribution. Since the theoretical model has, in contrast to the simulation model, no (hard) colloidal core, all simulation data have to be displaced by the core radius R_d.

chain compression term F_c. The latter had to be added to the electrostatic-entropic forces F_{ee} to account for conformational changes induced by the spatial proximity of the star to the planar wall. In doing so, the functional form of the theoretically predicted forces accurately renders the results found by our computer experiments. When using the respective star's radius as basic length scale for the plots, the position of the step is independent of the parameters considered. In this sense, the effect is universal and there is no influence by specific details of the system. Note that the distinct kink is an artifact resulting from the special construction of F_c, it does not have any physical meaning. Again, it should be emphasized that the described behavior is in contrast to the well-known star–star case [32, 33]. The difference between both systems mainly lies in the fact that a star is strictly forbidden to access the region of the wall, while it is allowed to interpenetrate another star-branched macromolecule to a certain degree. To put it in other words, a wall is impenetrable, while a second star is a diffuse, soft object. Here, we also want to point out that the step is no hysteresis or metastability effect, as in our MD simulations the center-to-surface separation D is varied by pulling the stars away from the wall instead of pushing them towards it. This procedure prevents any coincidental trapping of individual PE-chains.

The particular values of the fit parameter N_1 used to calculate the theoretical curves in Fig. 2.9 are given in the corresponding legend boxes. Obviously, N_1 significantly grows with both the charging fraction α and the arm number f, as is physically reasonable. Table 2.1 compares the fit values used to their counterparts obtained by our simulations. Thereby, one recognizes systematic deviations, i.e., the fit values are always slightly off from the numbers computed using the MD method. Both quantities are of the order of 50% to 60% of the total counterion number, for all functionalities f and charging fractions α. The discrepancies emerge due to the different meanings of the quantities star radius R_s and number of condensed counterions N_1. Within the scope of the simplified theoretical model, a PE-star is a spherical object of well-defined radius, while we observe permanent conformational fluctuations of the simulated stars. Thus, the MD radius does not identify a sharp boundary, but determines a typical length scale only. In this sense, the star can be viewed as a fluffy object. Most of the time, there are monomers, monomer ions and condensed counterions located at positions outside the imaginary sphere of radius R_s, and such counterions are not counted when measuring N_1, thus the theory value typically exceeds the simulational one. With increasing arm number f and charging fraction α, there is less variation in length of different arms of a star, resulting in smaller deviations between the theoretically predicted N_1 and its MD equivalent. Table 2.1 confirms this trend.

A last remark pertains to the behavior for small center-to-surface distances D. Since our simulation model includes a colloidal core of finite radius R_d, the forces obtained from MD runs diverge for vanishing wall separations due to the core–

wall LJ repulsion which mimics the excluded volume interaction. In contrast, our theoretical model has no core, for this reason the predicted forces remain finite for the whole range of distances. According to this, our theoretical approach is basically not capable of reproducing a divergence of the forces, even in case of close proximity to the confining wall.

2.5 Conclusions

We have measured by means of MD simulations and analyzed theoretically the effective forces emerging when multi-arm PE-stars approach neutral, impenetrable walls. The forces have the typical range of the star's center-to-end radius, since osmotic PE-stars reabsorb the vast majority of the counterions and are thereby almost electroneutral; longer-range forces that could arise due to the deformation of the diffuse counterion layer outside the corona radius are very weak, due to the small population of the free counterion species. The dominant mechanism that gives rise to the soft repulsion is the entropy of the absorbed counterions and the reduction of the space available to them due to the presence of the impenetrable wall. At the same time, a novel, additional mechanism is at work, which stems from the compression of a fraction of the star chains against the hard wall. For star–wall separations that are not too different from the equilibrium star radius, the chain compression gives rise to an additional repulsive contribution to the force. At close star–wall approaches, the compressed chains 'slip away' to the side, orient themselves parallel to or away from the wall and thus the compression process ceases and the additional contribution to the force vanishes.

The compression force could play a decisive role in influencing the cross-interaction between PE-stars and spherical, hard colloids of larger diameter. Indeed, for this case, the cross-interaction can be calculated by using the results of the present chapter as a starting point and performing a Derjaguin approximation. It will be interesting to see how the cross-interaction and, in particular, compression contributions to the same affect the structural and phase behavior of such PE-star–colloid mixtures. This issue is subject of chapter 3.

Chapter 3

Fluid–fluid demixing transitions in colloid–polyelectrolyte star mixtures

In this part of the thesis, we derive effective interaction potentials between hard, spherical colloidal particles and star-branched polyelectrolytes (PE's) of various functionalities f and smaller size than the colloids. The effective interactions are calculated using a Derjaguin-like approximation, which is based on potentials acting between PE-stars and planar walls as derived in chapter 2. By virtue of the obtained colloid–PE-star cross-interactions we subsequently calculate the demixing binodals of the binary colloid–PE-star mixture, employing standard tools from liquid-state theory. We find that the mixture is indeed unstable at moderately high overall concentrations. The system becomes more unstable with respect to demixing as the star functionality and the size ratio grow.

3.1 Introduction

Though a great deal has been learned regarding the behavior of one-component solutions of PE-stars, the question of the influence of these ultra-soft colloids on solutions of hard colloids has not been investigated thus far. At the same time and as already said throughout the course of this thesis, the behavior of PE-stars in the vicinity of planar or curved hard surfaces (such as a larger colloidal particle) is an issue of considerable interest, due to the possibility of manipulating the conformation of the PE-star by suitably changing the surface's geometry or physical characteristics [92, 93, 125]. In chapter 2, the properties of PE-stars close to hard, planar walls were investigated in detail by means of computer simulations and theory, see also [126, 127]. It has been found that the geometrical constraint of the planar wall

does not affect the ability of the PE-stars to absorb the vast majority of their counterions. In addition, a new mechanism giving rise to a wall–star repulsion has been discovered, which rests on compression of stiff star chains against the neighboring wall. Now, we proceed to the full, many body problem of a collection of PE-stars and neutral colloids, which can be seen as curved walls. Basing on the results of the previous chapter, we analyze the structure of the mixture and find that it is unstable against demixing as the concentration becomes sufficiently high. This studies serve, thereby, as the reference point for our investigations on the effects of adding charge to the colloidal particles in chapter 4. It is specular to recently published work on mixtures of charged colloids with uncharged polymers [128], since in our case the colloids are neutral and the (star-branched) polymers are charged.

The rest of this chapter is organized as follows: in Sec. 3.2, we introduce the colloid–colloid and PE-star–PE-star effective interactions and we derive the cross-interaction, based on our results on the PE-star interaction potential with a planar wall. In Sec. 3.3, we present our method for calculating structure and thermodynamics by employing the aforementioned interactions in combination with two-component liquid integral equation theory. In Sec. 3.4, we present our results for various regimes of the parameter space as well as the overall phase diagrams of the mixture. Finally, in Sec. 3.5 we summarize and draw our conclusions.

3.2 Effective pair potentials

The system under investigation is a binary colloid–PE-star mixture. The colloids are coded with the subscript 'c' and the PE-stars with 's'. The mixture contains N_c spherical, neutral colloids with diameter σ_c (radius R_c) and N_s PE-stars in aqueous solution. As already explained in detail in chapter 2, the stars can be characterized by their degree of polymerization N, functionality f, and charging fraction α. Thereby, the f chains of each star are charged in a periodical manner in such a way that every $(1/\alpha)$-th monomer carries a charge $e > 0$. As a result, every star carries a total bare charge $Q_\mathrm{s} = e\alpha f N$, leaving behind $N_- = \alpha f N$ monovalent, oppositely charged counterions in the mixture due to the requirement that the system must remain electroneutral as a whole. With σ_s referring to the diameter of the stars, i.e., twice the average center-to-end distance R_s of the arms, we define the size ratio q between the two species as

$$q = \frac{R_\mathrm{s}}{R_\mathrm{c}} = \frac{\sigma_\mathrm{s}}{\sigma_\mathrm{c}}. \tag{3.1}$$

Within this work, we will only consider PE-stars that are smaller than the colloids, hence $q < 1$. The degree of polymerization of every arm, N, and the charging ratio α play a crucial role because they determine the number of released counterions N_- mentioned above. The latter are, in turn, mainly responsible for the emergence of

the star–star [26,32,33] and the star–colloid effective repulsions [126,127], due to the loss of entropy they experience when two such objects approach close to each other, see also Eq. (3.3) in what follows. Here, we fix $N = 50$ and $\alpha = 1/3$ throughout. Generalizations to other values of α and N can follow by appropriately taking into account the dependence of N_- on these parameters. Thereby, the two remaining single-molecule parameters that we vary are the functionality f of the stars and the size ratio q.

The relevant thermodynamic parameters are the partial number densities $\rho_i = N_i/\Omega$ (with $i = \mathrm{c}, \mathrm{s}$) of the respective species and the absolute temperature T. Alternatively, we can work with the concentrations $x_i = N_i/N_{\mathrm{tot}}$ and the total number density $\rho = N_{\mathrm{tot}}/\Omega$, with $N_{\mathrm{tot}} = N_{\mathrm{c}} + N_{\mathrm{s}}$ being the total particle number in the overall volume Ω of our model system. Again, we will consider constant, room temperature ($T = 300\,\mathrm{K}$) throughout this chapter, since this is the temperature for which the star–star effective interactions [32, 33] and the PE-star–planar wall potentials (see chapter 2 or Refs. [126, 127]) have been derived, based on the value $\lambda_{\mathrm{B}} = 7.1\,\text{Å}$ for the Bjerrum length in aqueous solvents. As usual, we use the inverse thermal energy $\beta = 1/(k_{\mathrm{B}}T)$, with k_{B} denoting Boltzmann's constant.

The starting point for all considerations to follow are the effective pair potentials between the constituent mesoscopic particles, having integrated out all the monomer, solvent and counterion degrees of freedom. When introducing this set of interactions as an input quantity into the full two-component integral equation theory described in more detail in Sec. 3.3, we can in principle completely access the structure and thermodynamics of the system at hand.

3.2.1 The colloid–colloid and PE-star–PE-star interactions

The effective colloid–colloid interaction at center-to-center distance r is simply taken to be a pure hard sphere (HS) potential, namely:

$$\beta V_{\mathrm{cc}}(r) = \begin{cases} \infty & r \leq \sigma_{\mathrm{c}} \\ 0 & \text{else.} \end{cases} \tag{3.2}$$

A lot of work concerning effective PE-star–PE-star interactions was done in the recent past by Jusufi and co-workers [32, 33]. They employed monomer-resolved molecular dynamics (MD) simulations and analytical theories and found an ultra-soft, bounded, density-dependent effective interaction governed by the entropic repulsions of counterions trapped in the interior of the stars. The good agreement between simulations and theory even allowed them to put forward analytic expressions for the full pair potential at arbitrary star separations. The effective potential has a weak density-dependence, but this disappears when the star density exceeds its overlap value ρ_{s}^*. In this case, all counterions are absorbed within the stars, whose

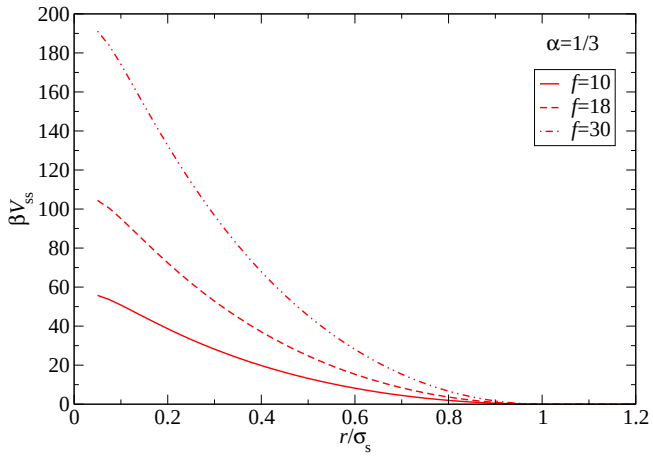

Figure 3.1: Star–star effective interaction according to Eq. (3.3), i.e., for densities ρ_s beyond the corresponding overlap concentration ρ_s^*. As expected, the potential vanishes for $r > \sigma_\mathrm{s}$, It is tunable by changing the PE stars' functionality f.

bare charges are therefore completely compensated. Thus, the effective potential vanishes identically for center-to-center distances $r > \sigma_\mathrm{s}$. For overlapping distances $r \leq \sigma_\mathrm{s}$, there is no dependence on the concentration anymore and only the trapped counterions' entropy contributes to the star–star interaction, for this reason reading for $r \leq \sigma_\mathrm{s} \equiv q\sigma_\mathrm{c}$ as [32, 33, 36, 54]:

$$\frac{\beta V_{\mathrm{ss}}(r)}{2N_2} = \ln\left\{\frac{N_2}{2\pi\left[1+\frac{r}{q\sigma_\mathrm{c}}\left(1-\ln\left(\frac{r}{q\sigma_\mathrm{c}}\right)\right)\right]}\right\} + \frac{\frac{r}{q\sigma_\mathrm{c}}\ln^2\left(\frac{r}{q\sigma_\mathrm{c}}\right)}{1+\frac{r}{q\sigma_\mathrm{c}}\left(1-\ln\left(\frac{r}{q\sigma_\mathrm{c}}\right)\right)} - \ln\left(\frac{N_2}{4\pi}\right). \tag{3.3}$$

In Eq. (3.3) above, N_2 is again the number of spherically trapped counterions of a single star. It does not coincide with the number of released counterions, N_-, because the number N_1 of Manning-condensed counterions [104] does not contribute to the effective interaction and must be excluded: thus $N_2 = N_- - N_1$. Extensive simulations [32, 33, 126, 127] have shown that the relative population of counterions in the two possible states is essentially independent of r. Thus, we fix N_1 to the value measured in our MD simulations made during the investigation of PE-stars in planar confinement in chapter 2 (see also [126, 127]). The fraction N_1/N_- typically grows with increasing α and covers ranges between 30% and 50%.

Clearly, the interaction $V_{\mathrm{ss}}(r)$ of Eq. (3.3) vanishes, along with its first derivative with respect to r, at $r = q\sigma_\mathrm{c}$, guaranteeing the smooth transition to the region

$r > q\sigma_c$, in which $V_{ss}(r) = 0$. The latter feature is, strictly speaking, valid only for star densities exceeding the overlap value ρ_s^* [36]. For $\rho_s < \rho_s^*$, a Yukawa tail exists, emerging from the Coulomb interaction between the non-neutralized PE-stars and screened by the free counterions. For the purposes of simplicity, we ignore this small contribution, because the number of released counterions from multi-arm PE-stars constitutes, at all densities, a tiny fraction of the total number of counterions N_- [33], as confirmed by the very small values of experimentally measured osmotic coefficients of PE-star solutions [37]. Finally, in order to give a better impression what the functional form of the effective PE-star–PE-star interaction $V_{ss}(r)$ looks like, Fig. 3.1 exemplarily shows it for different values of the functionality f.

3.2.2 The cross-interaction

In order to complete the set of effective pair potentials needed to describe the binary mixture within the framework of a full two-component picture, we have to specify the colloid–PE-star cross-interaction. Thereby, we proceed along the lines of Ref. [100] to derive the desired potential for small q-values based on results for the effective repulsion as obtained in chapter 2 for the case where a PE-star is brought within a distance z from a hard, flat wall, cf. also [126, 127].

To begin with, let $V_{sw}(z)$ be the star–wall interaction and $F_{sw}(z) = -\partial V_{sw}(z)/\partial z$ the corresponding force for a PE-star with all its counterions absorbed, i.e., for densities ρ_s beyond the overlap density ρ_s^* (see also previous Sec. 3.2.1). Then, for the geometry shown in Fig. 3.2(a), the force is related to the osmotic pressure $\Pi(s)$ exerted by the star on the surface of the wall via integration of the normal component of the latter along the area of contact [26]:

$$F_{sw}(z) = 2\pi \int_0^\infty \mathrm{d}y\, y\, \Pi(s) \cos\vartheta = 2\pi z \int_z^\infty \mathrm{d}s\, \Pi(s). \tag{3.4}$$

Using the above Eq. (3.4), we can directly obtain the functional form for the osmotic pressure $\Pi(z)$, provided that the functional form for the star–wall force $F_{sw}(z)$ is known:

$$\Pi(z) = -\frac{1}{2\pi}\frac{\mathrm{d}}{\mathrm{d}z}\left(\frac{F_{sw}(z)}{z}\right). \tag{3.5}$$

The same ideas can in principle be applied for a PE-star in the vicinity of a spherical, hard colloid, i.e., a hard sphere. Again, integrating the osmotic pressure along the area of contact between both objects yields the force acting on the centers of the mesoscopic particles. Pursuant to the geometry of the problem, see Fig. 3.2(b), and paying regard to the underlying symmetry, we get as result for the colloid–PE-star cross force $F_{cs}^*(z)$:

$$F_{cs}^*(z) = \frac{\pi\sigma_c^2}{2} \int_0^{\theta_{max}} \mathrm{d}\theta\, \sin\theta\, \Pi(s) \cos\vartheta. \tag{3.6}$$

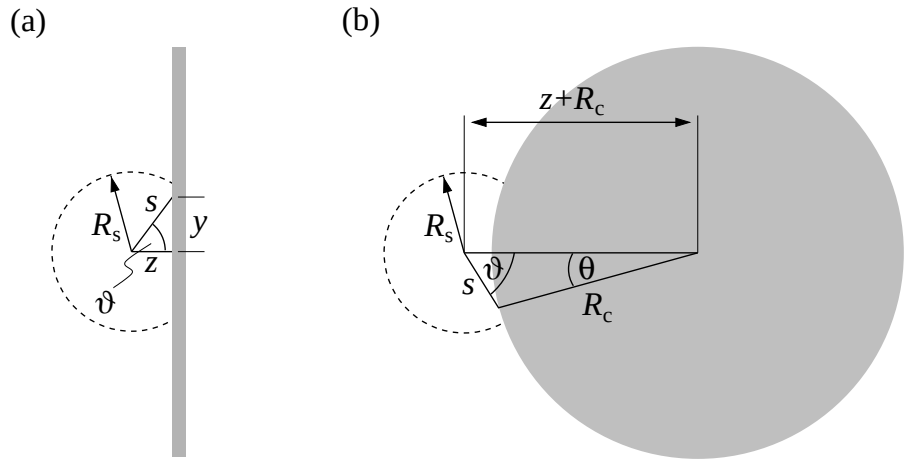

Figure 3.2: PE-star (smaller, dashed sphere) interacting with (a) a planar wall or (b) a hard colloidal particle (bigger, solid-gray sphere).

Here, the upper integration boundary $\theta_{\max}$ can be acquired by the condition that $\Pi(s)$ must vanish identically for all $\theta > \theta_{\max}$. It is possible to eliminate the polar angles ϑ and θ emanating from the centers of the PE-star and the colloid, respectively, in favor of the distance s between the star center and the point on the colloid's surface that is determined by the aforementioned angles. In doing so, we use geometrical relations evident from the sketch in Fig. 3.2(b), and finally obtain:

$$F_{\mathrm{cs}}^{*}(z) = \frac{\pi\sigma_{\mathrm{c}}}{2\left(\sigma_{\mathrm{c}}+2z\right)^{2}} \int_{z}^{s_{\max}} \mathrm{d}s \, \left[\left(\sigma_{\mathrm{c}}+2z\right)^{2} - \sigma_{\mathrm{c}}^{2} + 4s^{2}\right] \Pi(s). \tag{3.7}$$

Again, we may obtain the maximum integration distance $s_{\max}$ (without any need to calculate $\theta_{\max}$ before) simply by demanding that $\Pi(s)$ must be equal to zero for all $s > s_{\max}$. For such values of s, the integrand as a whole obviously vanishes and there are no contributions to the result of the integration anymore. Presumed the functional form for the osmotic pressure is known, such identification of $s_{\max}$ is rather easily feasible.

Since we want to consider small values $q \leq 0.3$ of the size ratio only, the stars discern the colloidal surface to be rather weakly bent compared to a flat wall, i.e., the radius of curvature is large in terms of the star radius R_{s}. Therefore, it is a reasonable approximation to assume that the osmotic pressure remains almost unchanged with respect to the situation where a PE-star is brought in contact with a planar wall. Consequently, we may combine Eqs. (3.5) and (3.7) to obtain a sound estimate for the effective force $F_{\mathrm{cs}}^{*}(z)$ as a function of distance of the star center and the colloid's surface. Note that in our special case $s_{\max}$ is of the order of the star radius R_{s}. This fact becomes evident from Eq. (3.5) if one takes into account that the typical range

for the star–wall force $F_{\mathrm{sw}}(z)$ as derived in chapter 2 is also approximately R_{s} or at the utmost slightly bigger due to effects of a chain compression at the hard wall (see below) [126, 127]. Clearly, the corresponding potential is received by a simple, one-dimensional integration:

$$V^*_{\mathrm{cs}}(z) = \int_{\infty}^{z} \mathrm{d}z'\, F^*_{\mathrm{cs}}(z'). \tag{3.8}$$

In Fig. 3.3 we show the shape of $V^*_{\mathrm{cs}}(z)$ for $q = 0.2$ and different values of the stars' functionality f. In order to demonstrate the importance of the compression term adding to the star–wall force F_{sw} besides electrostatic-entropic contributions [126, 127], we additionally included colloid–star potentials calculated on the basis of the electrostatic and entropic star–wall forces alone. Since there are striking deviations, we can clearly expect such devolved compression effects to influence the phase behavior of the mixture.

Finally, we need to express the effective potential as a function of the particles' center-to-center separation r instead of the center-to-surface distance z. Thereby, we have to take into account that the star center is strictly forbidden to penetrate the volume of the colloid. Thus, the total cross-interaction features a hard core plus the soft, purely repulsive tail as obtained from the above Eq. (3.8) and finally writes as:

$$V_{\mathrm{cs}}(r) = \begin{cases} \infty & r \leq \sigma_{\mathrm{c}}/2 \\ V^*_{\mathrm{cs}}(r - \sigma_{\mathrm{c}}/2) & \text{else.} \end{cases} \tag{3.9}$$

3.3 Determination of the structure and thermodynamics of the mixture

In this section, we describe the basic principles of liquid integral equation theory for binary mixtures[1] and how to subsequently access the thermodynamics of the system. In general, the pair structure of the system at hand (and analogously any other two-component system) is fully described by three independent total correlation functions $h_{ij}(r)$ with $i, j = \mathrm{c}, \mathrm{s}$. Hereby, we already allowed for the symmetry with respect to exchange of the indices, i.e., $h_{ij}(r) = h_{ji}(r)$. Closely related to the total correlation functions are the so-called direct correlation functions (dcf's) $c_{ij}(r)$. Following the same symmetry argument again, there exist only three independent dcf's. In what follows, we will denote the Fourier transforms of $h_{ij}(r)$ and $c_{ij}(r)$ as $\tilde{h}_{ij}(r)$ and $\tilde{c}_{ij}(r)$, respectively.

[1] A further generalization of the theoretical approach from $\nu = 2$ to $\nu > 2$ components in the mixture is straight-forward. But since we are only interested in binary systems within the framework of this chapter, we limit ourselves to that special case in order to keep all delineations as concise as possible.

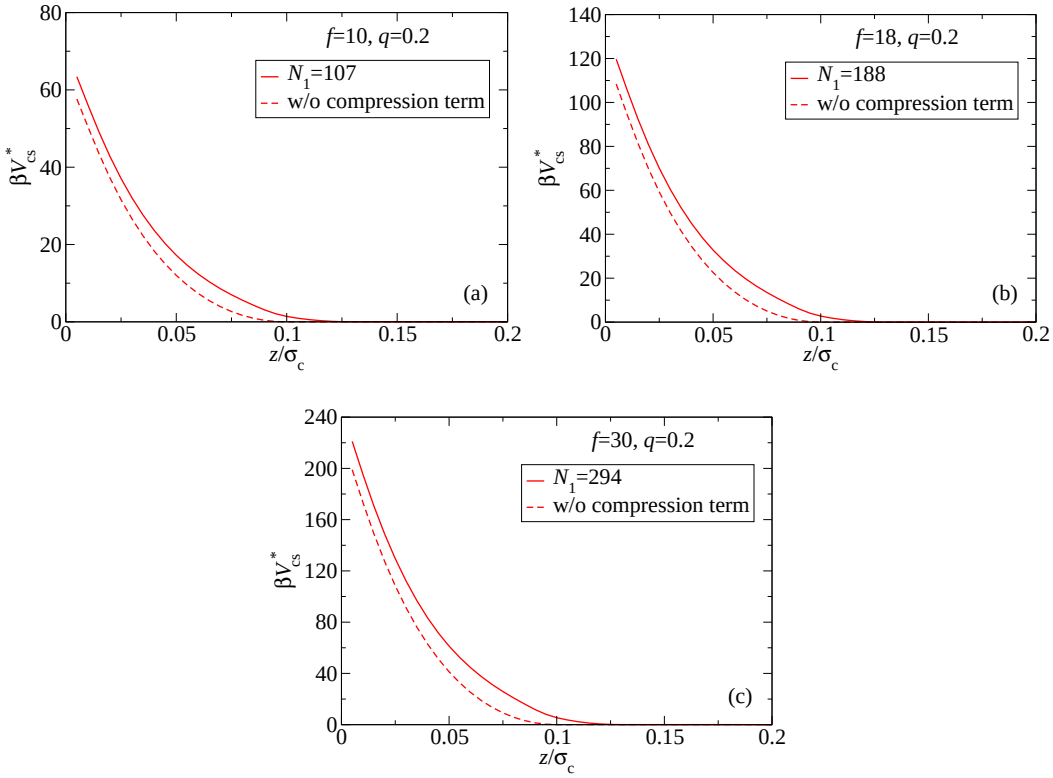

Figure 3.3: Effective colloid–PE-star potentials with and without provision for compression effects as a function of the center-to-surface distance z. Here, we have chosen the parameters $q = 0.2$ and (a) $f = 10$, (b) $f = 18$, and (c) $f = 30$. In the legend boxes, the numbers of condensed counterions N_1 used as fit parameters in chapter 2 are specified for sake of completeness.

The above-mentioned connection between the total and direct correlation functions is quantitatively incorporated via the multi-component generalization of the well-known and commonly used Ornstein-Zernike (OZ) relation, which in its Fourier space representation reads as [121, 129, 130]:

$$\tilde{\mathbf{H}}(k) = \tilde{\mathbf{C}}(k) + \tilde{\mathbf{C}}(k) \cdot \mathbf{D} \cdot \tilde{\mathbf{H}}(k). \tag{3.10}$$

Here, $\tilde{\mathbf{H}}(k)$ and $\tilde{\mathbf{C}}(k)$ are symmetric (2×2)-matrices whose elements are constituted by the total and direct correlation functions, respectively, and $\mathbf{D}$ is a diagonal (2×2)-matrix containing the partial densities characterizing the composition of the system under investigation, i.e.,

$$\left[\tilde{\mathbf{H}}(k)\right]_{ij} = \tilde{h}_{ij}(k), \tag{3.11}$$

$$\left[\tilde{\mathbf{C}}(k)\right]_{ij} = \tilde{c}_{ij}(k), \tag{3.12}$$

$$\left[\mathbf{D}\right]_{ij} = \rho_i \delta_{ij}. \tag{3.13}$$

Evidently, Eq. (3.10) can be rewritten yielding the equivalent matrix relation

$$\tilde{\mathbf{H}}(k) = \left[\mathbf{1} - \tilde{\mathbf{C}}(k) \cdot \mathbf{D}\right]^{-1} \cdot \tilde{\mathbf{C}}(k), \tag{3.14}$$

with the identity matrix $\mathbf{1}$ and the matrix inverse $[\mathbf{1} - \tilde{\mathbf{C}}(k) \cdot \mathbf{D}]^{-1}$. Defining $\Delta(k) \equiv \rho_\mathrm{s}\rho_\mathrm{c}[\tilde{c}_\mathrm{ss}(k)\tilde{c}_\mathrm{cc}(k) - \tilde{c}^2_\mathrm{cs}(k)]$ and $E(k) \equiv \rho_\mathrm{s}\tilde{c}_\mathrm{ss}(k) + \rho_\mathrm{c}\tilde{c}_\mathrm{cc}(k)$ and returning to a component-by-component notation, Eq. (3.14) can consistently be expressed in the following fashion:

$$\tilde{h}_{ij}(k) = \frac{\tilde{c}_{ij}(k) - \rho_i^{-1} \cdot \Delta(k) \cdot \delta_{ij}}{1 + \Delta(k) - E(k)}. \tag{3.15}$$

The linear algebraic system of Eq. (3.15) provides three independent equations coupling six yet unknown functions $\tilde{h}_{ij}(k)$ and $\tilde{c}_{ij}(k)$. In order to completely determine that set of functions, we therefore need to supply three additional relations to close and subsequently solve the system of equations. There are several popular choices for these so-called closures, e.g., the Percus-Yevick (PY) or hypernetted-chain (HNC) approximations in their respective two-component generalizations. While the former is known to generate reliable results for short-range interactions, the latter furnishes very accurate estimates for the pair structure in case of long-range, soft potentials. Neither the PY nor the HNC closure are thermodynamically consistent, however, and in our case this is a crucial factor, since we are interested in the calculation of phase boundaries, which should not depend on the route chosen to calculate the free energies. Thus, we resort to the Rogers-Young (RY) closure [131],

in which thermodynamic consistency can be enforced. In its multi-component version the RY-closure reads as:

$$g_{ij}(r) = \exp\left[-\beta V_{ij}\right] \cdot \left\{1 + \frac{\exp\left[\chi_{ij}(r) f_{ij}(r)\right] - 1}{f_{ij}(r)}\right\}, \tag{3.16}$$

where $g_{ij}(r) = h_{ij}(r) + 1$ are the so-called radial distribution functions and we introduced new auxiliary functions $\chi_{ij}(r) = h_{ij}(r) - c_{ij}(r)$. $V_{ij}(r)$ refers to the pair interactions between species i and j as presented in Sec. 3.2. It may be again emphasized that the main benefit we gain from using the modified relation (3.16) is closely related to the hybrid character of the latter. Due to the fact that any closure constitutes an approximation, we in general obtain different results for the partial and total isothermal compressibilities as calculated via either the virial or the fluctuation route (see below), as already mentioned above. But the three mixing functions emerging in Eq. (3.16) and given by

$$f_{ij}(r) = 1 - \exp\left[-\zeta_{ij} r\right], \tag{3.17}$$

with ζ_{ij} being the so-called self-consistency parameters, now allow us to address this problem and to appropriately match the isothermal compressibilities. Since it is sufficient to apply a single consistency condition only, namely the requirement of equality of the system's total virial and fluctuation isothermal compressibilities, the usual approach is to employ just one individual parameter $\zeta_{ij} = \zeta$ for all components. Hence, only a single mixing function $f_{ij}(r) = f(r)$ remains. However, multi-parameter versions of the RY closure have nevertheless also been proposed some years ago [132], accordingly demanding the equality of all the partial compressibilities. It is easy to check that for $\zeta = 0$ and $\zeta = \infty$ the multi-component PY and HNC closures, respectively, are recovered from Eq. (3.16)[2].

Now, we have to address in more detail the issue of calculating the total isothermal compressibility following the different routes. At first, we concern ourselves with the virial compressibility κ_T^{v}. The total pressure P of the system at hand, including both ideal and excess contributions, takes the form [130]:

$$\beta P = \rho - \frac{2\pi\rho^2}{3} \sum_i \sum_j x_i x_j \int_0^\infty \mathrm{d}r\, r^3\, V_{ij}'(r)\, g_{ij}(r), \tag{3.18}$$

with $V_{ij}'(r) = -\partial V_{ij}(r)/\partial r$ being the different pair potentials' derivatives with respect to the inter-particle distance r. Provided the pressure pursuant to Eq. (3.18)

[2] When using the RY closure, the correlation functions obviously – besides their inherent density dependence – parametrically depend on the mixing parameter ζ, i.e., $h_{ij} = h_{ij}(r; \rho_{\mathrm{c}}, \rho_{\mathrm{s}}, \zeta)$ and $c_{ij} = c_{ij}(r; \rho_{\mathrm{c}}, \rho_{\mathrm{s}}, \zeta)$. The same must obviously hold for all quantities deduced from these two functions. Note that we will nevertheless drop both the ρ_i's and ζ from the respective parameter lists in order not to overcrowd our notation.

is known, κ_T^{v} can be obtained by differentiating with respect to the total density ρ while the partial concentrations x_i are kept fixed:

$$\rho k_{\mathrm{B}} T \kappa_T^{\mathrm{v}} = \left[\left. \frac{\partial(\beta P)}{\partial \rho} \right|_{\{x_i\}} \right]^{-1}. \tag{3.19}$$

In order to evaluate the fluctuation compressibility κ_T^{fl}, we initially introduce the three partial structure factors $S_{ij}(k)$. As the correlation functions and the radial distribution functions, respectively, they also describe the structure of the system:

$$S_{ij}(k) = \delta_{ij} + \sqrt{\rho_i \rho_j} \tilde{h}_{ij}(k). \tag{3.20}$$

While for the one-component case the compressibility can simply be obtained as the $(k = 0)$-value of the static structure factor, i.e., $S(k = 0) = \rho k_{\mathrm{B}} T \kappa_T^{\mathrm{fl}}$, things are a bit more complicated for binary (or multi-component, $\nu > 2$) mixtures. Here, in generalization of the one-component situation, the compressibility can finally be written using the following expression [16, 133, 134]:

$$\rho k_{\mathrm{B}} T \kappa_T^{\mathrm{fl}} = \frac{S_{\mathrm{ss}}(0) S_{\mathrm{cc}}(0) - S_{\mathrm{cs}}^2(0)}{x_{\mathrm{c}} S_{\mathrm{ss}}(0) + x_{\mathrm{s}} S_{\mathrm{cc}}(0) - 2\sqrt{x_{\mathrm{s}} x_{\mathrm{c}}} S_{\mathrm{cs}}^2(0)}. \tag{3.21}$$

Based on the knowledge of the partial correlation functions $h_{ij}(r)$ and structure factors $S_{ij}(k)$ as obtained by (numerically) solving the OZ relation, Eq. (3.10), and using the RY closure, Eq. (3.16), we can in principle completely access the thermodynamics of the system at hand. In order to calculate the binodal lines, a very convenient quantity to consider is the concentration structure factor $S_{\mathrm{con}}(k)$. It is a linear combination of all the partial structure factors, whereby the corresponding pre-factors are determined by the different species' concentrations x_i, namely:

$$S_{\mathrm{con}}(k) = x_{\mathrm{c}} x_{\mathrm{s}}^2 S_{\mathrm{cc}}(k) + x_{\mathrm{s}} x_{\mathrm{c}}^2 S_{\mathrm{ss}}(k) - 2(x_{\mathrm{c}} x_{\mathrm{s}})^{3/2} S_{\mathrm{cs}}(k). \tag{3.22}$$

Now, let P be the total pressure according to the above Eq. (3.18) and $g(x_{\mathrm{s}}, P, T) = G(x_{\mathrm{s}}, N_{\mathrm{tot}}, P, T)/N_{\mathrm{tot}}$ the Gibbs free energy $G(x_{\mathrm{s}}, N_{\mathrm{tot}}, P, T)$ per particle. Then, the second derivative of the former is connected to the concentration structure factor $S_{\mathrm{con}}(k)$ by means of the sum rule [135–137]

$$\beta g''(x_{\mathrm{s}}, P, T) \equiv \beta \frac{\partial^2 g(x_{\mathrm{s}}, P, T)}{\partial x_{\mathrm{s}}^2} = \frac{1}{S_{\mathrm{con}}(0; x_{\mathrm{s}})}, \tag{3.23}$$

where we have added the concentration x_{s} as a second argument to $S_{\mathrm{con}}(k)$ to emphasize this dependence. This differential equation has to be integrated along an isobar for any prescribed value of the pressure $P^* \equiv \beta P \sigma_{\mathrm{c}}^3 = \text{const.}$, to obtain the

Gibbs free energy from the structural data, $S_{\mathrm{con}}(k = 0; x_{\mathrm{s}})$. A detailed analysis of the limiting behavior of $g''(x_{\mathrm{s}})$ shows a divergence as $1/x_{\mathrm{s}}$ for $x_{\mathrm{s}} \to 0$ and as $1/(1 - x_{\mathrm{s}})$ for $x_{\mathrm{s}} \to 1$ [137]. In order to avoid any technical difficulties when numerically integrating, we *a priori* split the Gibbs free energy $g(x_{\mathrm{s}})$ into a term that arises from its ideal part and a remainder, which we call excess part[3], $g_{\mathrm{ex}}(x_{\mathrm{s}})$:

$$\begin{aligned}\beta g(x_{\mathrm{s}}) =&(1 - x_{\mathrm{s}}) \ln(1 - x_{\mathrm{s}}) + x_{\mathrm{s}} \ln(x_{\mathrm{s}}) \\ &+ 3(1 - x_{\mathrm{s}}) \ln(\Lambda_{\mathrm{c}}/\sigma_{\mathrm{c}}) + 3x_{\mathrm{s}} \ln(\Lambda_{\mathrm{s}}/\sigma_{\mathrm{c}}) + \beta g_{\mathrm{ex}}(x_{\mathrm{s}}),\end{aligned} \tag{3.24}$$

with the thermal de-Broglie wavelengths $\Lambda_{\mathrm{c,s}}$ of the colloids and the stars, respectively. Taking the second derivative in the above Eq. (3.24) again, we obtain:

$$\beta g''(x_{\mathrm{s}}) = \frac{1}{x_{\mathrm{s}}} + \frac{1}{1 - x_{\mathrm{s}}} + g''_{\mathrm{ex}}(x_{\mathrm{s}}). \tag{3.25}$$

Thus, the ideal part of the Gibbs free energy is exclusively responsible for the appearance of the aforementioned divergences at the integration boundaries and the modified second-order differential equation

$$\beta g''_{\mathrm{ex}}(x_{\mathrm{s}}) = \frac{1}{S_{\mathrm{con}}(0; x_{\mathrm{s}})} - \left(\frac{1}{x_{\mathrm{s}}} + \frac{1}{1 - x_{\mathrm{s}}} \right) \tag{3.26}$$

for the excess Gibbs free energy alone is obviously free of any diverging terms. We can therefore easily solve it numerically. Subsequent addition of the analytically known ideal term $g_{\mathrm{id}}(x_{\mathrm{s}}) = (1 - x_{\mathrm{s}}) \ln(1 - x_{\mathrm{s}}) + x_{\mathrm{s}} \ln(x_{\mathrm{s}})$ directly yields the total Gibbs free energy per particle that we are interested in. The two terms involving the thermal de-Broglie wavelength are linear in x_{s}; they only provide a shifting of the chemical potentials and can be dropped.

Thermodynamic stability requires that $g(x_{\mathrm{s}})$ is convex [138]. In case we encounter some x_{s}-region where $g''(x_{\mathrm{s}}) < 0$ the binary mixture features a fluid–fluid demixing transition. In that sense, Eqs. (3.23) and (3.26), respectively, allow us to investigate the thermodynamics and the phase behavior of the system at hand by providing a tool to compute the Gibbs free energy (per particle). The corresponding phase boundaries can be calculated using Maxwell's common tangent construction, which guarantees that the chemical potentials, μ_i, are the same between both coexisting phases. Since we are in a situation where we moreover fixed the pressure P^* of the mixture and its absolute temperature T, all conditions for phase coexistence are clearly fulfilled. Concretely, the common tangent construction amounts to solving the coupled equations

$$g'(x_{\mathrm{s}}^{\mathrm{I}}) = g'(x_{\mathrm{s}}^{\mathrm{II}}) \tag{3.27}$$

[3]The 'excess' part $g_{\mathrm{ex}}(x_{\mathrm{s}})$ in Eq. (3.24), includes a term $\ln(\rho\sigma_{\mathrm{c}}^3)$ that arises from the original ideal part but which does not cause any divergences at the limits $x_{\mathrm{s}} \to 0$ and $x_{\mathrm{s}} \to 1$, which we seek to remove. Thus we readsorb it into a redefined excess part, which can be integrated without problems.

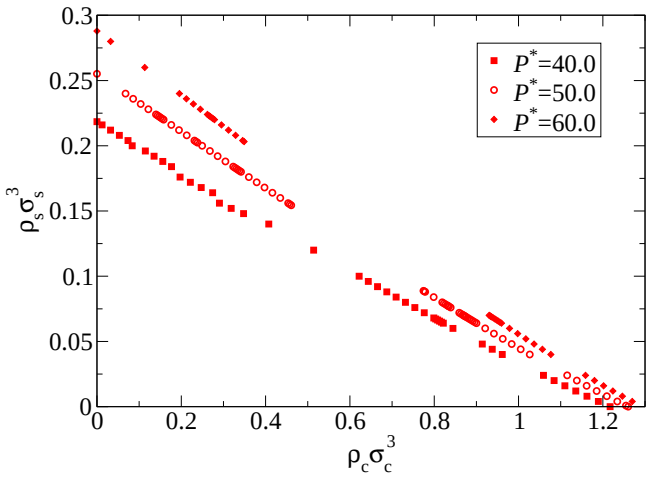

Figure 3.4: Position and shape of isobars $P^* = \beta P \sigma_c^3 = \text{const.}$ in the (ρ_c, ρ_s)-plane as computed starting from solutions of the OZ relation, exemplarily shown for $(f = 30)$-arm PE-stars and a size ratio $q = 0.2$. For the higher values of the pressure, namely $P^* = 50.0$ and $P^* = 60.0$, there are parts of the density plane emerging where it is not possible to numerically solve the integral equations anymore, thus the isobars display 'gaps' that are indicators of the ensuing coexistence region.

and

$$g(x_s^{\mathrm{I}}) - x_s^{\mathrm{I}} g'(x_s^{\mathrm{I}}) = g(x_s^{\mathrm{II}}) - x_s^{\mathrm{II}} g'(x_s^{\mathrm{II}}) \tag{3.28}$$

for the concentrations $x_s^{\mathrm{I,II}}$ of the coexisting phases I and II.

In integrating Eq. (3.25) and adding the ideal terms, one obtains the Gibbs free energy per particle, $g(x_s)$ modulo an undetermined linear function $C_1 x_s + C_0$ with the constants C_1 and C_0 to be fixed by appropriate boundary conditions. As is clear from Eqs. (3.27) and (3.28) above, such a linear term is anyway immaterial from the determination of phase boundaries and, in practice, it can be ignored on the same grounds that the terms involving the thermal de-Broglie wavelengths in Eq. (3.24) have been dropped. Nevertheless, the constants C_1 and C_0 can be determined as follows. Taking into account that the Gibbs free energy $G(x_s, N_{\mathrm{tot}}, P, T)$ is an extensive function but in its natural argument list there is only one extensive variable, namely the number of particles N_{tot}, Euler's theorem [10] asserts the function g to have the form:

$$g(x_s) = x_s \mu_s(x_s) + (1 - x_s)\mu_c(x_s). \tag{3.29}$$

For both limiting one-component cases, i.e., if no stars ($x_s = 0$) or no colloids ($x_s = 1$) are present in the system, the following relation holds true:

$$\beta g = \hat{f} + \rho \hat{f}' = \ln(\rho) + \hat{f}_{\mathrm{ex}} + \rho \hat{f}'_{\mathrm{ex}}, \tag{3.30}$$

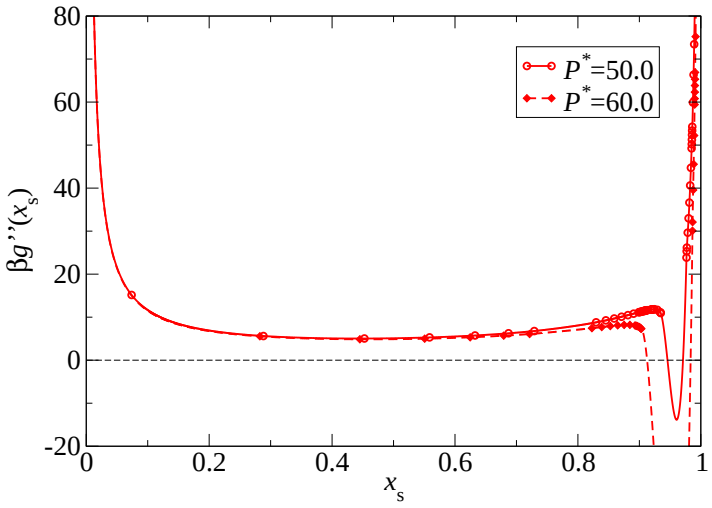

Figure 3.5: Examples of the second derivative of the Gibbs free energy per particle, $g''(x_\mathrm{s})$, plotted against the star concentration x_s for stars with functionality $f = 30$, PE-star–colloid size ratio $q = 0.2$, and two different pressures $P^* = \beta P \sigma_\mathrm{c}^3$. Symbols are calculated from the OZ relation, lines were obtained by cubic spline interpolation. Note that the x_s-interval where we are not able to numerically solve the integral equations grows distinctly upon increasing the pressure, i.e., as we move away from the critical point. Moreover, the plot illustrates the limiting behavior of $g''(x_\mathrm{s})$ as $1/x_\mathrm{s}$ for $x_\mathrm{s} \to 0$ and as $1/(1-x_\mathrm{s})$ for the opposite case $x_\mathrm{s} \to 1$, respectively.

where $\hat{f} = \beta F / N_\mathrm{tot}$ denotes the Helmholtz free energy per particle and $\hat{f}'$ its derivative with respect to the density ρ; the subscript 'ex' refers to the excess part of $\hat{f}$. On the other hand, $\hat{f}'_\mathrm{ex}$ is connected to the excess pressure P_ex [as known from Eq. (3.18) above] via the equation

$$\hat{f}'_\mathrm{ex} = \beta P_\mathrm{ex} / \rho^2. \tag{3.31}$$

Following Eq. (3.31), $\hat{f}_\mathrm{ex}$ can be obtained by integrating the ratio P_ex/ρ^2 with respect to ρ and applying the additional boundary condition $\hat{f}_\mathrm{ex}(\rho \to 0) = 0$. Once the Helmholtz free energies for the pure colloid and PE-star systems are known this way, the corresponding chemical potentials $\mu_\mathrm{c}(0)$ and $\mu_\mathrm{s}(1)$ can be calculated and the conditions $g(0) = \mu_\mathrm{c}(0)$ and $g(1) = \mu_\mathrm{s}(1)$ for any arbitrary pressure P [cf. Eqs. (3.29) and (3.30) above] yield C_0 and C_1. Note that for the pure colloidal system, $x_\mathrm{s} = 0$, we can avoid the integration route to compute the pressure by using the accurate Carnahan-Starling expressions for hard spheres [139]. The pressure obtained this way turns out to be consistent with the one calculated from the Rogers-Young route, based on Eq. (3.18) and our results for the radial distribution function $g(r)$.

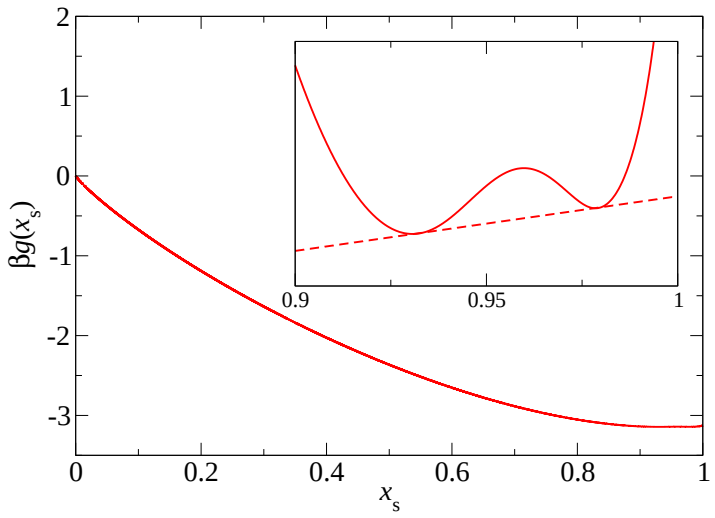

Figure 3.6: Gibbs free energy per particle $g(x_\mathrm{s})$ vs. the star concentration x_s, plotted for $f = 30$, $q = 0.2$, and $P^* = 50.0$. The curve was obtained via integrating the interpolated function $g''(x_\mathrm{s})$ twice according to the procedure delineated in the main text, whereby we subtracted an arbitrary linear function afterwards. The corresponding inset shows $g(x_\mathrm{s})$ with an differently scaled x_s-axis in order to highlight the concave parts of the function and to show Maxwell's common tangent construction in detail.

Note that when crossing the spinodal line in the density plane the long wavelength limits of the partial structure factors, $S_{ij}(k \to 0)$, take non-physical values. This behavior expresses the system's physical instability against a possible fluid–fluid phase separation. Thereto, it is no longer feasible to (numerically) solve the integral equations once we reached the spinodal; in fact, integral equation theories themselves break down before the spinodal is reached, yet after the binodal [140]. Consequently, depending on the total pressure and above a certain threshold value of the same, $P > P_\mathrm{thr}$, the concentration structure factor $S_\mathrm{con}(0; x_\mathrm{s})$ is unknown over some interval $\Delta x_\mathrm{s}(P)$. Hence, we need to appropriately interpolate $S_\mathrm{con}(0; x_\mathrm{s})$ in order to obtain the second derivative of the Gibbs free energy per particle for all $0 \leq x_\mathrm{s} \leq 1$ and, in this way, to allow for the integration of the differential equations (3.23) or (3.26), respectively. Along the lines of Ref. [137], we perform this necessary interpolation using cubic splines. In order to illustrate the whole procedure, Fig. 3.4 exemplarily depicts the shape of the isobars in the $(\rho_\mathrm{c}, \rho_\mathrm{s})$-plane as obtained via the integration route for various pressures P^* and a representative parameter combination, while for the same values of f and q Fig. 3.5 shows the function $g''(x_\mathrm{s})$ as computed from the OZ equation together with its cubic spline interpolation, again for two different pressures P^*. Moreover, in Fig. 3.6, we plotted the corresponding

Gibbs free energy $g(x_\mathrm{s})$ for a pressure $P^* = 50.0$. In addition, the inset depicts Maxwell's common tangent construction used to calculate the star concentrations for the coexisting fluid phases.

It may be emphasized that the results for the binodal do not depend on the concrete interpolation scheme, at least as long as the numerical methods used to solve the OZ relation are able to precisely reach the spinodal, i.e., the points where the structure factors diverge for $k \to 0$. Admittedly, this is not always strictly the case since the numerical schemes we employed to calculate correlation functions and corresponding structure factors, respectively, may break down slightly before the spinodal is reached. Accordingly, small inaccuracies induced by the interpolation procedure arise which grow with increasing width of the gap region $\Delta x_\mathrm{s}(P)$, or to put it in other words, with increasing pressure P, i.e., if we move away from the critical point. As long as the aforementioned interval where no solution of the integral equations can be found is rather small, we expect the interpolation to be reliable, while for higher pressures the received binodals are of more approximate character. Nevertheless, they still show a very reasonable behavior. We are going to discuss the results for the phase diagrams in detail in Sec. 3.4.3.

3.4 Results

3.4.1 Low colloid-density limit

Based on the radial distribution functions $g_{ij}(r)$ as obtained by the OZ relation closed with the RY closure, Eqs. (3.10) and (3.16), we may map our two-component mixture onto an effective one-component system of the colloids alone. In doing so, the PE-stars are completely traced out, resulting into an effective colloid–colloid interaction where the pure hard sphere potential is masked by additional depletion contributions originating in the presence of the stars and the forces they exert on the colloids. To put it in other words, the colloid–PE-star interactions cause spatial correlations of the PE-star distribution in the vicinity of the colloids, and it is exactly these correlations that determine the resulting shape of the depletion potential. Note that the latter in general parametrically depends rather on the PE-stars' chemical potential μ_s or, equivalently, the density $\rho_\mathrm{s}^\mathrm{r}$ of a reservoir of stars at the same chemical potential $\mu_\mathrm{s}^\mathrm{r} = \mu_\mathrm{s}$, than on their density ρ_s in the real system. Hence, it is in principle more convenient to switch to a reservoir representation $(\rho_\mathrm{c}, \rho_\mathrm{s}^\mathrm{r})$ of the partial densities instead of the original system representation $(\rho_\mathrm{c}, \rho_\mathrm{s})$ when considering such effective interactions. Clearly, if the colloid density ρ_c takes finite values, it must hold $\rho_\mathrm{s} \neq \rho_\mathrm{s}^\mathrm{r}$. But since we will consider the limiting case of low colloid densities $\rho_\mathrm{c} \to 0$ only in what follows, we have $\rho_\mathrm{s}^\mathrm{r} = \rho_\mathrm{s}$ again, i.e., reservoir and system representation of the partial densities coincide.

Concretely, the desired mapping[4] can be achieved by a so-called inversion of the full, two-component results of the integral equations in the low colloid-density limit $\rho_c \to 0$ [137, 141, 146–148]. It can be shown from diagrammatic expansions in the framework of the theory of liquids [129] that in this limit the pair correlation function for any fluid reduces to the Boltzmann factor $g(r) = \exp[-\beta v(r)]$. Here, $v(r)$ denotes the pair potential the fluid's constituent particles interact by. According to this relation, the effective colloid–colloid potential $V_{\mathrm{depl}}(r)$, depending parametrically on both the partial colloid and star densities ρ_c and $\rho_s^r = \rho_s$, is obtained as follows:

$$\beta V_{\mathrm{depl}}(r) = \lim_{\rho_c \to 0} \ln \left[g_{cc}(r; \rho_c, \rho_s^r) \right] . \tag{3.32}$$

Fig. 3.7 shows examples for the effective colloid–colloid interaction $V_{\mathrm{depl}}(r)$ for different functionalities f of the stars, partial star densities $\rho_s^r = \rho_s$, and PE-star–colloid size ratios q. As one can see from the plots, for distances $r > \sigma_c$ the resulting depletion interaction mediated by the stars is attractive and features a slightly oscillating behavior, while for inter-particle separations $r \leq \sigma_c$ the bare hard sphere repulsion remains. In particular, Fig. 3.7(a) illustrates that the addition of PE-stars to the mixture results in both a significant increase of the depth of the attractive potential well and a further enhancement of the aforementioned oscillations but does in no way affect the range of the attraction. As can be read off from Fig. 3.7(b), the latter is determined by the size ratio q alone and grows linearly with the diameter of the stars. Furthermore, there is a measurable, but weak, dependence of the interaction strength on the functionality of the PE-stars: the higher the arm number f the stronger becomes the effective attraction between two colloids [cf. Fig. 3.7(c)]. All these trends are in perfect agreement with the common understanding of the physical mechanisms leading to the appearance of such an effective attraction: due to a depletion of the PE-stars in the spatial region between a pair of colloids, and dependent on the colloids' mutual distance, they are hit asymmetrically by the stars from the inside and the outside. Consequently, the unbalanced osmotic pressure pushes the colloids together. Clearly, the absolute value of this force must grow when increasing the star density ρ_s, simply because there are more collisions between PE-stars and colloids. For higher functionalities f, the colloid–PE-star cross-interaction becomes more repulsive (see Sec. 3.2.2), i.e., the stars push the colloids harder, thus also leading to a strengthened effective colloid–colloid attraction. And finally, the diameter of the PE-stars determines whether or not they fit into the spatial region

[4] Note that the most accurate way to compute effective interactions between two colloidal particles in the presence of (smaller) PE-stars is to employ direct computer simulations [137, 141–144]. Another way to the depletion potential would in principle be offered by Attard's so-called superposition approximation (SA) [145]. But since we want to perform the mapping onto an effective one-component system in order to gain some qualitative understanding of the physics of our system only but stick to the full two-component picture to quantitatively calculate the binodals of the mixture, we turn down such alternative methods within the scope of the thesis at hand.

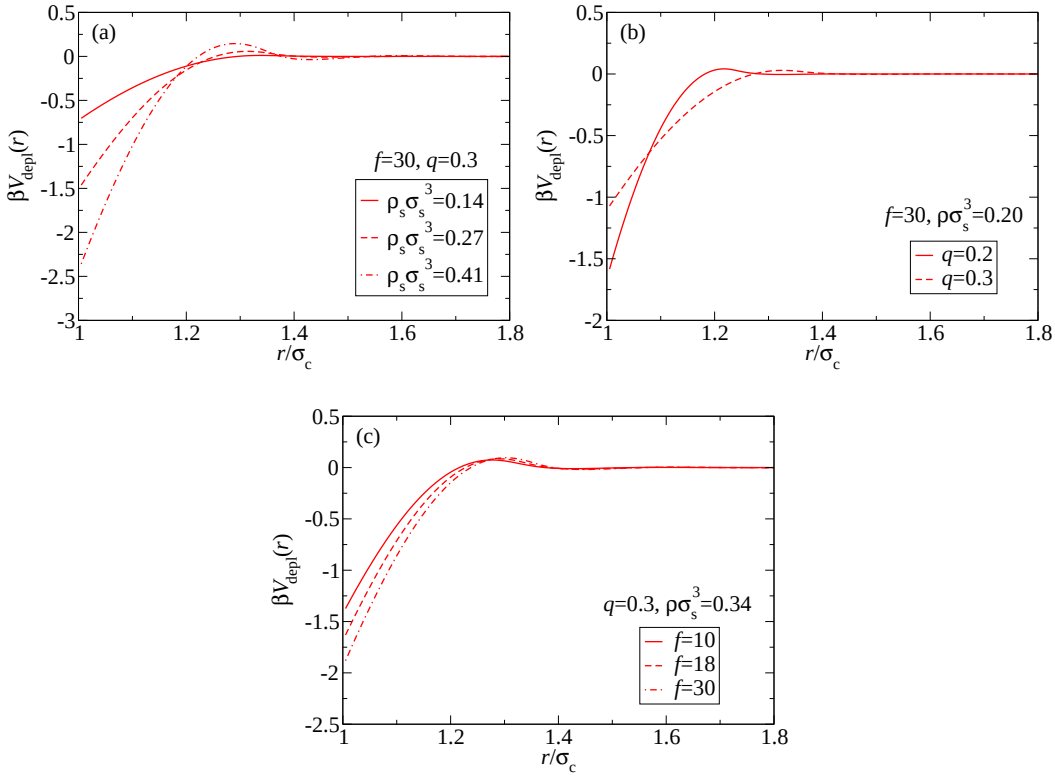

Figure 3.7: Effective colloid–colloid depletion potentials $V_{\mathrm{depl}}(r)$ as obtained by an inversion of the OZ relation. For details concerning the procedure, see main text. We have investigated the influence of (a) the partial star density $\rho_{\mathrm{s}}^{\mathrm{r}} = \rho_{\mathrm{s}}$, (b) the PE-star–colloid size ratio q, and (c) the functionality f of the stars on the functional form of the interaction potential. It is evident from the plots that the presence of the stars induces an attraction between the colloids in addition to their bare hard sphere repulsion which takes over for distances $r \leq \sigma_{\mathrm{c}}$.

between a pair of colloids for a given distance of the two. Hence, the size ratio q controls if the stars are expelled from the said region of space, or to put it in other words, for what scope of inter-colloidal separations depletion actually takes place. Thus, the range of the effective force can be altered by changing q.

The occurrence of oscillations of the effective potential $V_{\mathrm{depl}}(r)$ obviously means that the attractive minimum is followed by a repulsive barrier whose height is set by the concentration of PE-stars in the mixture (see above). In particular, it grows upon addition of stars to the system and such behavior could, in case of distinctly high and broad maxima, in principle lead to micro-phase separation, i.e., cluster formation [149–153]. But for the physical system we examine and the range of parameters we investigate, the barrier remains anyway rather low and narrow. Micro-phase separation is therefore not likely to happen. Instead, the type of effective colloid–colloid attractions at hand, i.e., an attractive potential valley together with a nearly vanishing or at least less-pronounced repulsive barrier, forces the system to develop long-range fluctuations upon an increase of the PE-star concentration, consequently favoring the possibility of a fluid–fluid demixing transition of the two-component mixture. Such behavior is frequently observed in, e.g., colloid–polymer mixtures [154–156]. Thus, when considering the phase behavior of our system by calculating its binodals, we expect to find evidence for macro-phase separation. This anticipated result will be confirmed by the results of the following section.

3.4.2 Structure of the mixture

Before switching over to a presentation of the demixing binodals as obtained via the procedure described in detail in Sec. 3.3, i.e., initially calculating the Gibbs free energy $g(x_{\mathrm{s}})$ with both the temperature T and the pressure P kept fixed and subsequently identifying the sought-for coexisting fluid phases using Maxwell's common tangent construction for the concave parts of that function (see, in particular, Figs. 3.5 and 3.6), it is useful to study partial pair correlation functions $g_{ij}(r)$ and corresponding structure factors $S_{ij}(k)$ $(i, j = \mathrm{c}, \mathrm{s})$ first. Since these quantities completely describe the pair structure of the system, we are able to gain detailed insight into the physics and phase behavior of the mixture and to discover, in addition to the findings of the previous Sec. 3.4.1, more evidence that it is reasonable to expect a mixing–demixing transition.

Fig. 3.8 shows the partial radial distribution functions $g_{ij}(r)$ for typical parameters, namely a colloid–PE-star mixture with a size ratio of $q = 0.3$ and the PE-stars having $f = 30$ arms each. We show results for different mixture compositions, i.e., varying the partial densities for both species as indicated in the plots. Figs. 3.8(a) and (b), on the one hand, depict the decisive length scales of the problem or, equivalently, the typical ranges of the underlying pair potentials as set by the sizes of colloids and PE-stars, respectively. The distinct height of the colloid–colloid con-

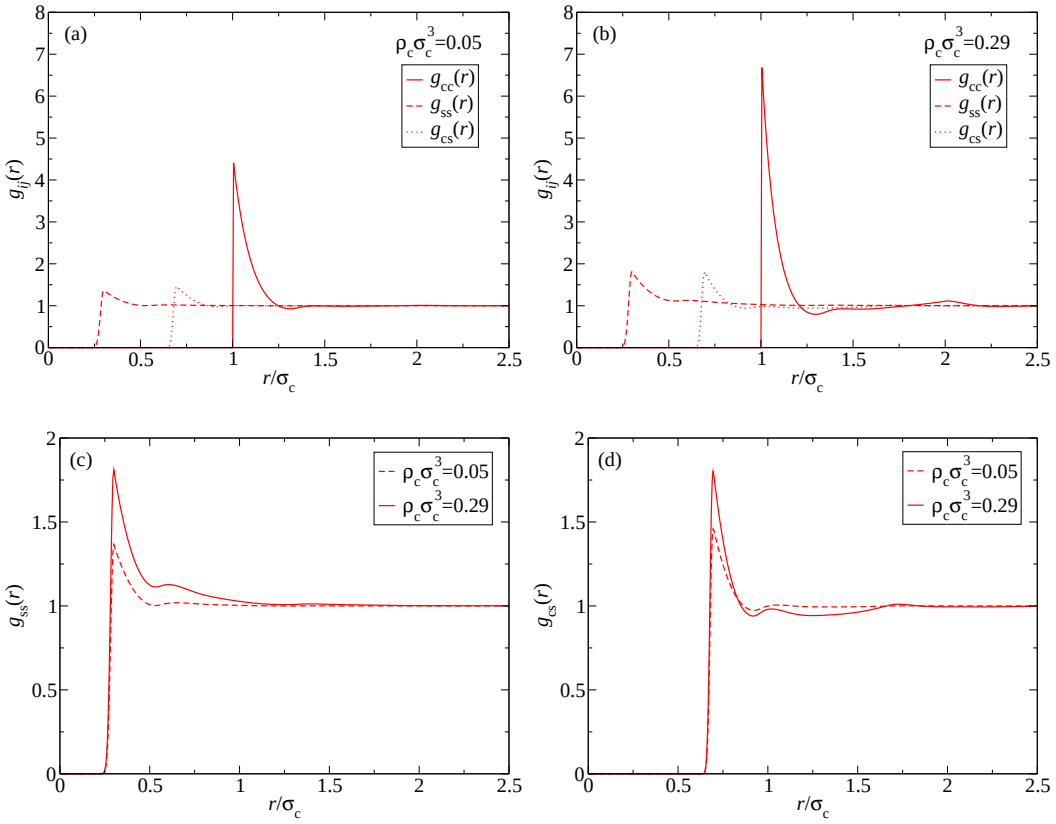

Figure 3.8: Partial radial distribution functions $g_{ij}(r)$ $(i = \mathrm{c}, \mathrm{s})$ for PE-stars with $f = 30$ arms, star–colloid size ratio $q = 0.3$, fixed PE-star density $\rho_\mathrm{s}\sigma_\mathrm{s}^3 = 0.27$, and colloidal densities of (a) $\rho_\mathrm{c}\sigma_\mathrm{c}^3 = 0.05$ or (b) $\rho_\mathrm{c}\sigma_\mathrm{c}^3 = 0.29$. For the same value of the stars' partial density, the remaining two parts of the figure illustrate the detailed shape and the ρ_c-dependence of (c) the star–star correlation function $g_\mathrm{ss}(r)$ and (d) the cross-correlation function $g_\mathrm{cs}(r)$. For an in-depth discussion and interpretation of the results, we refer the reader to the main text.

tact value $g_{cc}(\sigma_c)$ and its further rise upon increasing the PE-star density (not shown in our figures) is an obvious manifestation of the mainly attractive character of the effective colloid–colloid interactions. In this respect, we again refer the reader to Sec. 3.4.1 and, in particular, Eq. (3.32) mathematically describing the inversion procedure for the OZ relation. On the other hand, when taking a closer look to the whole set of pair correlation functions we find various signs pointing towards the supposable occurrence of a demixing transition. The main peaks of both $g_{ss}(r)$ and $g_{cc}(r)$ gain in height when adding colloids to the system, while the peak height of the cross-correlation function $g_{cs}(r)$ remains essentially the same [see Figs. 3.8(a), (b) and (d)]. In addition, Figs. 3.8(c) and (d) show an enhancement in the star–star pair correlations and an concurrent depletion in the colloid–star correlations for raising colloid densities. The intervals of distances affected are remarkably broad, both the range of the enhancement and the depletion are of the order of the colloid size, not the much smaller star size. Altogether, these features show the tendency of colloids as well as stars to seek spatial proximity of their own species while avoiding the other one, and we may expect macroscopic regions rich in the one and poor in the other species to be formed provided the partial densities, in particular of the colloids, are sufficiently high.

Fig. 3.9 illustrates the typical shape of the partial structure factors $S_{ij}(k)$. Here, we chose the parameters as follows: the PE-star functionality is $f = 18$, we set the size ratio to $q = 0.2$, fixed the density of the stars as $\rho_s\sigma_s^3 = 0.12$, and considered several values of the colloidal density $\rho_c\sigma_c^3$. When comparing the three main plots of the figure, the first finding is that the locations of the different Lifshitz lines [157,158] in density space strongly vary. These lines mark the crossover of respective structure factors between a regime where they display a local minimum in the long wavelength limit $k \to 0$ and a region where the behavior changes to developing a local maximum for the same k-values. While for the given number of stars in the system the star–star Lifshitz line is obviously immediately crossed for practically arbitrary low colloid concentrations [Fig. 3.9(b)], we need an noticeably increased partial colloid density lying in the range of about $0.25 \lesssim \rho_c\sigma_c^3 \lesssim 0.5$ for the colloid–star structure factor to experience such crossover [Fig. 3.9(c)]. In case of the colloid–colloid structure factor, the corresponding values of the colloid density are even higher, about $\rho_c\sigma_c^3 \approx 0.7$ for the parameters used here [Fig. 3.9(a)]. Another indication of the demixing transition we are searching for within the scope of this chapter and that is expected to occur upon adding more and more colloids and stars to the binary mixture is the tendency of all partial structure factors to diverge in the aforementioned long wavelength limit, i.e., $S_{cc}(k \to 0) \to +\infty$, $S_{ss}(k \to 0) \to +\infty$ and $S_{cs}(k \to 0) \to -\infty$, thus demonstrating that we approach the spinodal line. The inset in Fig. 3.9(b) was included in order to again demonstrate the huge difference in the structural length scales of the two species present in the mixture. The pre-peak in the cross structure factor $S_{cs}(k)$ is without any direct physical interpretation, while pre-peaks in the

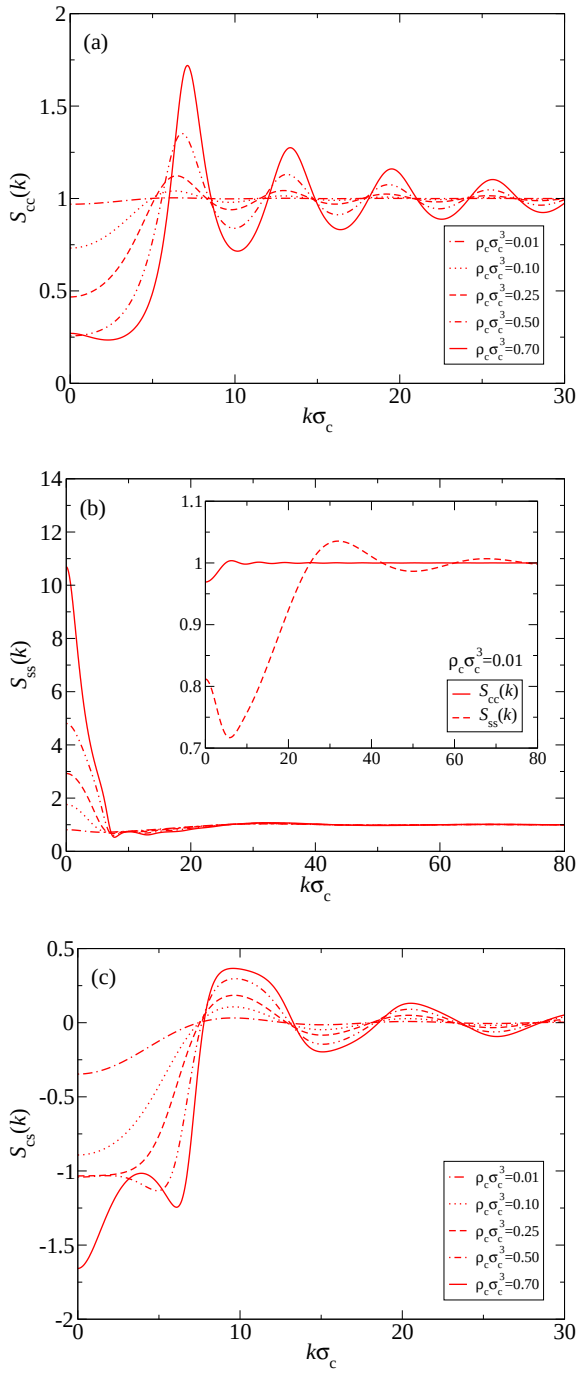

Figure 3.9: Examples of the partial structure factors (a) $S_{cc}(k)$, (b) $S_{ss}(k)$, and (c) $S_{cs}(k)$ for PE-star functionality $f = 18$, size ratio $q = 0.2$, fixed density of the stars $\rho_s\sigma_s^3 = 0.12$, and several values of the colloidal density $\rho_c\sigma_c^3$, i.e., different mixture compositions. Please note that the line styles in the main plot of part (b) refer to the same parameters as explained in the legends of parts (a) and (c), respectively. The inset in (b) addresses a comparison between the colloid–colloid and the star–star structure factors for the aforementioned star density and a typical value of the colloid density (indicated in the plot) and thereby illustrates the huge difference in the structural length scales of the two species.

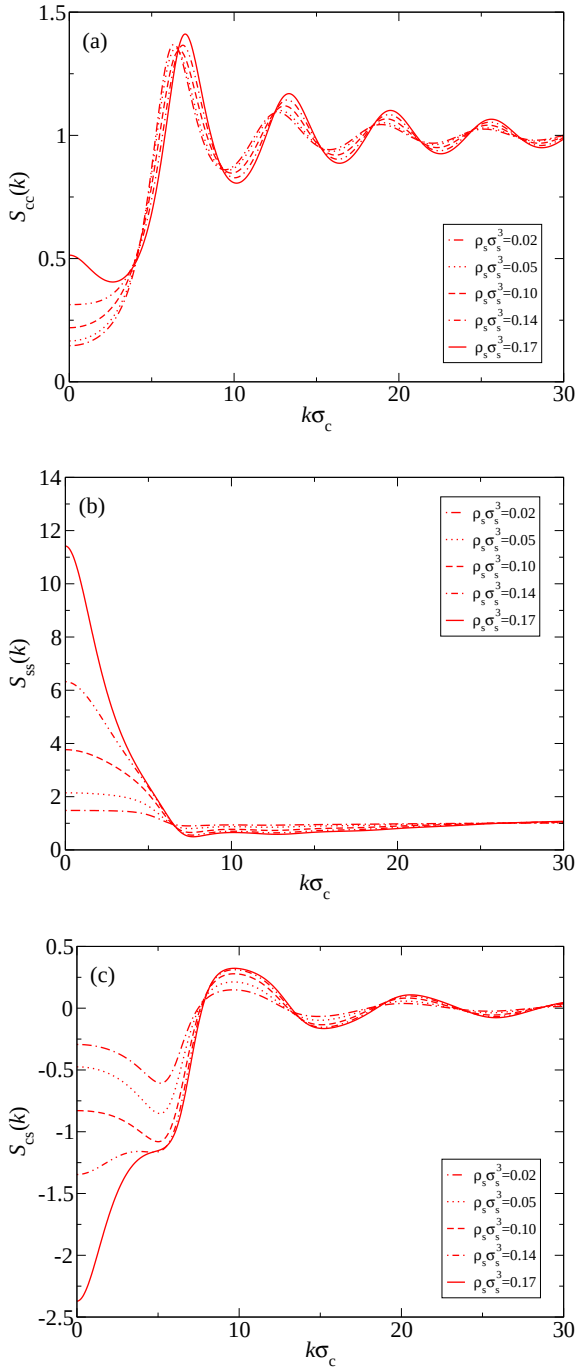

Figure 3.10: The same as Fig. 3.9, but now for fixed colloid density $\rho_c\sigma_c^3 = 0.5$ and several values of the PE-star density $\rho_s\sigma_s^3$.

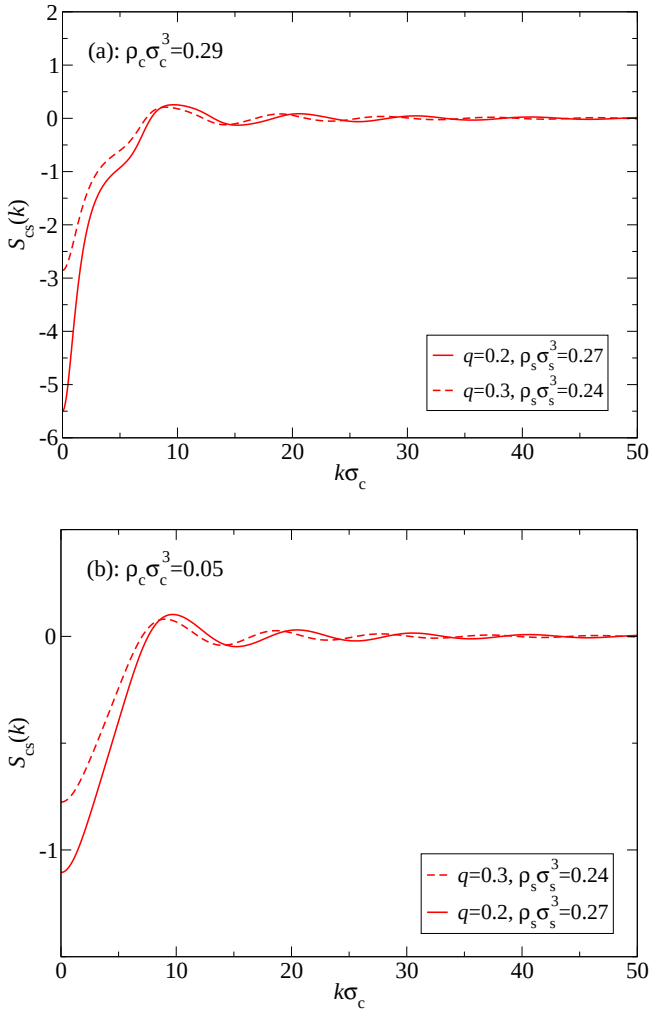

Figure 3.11: Comparison of the cross structure factors $S_{\rm cs}(k)$ for $f = 30$ and the two different size ratios investigated, $q = 0.2$ and 0.3. The PE-star partial densities were chosen to be almost the same in both cases, i.e., $\rho_{\rm s}\sigma_{\rm s}^3 = 0.27$ and 0.24, respectively. The corresponding colloid densities are (a) $\rho_{\rm c}\sigma_{\rm c}^3 = 0.29$ and (b) $\rho_{\rm c}\sigma_{\rm c}^3 = 0.05$. Upon varying the size ratio, the peak positions shift and the $(k = 0)$-values of the partial structure factors shown change significantly while there is no remarkable effect on the height of the different peaks.

intra-species structure factors would evince micro-phase separation [149–153]. Since the latter peaks are completely absent in our case, we may once more conclude that the system is expected to macro-phase separate instead of forming clusters. Fig. 3.10 also shows results for the partial structure factors $S_{ij}(k)$, but in contrast to Fig. 3.9 now for fixed colloid density $\rho_c\sigma_c^3 = 0.5$ and varying values of the PE-star density $\rho_s\sigma_s^3$. As expected, the observed trends are clearly the same.

Finally, Fig. 3.11 depicts the q-dependence of the cross structure factors for $f = 30$ and two different values of the colloid density $\rho_c\sigma_c^3$ [parts (a) and (b)]. For both size ratios investigated, the star densities $\rho_s\sigma_s^3$ are chosen to be almost the same[5]. As is obvious from the plots, a change in q only affects the peak positions and the depth of the local minimum for $k \to 0$, but there is no significant influence on the peak heights of the functions. This is in agreement with the findings for the q-dependence of the effective colloid–colloid interactions (see Fig. 3.7), and essentially means that the size ratio q is crucial for determining the typical structural length scales, but hardly for how pronounced this structure is.

3.4.3 Fluid–fluid phase equilibria

After having found plenty of evidence in our analysis so far for a mixing–demixing transition taking place for certain ranges of partial densities $\rho_i\sigma_i^3$, we finally come to a more quantitative description based on the corresponding binodals obtained as explained above. In Fig. 3.12 we show the demixing binodals for size ratios $q = 0.2$ [Fig. 3.12(a)] and $q = 0.3$ [Fig. 3.12(b)] and for different PE-star functionalities f, as denoted in the legend boxes. In addition, we connected some of the point pairs used to compute the binodals and representing coexisting colloid-rich and colloid-poor phases by tie lines. Concerning the mutual positions of the binodals in the density plane, it can be seen that they shift towards higher PE-star concentrations upon increasing the size ratio q and/or decreasing the PE-star functionality f. This characteristic behavior is in agreement with previous studies of binary mixtures of colloids and neutral polymer stars [137]. The filled triangles in Fig. 3.12 denote rough estimates for the positions of the respective critical points determined graphically by taking the tie lines into account. The critical points move towards slightly lower colloid densities when lowering the arm number of the PE-stars, whereas altering the size ratio has q has no significant effect.

The star densities $\rho_s\sigma_s^3$ that bring about a demixing instability are typically higher for the case $q = 0.3$ than for the case $q = 0.2$. This looks counterintuitive at first sight, since one expects that larger PE-stars will destabilize the mixture earlier.

[5] They are not exactly the same since such results are not systematically available due to the fact that we originally solved the OZ relation together with the RY closure for points in the density plane where the star density takes 'smooth' values when scaled with respect to the colloidal diameter σ_c, not their own diameter σ_s.

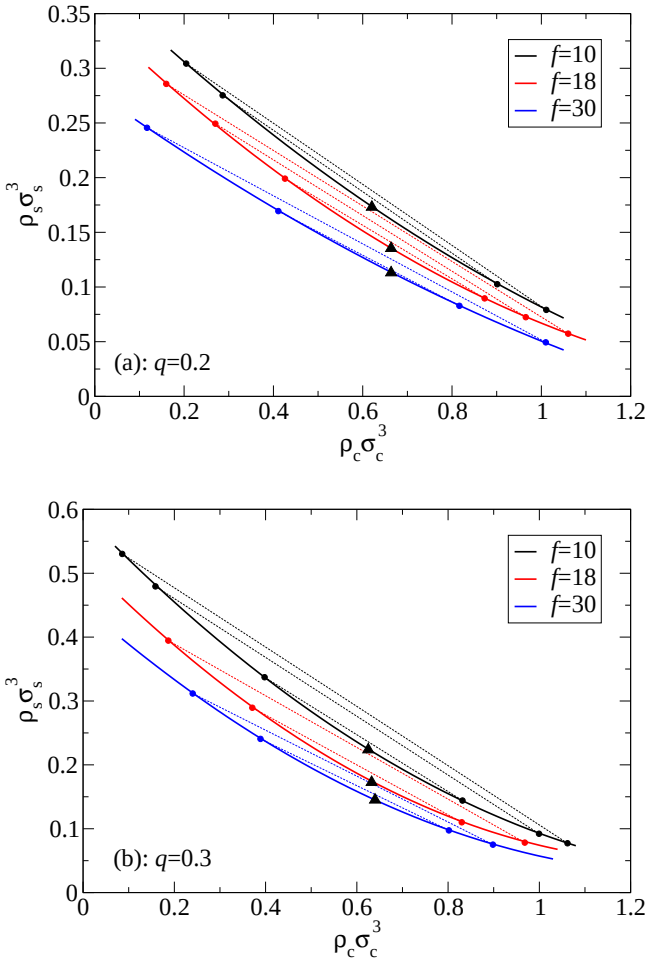

Figure 3.12: Demixing binodals calculated according to the procedures introduced in the main text for (a) $q = 0.2$ and (b) $q = 0.3$, and different values of the PE-stars' functionality f. In order to illustrate the coexisting colloid-poor and colloid-rich phases, we additionally show several tie lines. In this connection, please note that we in fact used much more such point pairs in order to obtain the binodal lines and not only the shown ones. Based on the full sets of coexisting fluid phases we computed, we made rough estimates for the positions of the respective critical points in the ρ_c-ρ_s plane, represented by the filled triangles.

In order to put the numbers in their appropriate context, it is useful to employ the picture of the effective colloid–colloid potential, which includes a star-induced attraction. Here, the range and depth of this attraction steer the occurrence of the demixing binodal, which is equivalent to a separation between a colloidal fluid and a colloidal gas. The natural length scale in this picture is the colloid diameter σ_c; concomitantly, the physically relevant density in making comparisons between the $q = 0.2$ and the $q = 0.3$ cases should be scaled with the colloid size: $\rho_s\sigma_c^3 = q^{-3}\rho_s\sigma_s^3$. It can be easily seen that the additional pre-factor q^{-3} renders the rescaled star densities for $q = 0.3$ indeed lower than the ones for $q = 0.2$, in agreement with the intuitive expectations.

The volume terms for the integrated out counterions [159–161] do not affect the phase boundaries, since under the assumption of full absorbing in the stars' interiors, they are simply proportional to the number N_s of the latter [36] and thus they cause a trivial shift of the stars' chemical potential, without affecting the osmotic pressure of the solution [4]. Finally, we mention that we did not consider the competition between the demixing binodals and the crystallization of the colloids. The investigation of the system's solid states lies beyond the scope of this work. The trends found for the f- and q-dependences are comparable to the colloid–star polymer case mentioned above. Although the underlying pair potentials are different to a certain degree, a closer inspection to the full phase diagrams in Ref. [137] can give hints regarding the stability of the binodals against pre-emption by the freezing lines. Provided the positions of the freezing lines are not too different here, it seems to be reasonable to assume, based on such a comparison, that our demixing lines will survive at least for the larger size ratio between stars and colloids. Nevertheless, the existence of a demixing binodal, even in the case that the latter is pre-empted by crystallization, has important consequences for the time scales involved in the dynamics of crystallization [162, 163].

3.5 Conclusions

We have put forward a coarse-grained description of mixtures between neutral, spherical, hard colloids and multi-arm PE-stars of size smaller than the colloidal particles. Effective interactions between the constituent particles have been employed throughout, allowing for a mesoscopic description that leads to valuable information on the structure and thermodynamics of the two-component mixture. The cross-interaction, which has been derived here, is sufficiently repulsive to bring about regions of instability in the phase diagram and leading thereby to macroscopic, demixing phase behavior. This, in turn, can be rationalized by means of the depletion potentials between the colloids, which are induced by the stars, and feature attractive tails akin to those encountered in usual colloid–polymer mixtures.

The form of the cross-interaction plays a crucial role in determining stability and can, by suitable tuning, completely change the behavior of the mixture from macroscopic phase separation to micro-phase structuring with a finite wavelength. In this respect, a very promising direction of investigation is to allow for the colloids to carry a charge opposite to that of the arms of the PE-stars. As we are going to see in chapter 4, there is a rich variety of resulting complexation morphologies between the two constituents.

Chapter 4

Complexation of polyelectrolyte stars with charged substrates

Within this chapter, we study the complex formation of star-branched polyelectrolytes (PE's) with oppositely charged substrates of different geometries by means of monomer-resolved molecular dynamics (MD) simulations. In case of planar surfaces, we identify five different morphological states with continuous crossovers between them, ranging from almost undisturbed, spherical configurations for low surface charge densities to fully collapsed, two-dimensional starfish-type arrangements in the complementary limit of strong electrostatic attractions. Thereby, the PE-stars lose the ability to reabsorb the vast majority of their counterions. The general behavior is stable against variation of the PE-star density and addition of accessory wall counterions, although there are quantitative changes. For weakly curved surfaces, i.e., PE-stars near charged colloids of larger radius, our results prove the fundamental trends to persist as long as the size ratio is sufficiently small.

4.1 Introduction

In chapters 2 and 3, we studied the impact of planar and curved confinement on the typical conformations and other properties of star-branched PE's. Thereby, we determined the purely repulsive, effective interaction between PE-stars and neutral, flat walls by dint of both simulational techniques and mean-field theory [126, 127]. Based on the results, the cross-interaction between PE-stars and hard, uncharged colloids of larger diameter was calculated, granting access to a computation of the structural and phase behavior of binary colloid–PE-star mixtures [164]. A consequential next step is to drastically change the features of the confining surfaces by allowing for them to carry charges of opposite sign with respect to the PE-stars, thus inducing a complexation process of morphological nature.

In the recent past, a great deal of work was already devoted to investigations of the adsorption of linear PE's to planar, charged substrates, charged colloids or cylinders, proteins, and dendrimers. All these efforts were motivated by the high biological and technical relevance of such processes. Hereby, theoretical [1, 58–68], experimental [69–77] and simulational methods [78–90], were employed to study a rich variety of problems. This includes, e.g., the complexation and coagulation characteristics, the dependence of the resulting configurations on size and charge ratios, a possible change of the complexation tendency upon variation of chain rigidity, overcharging phenomena, the functional form of effective interactions between the substrate and the attracted PE's, and the stability of the composed entities. Many-body effects like induced flocculation, PE multi-layering, and phase separation into colloid-poor and colloid-rich, complexated phases also attracted a lot of interest. However, there is no systematic comparison of theory and experiment yet that is devoted to the adsorption onto colloidal particles (for a discussion of this problem, see Ref. [165]).

For star-branched PE's, to our best knowledge only very little work probing the complex formation with charged substrates was done up to now [166, 167]. We are going to deal with PE-stars instead of linear PE's not only because this is a natural extension of our previous work, but also since this particular architecture offers a number of distinct advantages. As already stated in the previous chapters, by modifying the functionality, PE-stars show the unique property of being tunable, soft colloids and bridging between ultra-soft and stiff behavior. This character, together with the ability of PE-stars to absorb a large amount of counterions, renders the complexation process very different from that of linear PE chains. By suitably changing, e.g., the PE-star functionality or the surface charge density of the substrate, we can thus generate a large variety of complex morphologies. In the extreme limit of very strong PE-star–wall attractions, this complexation can be expected to reach as far as a full collapse onto two-dimensional configurations, which we are going to call 'starfishes' in what follows. Indeed, the existence of the latter already found experimental corroboration [166]. Moreover, it is known that the configurations of PE-stars can also be influenced by other stimuli. The addition of multivalent counterions can induce a collapse of PE-stars in solution or in the adsorbed state on mica surfaces, and they can subsequently be switched from the collapsed back to an expanded state by laser light [167]. In case of colloid–PE-star mixtures, new types of supra-colloidal aggregates might also be created, gaining insight and control over the phase behavior and the transport properties of such solutions.

From a technical and application-oriented point of view there is also a strong interest in undertaking efforts to understand how shape and structure of complexes built of PE-stars and planar or curved surfaces can be influenced externally. Since PE-stars show far-reaching fundamental similarities to ionic hydrogels, which were found to form arrays of dynamically tunable, photo-switchable or bioresponsive mi-

crolenses [91–94], theoretical predictions regarding possibilities to precisely steer these lenses would allow for the design and tailoring of single such functional units or even entire functional surface coatings and nano-devices.

The chapter at hand is organized as follows. In Sec. 4.2, we describe the physical systems under investigation and the necessary modifications to the simulation model as originally introduced in chapter 2. In Secs. 4.3 to 4.7, we present results for density profiles, the equilibrium center-to-surface separation, the effective forces acting between a PE-star and the substrate, and the surface charge dependence of the PE-star radii, in each case for planar charged walls. Moreover, we develop quantitative criteria to classify the observed complex morphologies and draw corresponding 'phase' diagrams illustrating the diffuse regions where continuous crossovers between different types of configurations take place. Sec. 4.8 is devoted to an analysis of the influence of wall curvature on the physical behavior. Finally, in Sec. 4.9, we summarize our findings and conclude.

4.2 Physical setup and simulation model

4.2.1 Planar charged substrates

In order to explore the complexation of PE-stars and charged, planar substrates, we go back to the geometry and the simulation model as described in Sec. 2.2, including all the basic simulational parameters and essentially using the same techniques. To give a brief summary, we consider a dilute, salt-free solution of PE-stars, each modeled to consist of f bead-spring chains of LJ particles with typical diameter d. These chains are grafted to a common colloidal core of finite radius R_d, and the resulting macromolecular entities are confined in a slit-pore of width τ. The total volume of the simulation box is denoted as $\Omega = M^2\tau$, and we set $M = \tau = 120d$, exactly as in the case of neutral confining walls. We only implicitly incorporate a good, aqueous solvent via its relative permittivity $\epsilon \approx 80$. As before, we suppose the dielectric constants of the solvent and the planar substrates (typical experimental values $2 \lesssim \epsilon_\mathrm{p} \lesssim 5$) to be the same, since a dielectric discontinuity would result in the appearance of additional image charges [90, 95]. Based on previous experience [102, 168] we expect, however, that image charges play a subdominant role in the phenomena, and for the sake of simplicity we again ignore them altogether.

In what follows, we are going to study two different setups, referred to throughout as systems I and II, respectively, and depicted in Fig. 4.1. In case of system I, symmetrically charging both confining walls, located at positions $z_\pm = \pm\tau/2$, by homogeneous surface charge densities $\pm\sigma_0/2$ with $\sigma_0 \geq 0$ yields a capacitor-like geometry. Due to construction, the overall system made up of the PE-stars, their associated counterions, and the surfaces charges is electroneutral. Assuming

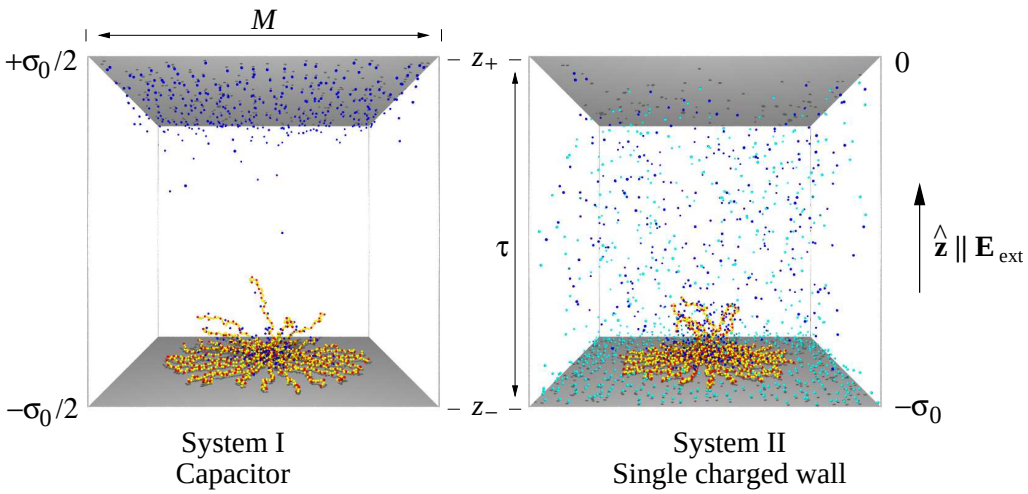

Figure 4.1: Sketch of the geometry for planar, charged substrates: PE-star in slab-like confinement, whereby an additional external electric field $\mathbf{E}_{\text{ext}}$ is applied by bringing surface charges onto the walls. We study two different physical setups, denoted as systems I (left) and II (right), respectively. As in Fig. 2.1, yellow balls are neutral monomers, while the red balls along the backbones of the chains indicate positively charged monomer ions and dark blue spheres depict counterions to the star. In case of system II, the light blue spheres are positively charged wall counterions.

infinitely large plates, i.e., for the case of an ideal parallel-plate capacitor, the resulting external electric field is constant, namely $\mathbf{E}_{\text{ext}} = -(2\pi\sigma_0/\epsilon)\hat{\mathbf{z}}$. Accordingly, each charged particle of valency Z_i, i.e., charge $Z_i e$ (with $e > 0$), is exposed to an external potential reading as

$$V_{\text{ext}}(z) = \frac{2\pi\sigma_0 Z_i e}{\epsilon} z. \tag{4.1}$$

Alternatively, in case of system II, for a given value of σ_0 we generate exactly the same electric field and corresponding potential by bringing a surface charge density $-\sigma_0$ onto the lower wall, only. In contrast to system I, we then need to introduce $N_+ = M^2\sigma_0/e$ positively charged wall counterions, i.e., coions with respect to the PE-star, to compensate for the unbalanced surface charge densities of the two plates. Thereby, akin to the star counterions, the wall counterions are modeled as LJ beads of the same diameter d and mass m as the monomers, carrying a monovalent charge $+e$. Clearly, comparing results as obtained for both setups renders possible a systematic analysis of the wall counterions' influence on the complexation process and the resulting PE-star morphologies.

For both setups, we carry out simulations for PE-stars with fixed degree of polymerization $N = 50$, fixed charging fraction $\alpha = 1/3$, and a variety of different functionalities f ($f = 10, 18, 30, 50$), equivalent to a tuning of their behavior between ultra-soft and stiff. By restricting our studies to the case of fairly highly charged PE's, we expect a pronounced tendency to form stable complexes even for rather small strengths of the external electric field. We strongly vary the latter, considering values of the surface charge density σ_0 spanning two orders of magnitude, namely $\sigma_0 d^2/e = 0.005, 0.01, 0.03, 0.05$ and 0.1. In case of water as solvent and assuming constant room temperature, the Bjerrum length is $\lambda_B = 7.1$ Å [cf. chapter 2, Eq. (2.6)]. Thus, setting the Bjerrum length in our simulations to a value $\lambda_B = 3d$ accords to an experimental particle diameter $d = 2.4$ Å [101], and with $e = 1.602 \times 10^{-19}$ C being the absolute value of the elementary charge, we can translate the above charge densities from reduced to SI units[1]. The maximum charge density used is thus about $\sigma_0 \approx 0.28$ C/m^2, corresponding to one elementary charge per 60 Å^2, a realistic value under experimental conditions [169].

In general, we expect the scanned region in (f, σ_0)-space to feature a rich variety of PE-star morphologies. As already mentioned above, these might range from weakly disturbed, more or less spherical conformations for small strength of the external field and large functionalities to a fully collapsed starfish-limit for highly charged surfaces and small arm numbers. Thereby, it is *a priori* unknown what intermediate states might exist and how they may look like. Moreover, central questions are which criteria are appropriate to quantitatively distinguish the possible states, how sharp the necessarily continuous morphological crossovers between them are, and how precisely one can steer the adopted conformations by changing the decisive parameters. Besides gathering information on the fundamental shapes of the stars, it is also of great interest how several other properties are affected and may change compared to their respective counterparts for free PE-stars or PE-stars in neutral confinement. Particularly, this includes the relative center-to-end radii $R_s(\sigma_0)/R_s$, with $R_s \equiv R_s(\sigma_0 = 0)$, and the ability of the PE-stars to absorb the majority of their counterions. In addition, we also monitor the equilibrium center-to-surface separation, the effective interaction between the charged substrate and the PE-stars, and density profiles of all the particle species present in the system, in either case as a function of both f and σ_0. In doing so, we hope to gain deeper insight into the competition between entropic and electrostatic contributions to the total free energy.

In order to guarantee that we reach true equilibrium configurations for the PE-stars instead of metastable states corresponding to local minima of the free energy

[1] Although we use the Gaussian cgs system of units throughout this thesis, the SI system is most convenient to compare our data to experimental values. In Gaussian units, the absolute value of the elementary electron charge is $e = 4.803 \times 10^{-10}$ g$^{1/2}$ cm$^{3/2}$ s^{-1}, and translating the maximum surface charge density considered here consequently yields $\sigma_0 = 0.83 \times 10^5$ g$^{1/2}$ cm$^{-1/2}$ s^{-1}.

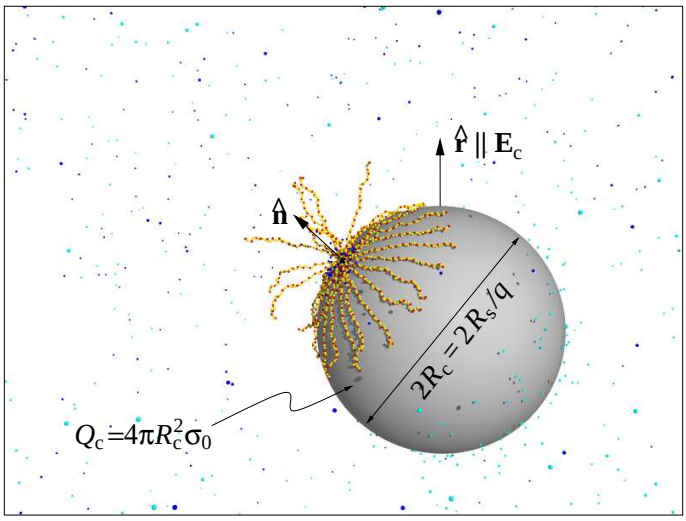

Figure 4.2: Sketch of the geometry for a curved, charged surface: a large colloid of radius $R_c > R_s$ (gray sphere), i.e., size ratio $q < 1$, carries a negative total charge Q_c, leading to a radial electric field $\mathbf{E}_c$. For a description of the color coding of the particle species, see also the caption of Fig. 4.1. The unit vector $\hat{\mathbf{n}}$ marks the instantaneous direction of the axis connecting the centers of colloid and PE-star.

and to explicitly check for hysteresis effects, we started simulation runs from both (hemi-)spherical and starfish-like initial configurations. Furthermore, we performed very long simulation runs, lasting about 2×10^6 time steps for equilibration and up to 6×10^6 time steps to gather statistics. Thereby, as in chapter 2, the typical time step was $\Delta t = 0.002 t_0$, with $t_0 = \sqrt{md^2/\varepsilon_{LJ}}$. It arises that there are only extremely weak hysteresis effects, to be discussed in the following sections.

4.2.2 Curved charged substrates: charged colloids

To take into account the influence of wall curvature, we need to modify the simulation model. We do not consider a confined system anymore, but switch over to a fully three-dimensional system, incorporated in our MD simulations via periodic boundary conditions for all spatial directions. Besides a cationic f-arm PE-star with its N_- monovalent counterions of charge $-e$ as described in Secs. 2.2 and 4.2.1, respectively, the cubic simulation box of total volume $\Omega = M^3$ now also contains a larger spherical colloid of radius R_c. Fig. 4.2 sketches the geometry and gives an impression of the physical situation. As in chapter 3 of this thesis, we accordingly define the size ratio between the PE-star and the colloid as the fraction

$$q = \frac{R_s}{R_c} = \frac{\sigma_s}{\sigma_c}. \tag{4.2}$$

The colloid is modeled akin to the core particle of the PE-star, i.e., we provide for its finite radius by using a shifted version of the LJ-type excluded volume repulsion for the colloid–monomer interaction:

$$V_{\mathrm{LJ}}^{\mathrm{c}}(r;R_{\mathrm{c}}) = \begin{cases} \infty, & r \leq R_{\mathrm{c}} \\ V_{\mathrm{LJ}}(r-R_{\mathrm{c}}), & r > R_{\mathrm{c}}. \end{cases} \tag{4.3}$$

Since we want to study electrostatically driven complexation, the colloid is assumed to carry a negative total charge $Q_{\mathrm{c}} = -Z_{\mathrm{c}}e$, compensated for by $N_+ = Z_{\mathrm{c}}$ positively charged, monovalent counterions. We presume the charge distribution to be spherically symmetric, therefore the colloid behaves from the electrostatic viewpoint like a point particle with the entire charge Q_{c} concentrated in its center and the resulting electric field reads as $\mathbf{E}_{\mathrm{c}}(r) = (Q_{\mathrm{c}}/r)\,\hat{\mathbf{r}}$. Consequentially, the Coulomb interaction between the colloid and any charged bead i of valency $Z_i = \pm 1$, with r denoting their mutual distance, is described according to Eq. (2.5):

$$\beta V_{\mathrm{Coul}}(r) = \lambda_{\mathrm{B}} \frac{Z_{\mathrm{c}} Z_i}{r}. \tag{4.4}$$

To evaluate the resulting forces, we again make use of Lekner's summation technique, but now in its version for three-dimensional geometries [103].

In contrast to the case of planar charged substrates, the systematic investigation of colloid–PE-star complex formation has just been initiated in the framework of this thesis and is subject of ongoing work. Thus, we present exemplary results only, namely for stars with constant degree of polymerization $N = 50$, fixed charging fraction $\alpha = 1/3$, and functionalities $f = 10, 18$ and 30. For all values of f, the colloid–star size ratio is chosen to be $q = 0.5$ with the star radii as given in Table 2.1, i.e., the star is smaller than the colloid. In either case, the colloidal charge is set to be $Q_{\mathrm{c}}/e = -700$. Assuming all the charges of the colloid to be placed on the surface, we may define a surface charge density analogous to Sec. 4.2.1:

$$\sigma_0 = -\frac{Q_{\mathrm{c}}}{4\pi R_{\mathrm{s}}^2} q. \tag{4.5}$$

Then we have $\sigma_0 d^2/e \approx 0.02$, or, equivalently expressed in SI units[2], $\sigma_0 \approx 0.06\ \mathrm{C/m^2}$, with the exact value depending on the functionality f.

Due to the huge radius of the colloid, we need to increase the edge length of the simulation box to $M = 384d$. Since the colloid is supposed to act as a curved substrate and its spatial position is thus fixed during the simulation runs, there is no necessity to change the typical time step compared to the previous subsection or chapter 2: $\Delta t = 0.002 t_0$, with $t_0 = \sqrt{m d^2/\varepsilon_{\mathrm{LJ}}}$. The equilibration time is chosen to be $t_{\mathrm{eq}} = 1 \times 10^6 \Delta t$, and afterwards we average all the quantities of interest over about 4×10^6 time steps to guarantee good statistics.

[2] As in Sec. 4.2.1 and for sake of completeness, we also specify the value of the surface charge density σ_0 in Gaussian units: $\sigma_0 \approx 0.17 \times 10^5\ \mathrm{g^{1/2}\,cm^{-1/2}\,s^{-1}}$.

4.3 Density profiles

To begin with, we will focus on the two planar geometries, systems I and II, in Secs. 4.3 to 4.7. In general, a convenient means in analyzing the conformational properties of PE-stars near charged, flat walls is to measure one-particle density profiles for all particle species. Let $\rho_\alpha(\mathbf{r})$ ($\alpha = \mathrm{m}, \mathrm{mi}, +, -$) denote the local number densities of monomers, monomer ions, and positively and negatively charged free ions, respectively, at a position $\mathbf{r}$ between the confining plates. Due to geometry and the resulting external electric field, $\hat{\mathbf{z}}$ marks a preferred direction in the system. For this reason, the spatial arrangement of the PE-stars can be expected to exhibit a cylindrical symmetry around an axis parallel to $\hat{\mathbf{z}}$ and running through the star center. The lateral structure is of less significance and we consider the density in a coarse-grained fashion with the x- and y-dependencies integrated out:

$$c_\alpha(z) = \int_{-\infty}^{\infty}\int_{-\infty}^{\infty} \mathrm{d}x\,\mathrm{d}y\;\rho_\alpha(\mathbf{r}). \tag{4.6}$$

Due to the electrostatic attraction, for both setups I and II the PE-star is expected to form a complex with the lower plate. Therefore, it is useful to express the density distributions as a function of the distance $D = |z_- - z| = z - z_-$ from the latter,

$$c^*_\alpha(D) = c_\alpha(D + z_-). \tag{4.7}$$

In our simulations, we can easily obtain $c_\alpha(z)$ or $c^*_\alpha(D)$, respectively, via partitioning the system in thin rectangular slabs of width Δz parallel to the (x, y)-plane, counting the number of particles of species α in each slab, averaging the same during the simulation runs, and subsequently normalizing the profile by dividing by Δz and the respective total particle number N_α.

Fig. 4.3 shows typical results for the monomer density $c^*_\mathrm{m}(z)$ of ($f = 30$)-arm PE-stars as received for (a) system I and (b) system II. As one would anticipate, the monomer density features a pronounced global maximum as σ_0 increases, i.e., its height grows and the peak becomes more narrow. In addition, the peak position D_0 noticeably moves towards the wall. While D_0 is of the order of the star radius R_s for weak external fields, we reach the closest possible approach $D_0 \approx d$, as determined by the typical bead size, for $\sigma_0 d^2/e = 0.1$. This behavior obviously reflects the PE-star–wall complexation process.

The insets in both panels of Fig. 4.3 display the same profiles but have rescaled axes in order to shed light on the structure beyond the dominating main peaks, in particular for the high-σ_0 regime. As can be seen, the profiles $c^*_\mathrm{m}(D)$ basically consist of only one broad peak for small values of σ_0, mirror-symmetrical with respect to the position of the maximum, at least for system I. This shape corresponds to still almost spherical PE-stars. Upon ramping up the external field, a secondary

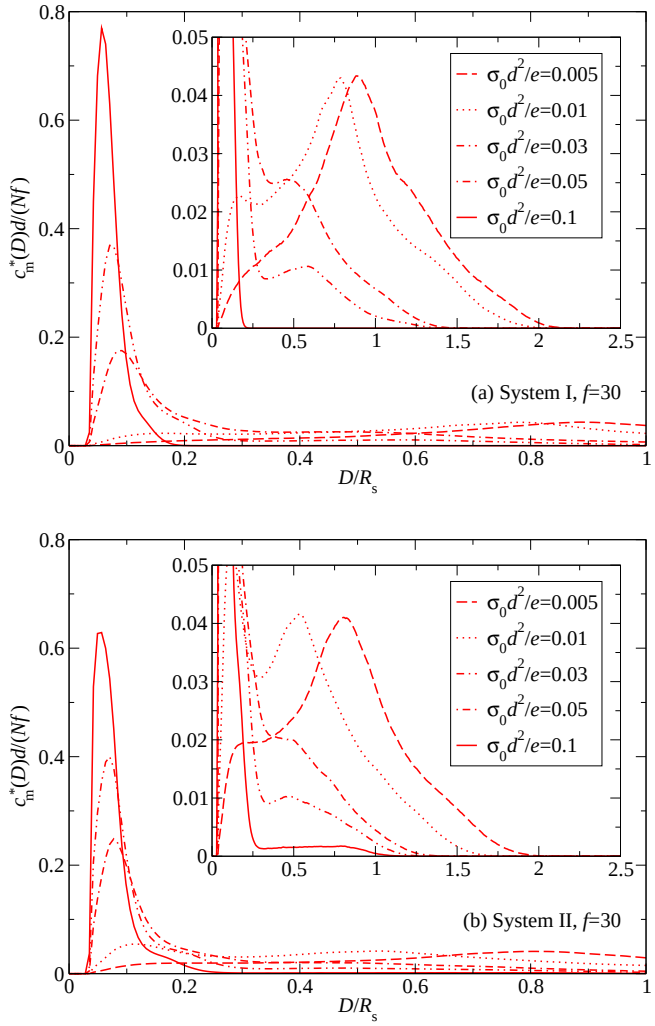

Figure 4.3: Monomer density profiles $c_{\mathrm{m}}^*(D)$ as a function of the distance D with respect to the lower wall, both for (a) system I and (b) system II. We show data as obtained for $f = 30$ and different values of the surface charge density σ_0. The insets have rescaled axes in order to illustrate the structure of the density distributions beyond their dominating global maxima.

peak of rising height develops close to the surface and at the same time the first peak shrinks, expressing the progressing distortion of the PE-star. At a certain point, depending on the setup, the second peak exceeds the first one in height, thus becoming the new global maximum of the density distribution. This trend continues with a further increase of the external field's strength. Thereby, the right peak degenerates completely and the resulting tail may even vanish for the highest surfaces charge densities investigated here (solid lines in the plots). Then, we have reached a fully collapsed, starfish-like conformational limit, were all the monomers are located within a small region close to the confining wall, at the utmost only about three monomer diameters away from the latter.

A comparison between the results for the two setups shows that there are the same typical shapes occurring, but the dependence on σ_0 differs. In case of system II, the presence of additional positive ions seems to support configurational changes for small surface charge densities σ_0, leading to an earlier onset of deviations from sphericity. For instance, for $\sigma_0 d^2/e = 0.01$, the left peak already exceeds the right one, while it is hardly developed for the capacitor-type geometry I. By contrast, in the high-σ_0 regime, the wall counterions obviously obstruct conformational changes. We observe a small persisting tail of the monomer distribution, i.e., the star is prevented from reaching the starfish limit.

The intriguing role of the wall counterions can be understood by considering the competition between entropy and electrostatics and the tendency of the system to achieve local charge neutrality. In general, there is always a gain in entropy if positively charged, bound monomer ions are adsorbed to the substrate instead of the unbound wall counterions, thus releasing the latter. Such entropic contributions add to the purely electrostatic PE-star–wall attraction and effectively strengthen it, noticeable in particular for weak electric fields and, accordingly, PE-stars loosely attached to the wall. But for higher values of σ_0, electrostatic interactions become dominant in the system. The monomer ions alone cannot compensate for the surface charges anymore and a considerable fraction of wall counterions is adsorbed anyway, thus screening the wall charges. Thereby, the effective attraction between PE-star and substrate is diminished, and in this sense the positively charged ions now inhibit complexation.

The argumentation of the preceding paragraph is corroborated by the measured distributions $c_+^*(D)$ for the wall counterions as exemplarily shown in Fig. 4.4, again for $f = 30$ and the whole range of surface charge densities σ_0. As expected, the profiles for $\sigma_0 d^2/e \lesssim 0.01$ feature very diffuse and flat maxima for small D, revealing the release of ions from the lower wall due to an entropy gain resulting from their replacement by the PE-star. Upon an increase of σ_0, a sharply bordered layer of adsorbed ions forms, as identifiable by the emerging peak. Accordingly, the described screening of the external field sets in, weakening the tendency of the PE-stars to form tightly bound complexes with the confining wall.

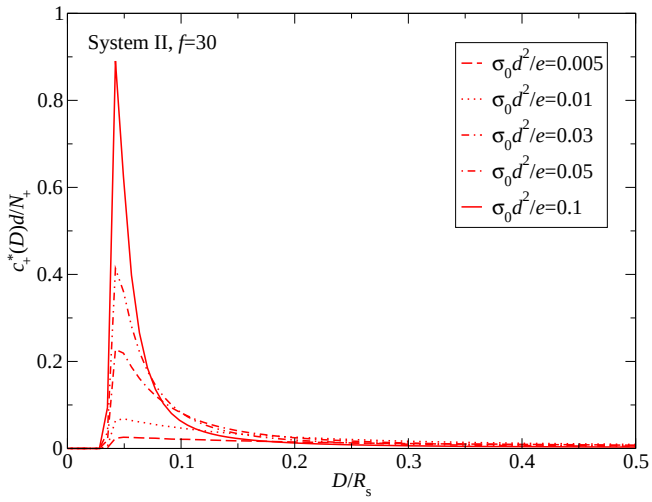

Figure 4.4: Wall counterion density profile $c_+^*(D)$ for system II as a function of the distance D with respect to the lower wall. As in Fig. 4.3, the results pertain to a PE-star with $f = 30$ arms and the whole range of surface charge densities σ_0.

Fig. 4.5(a) and (b) show counterion profiles $c_-^*(D)$ for systems I and II, respectively. The parameters are again the same as above. Since the monomer ions are distributed regularly along the backbones of the PE-chains and their density profiles must hence have the same functional form as shown in Fig. 4.3, one would expect the counterion density to follow the monomer profiles due to Coulombic attractions. Indeed, for both systems the results exemplify that this is true only in case of walls carrying small amounts of surface charges. As soon as σ_0 reaches intermediate values, the behavior changes drastically. The number of trapped ions is reduced considerably with increasing σ_0, apparent from the shrinkage of the corresponding peak in the density profile. In the limit of very high surface charge densities, the vast majority of counterions is repelled from the interior of the star. This is in strong contrast to the case of free PE-stars [32, 33] or PE-stars in neutral confinement [126, 127] (cf. also chapter 2), where always only small fractions of ions are released from captivity.

The origin of this phenomenon can be understood as follows. Since the lower wall carries surface charges of opposite sign with respect to the monomer ions, it contributes significantly in establishing local electroneutrality. Thus, less star counterions are needed for this purpose. In addition, a release of ions from a trapped state is also entropically beneficial, as already discussed above in connection with the positively charged wall counterions. Furthermore, negatively charged star counterions are simply repelled electrostatically by the wall. For completely flat starfish-type configurations, all monomer ions are located close to the substrate and, provided the

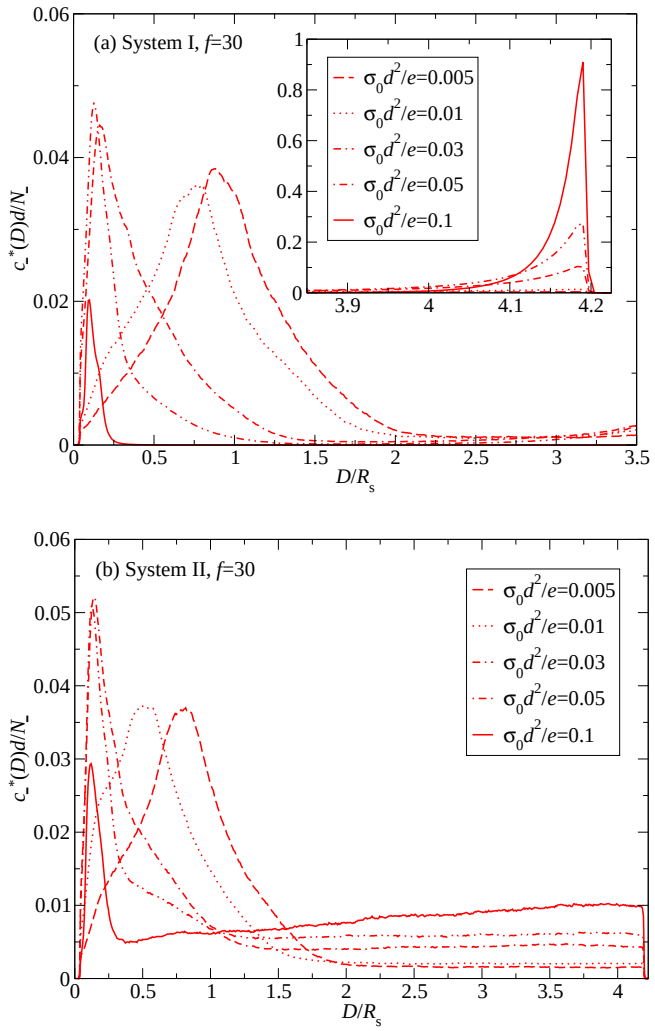

Figure 4.5: Star counterion density profiles $c^*_-(D)$ as a function of the distance D with respect to the lower wall for (a) system I and (b) system II. The other parameters are the same as in Figs. 4.3 and 4.4. The inset in part (a) was included to point out the articulate peak developing close to the upper wall.

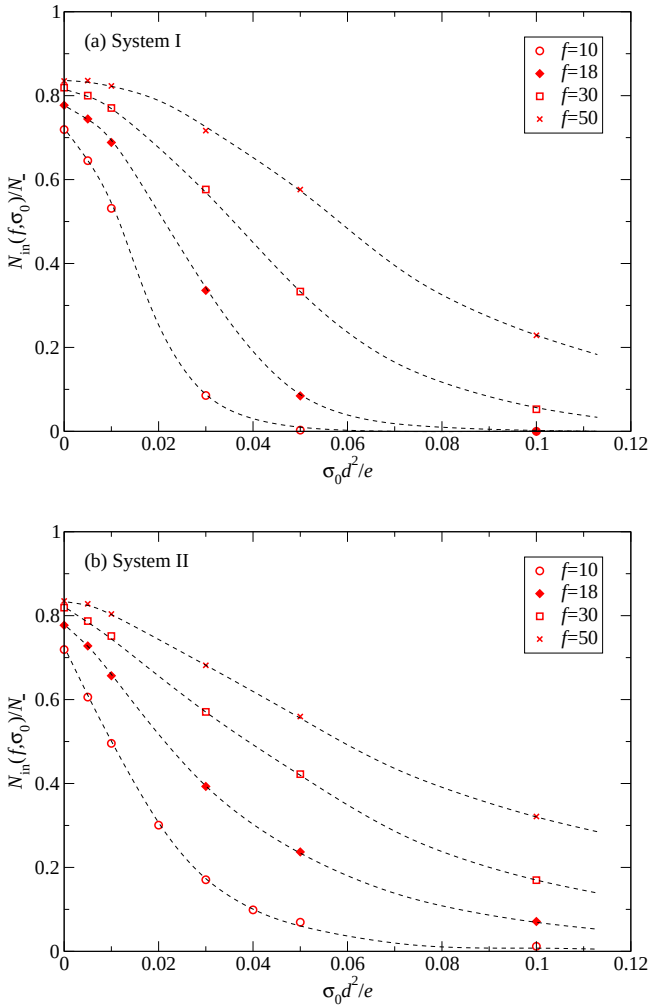

Figure 4.6: Fraction $N_{\text{in}}(f, \sigma_0)/N_-$ of trapped star counterions as a function of the surface charge density σ_0 for (a) setup I and (b) setup II. For reasons of comparison, we included corresponding values for a free star ($\sigma_0 = 0$), which were taken from chapter 2 ($f = 10, 18, 30$) and Ref. [33] ($f = 50$), respectively. The dashed lines are guides to the eye in order to point out the monotonic decrease.

surface charges are distributed over the plane sufficiently dense, the compensation of charges is almost perfect, even without any absorbed star counterions.

Note that, because of the shift of configurational crossovers towards higher surface charge densities for system II, the release of star counterions is consequentially also 'delayed' in this case, as is obvious from the height of the respective peaks in Fig. 4.5. Moreover, the spatial distribution of the non-captured ions crucially depends on which system we are considering, too. For the capacitor-like setup I, the external field causes an accumulation near the upper plate and a depletion within the 'bulk' region in-between the walls, more and more pronounced as the field strength grows. The inset in Fig. 4.5(a) visualizes in detail what happens. For system II, due to the screening of the external field by the wall counterions and since the upper wall is neutral, there is no such inhomogeneous arrangement. Instead, a plateau value of the counterion density is reached far away from the lower surface, Fig. 4.5(b).

In order to highlight the release of star counterions from the star interior, we measured, as in the case of neutral walls, the total fraction $N_{\mathrm{in}}(f,\sigma_0)/N_-$ of trapped ions as a function of the surface charge density. For each value of σ_0, this measurement was implemented by counting all ions located within an imaginary sphere having the star's instantaneous, arm-averaged center-to-end radius and subsequently taking the time average (see also chapter 2). Fig. 4.6 shows data obtained for different functionalities f, again for both setups under consideration. The dashed lines serve as guides to the eye, clarifying the monotonic decrease. The results clearly confirm the above findings and point out another important trend. Since PE-stars with lower arm numbers experience a weaker steric repulsion by the wall due to their easier deformability (compare Refs. [126, 127] or chapter 2), they reach the starfish limit somewhat earlier. Here, this is apparent from the faster decay of the curves for lower f.

4.4 Equilibrium center-to-surface separation

A simulational measurement of a PE-star's average equilibrium center-to-surface distance $\langle D(f,\sigma_0)\rangle$ as a function of surface charge density and functionality allows to draw conclusions concerning the deviation of the configuration from sphericity. Fig. 4.7 shows such data for system I (main plot) and system II (inset), respectively. Again, the dashed lines were included as guides to the eyes. The obtained values for $\langle D(f,\sigma_0\rangle)$ are in any case smaller than the typical radius R_{s} of a free PE-star, or, equivalently, the typical range of the steric PE-star–wall repulsion arising from excluded volume effects and the concomitant deformation of the counterion cloud of the star (see chapter 2). Accordingly, the PE-stars are indeed, albeit in part weakly, bound to the lower wall for all values of σ_0 and f considered within the scope of this chapter.

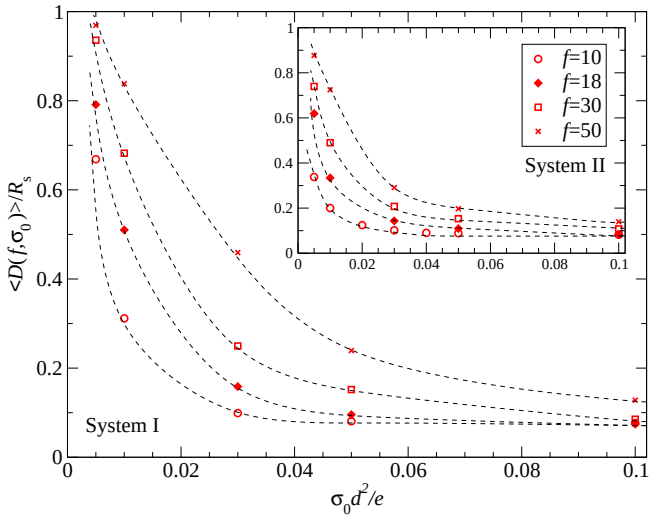

Figure 4.7: Relative equilibrium center-to-surface separation $\langle D(f,\sigma_0)\rangle / R_\mathrm{s}$ as a function of the surface charge density and for different functionalities. Results shown in the main plot are for the capacitor-like geometry (system I), while the data in the inset belongs to system II. The black, dashed lines are guides to the eye.

Since an amplification of the external field induces a tighter binding of the PE-stars to the substrate, the star–wall distances drop monotonically when increasing the surface charge density. On the other hand, the equilibrium separation grows monotonically for increasing functionality of the PE-stars, because their behavior changes from ultra-soft to stiff upon increasing the arm number. In the limit of high σ_0 and low f a plateau value for the distances is reached. It pertains to starfish-type configurations and is mainly determined by the radius of the PE-stars' colloidal core, with only a slight dependence on the arm number. A comparison of the two setups again verifies that the presence of additional wall counterions favors the formation of complexes for weak electric fields. In case of system II and for the low-σ_0 regime, the measured center-to-wall separations are systematically smaller than in system I for all f.

Fig. 4.8 displays the distribution $P(D)$ of the instantaneous center-to-surface distance D during the production runs of our MD simulations and the changes for different surface charge densities σ_0, part (a), or the PE-star functionalities f, part (b). For all sets of parameters, $P(D)$ is approximately of Gaussian form with the maximum indicating the mean separation $\langle D(f,\sigma_0)\rangle$, but typical height and width differ strongly. The former reflects the depth of the minimum of the total effective star–wall interaction, thus describing the stability of the binding of the respective complex: the higher the peak is, the deeper is the potential well and the more stable

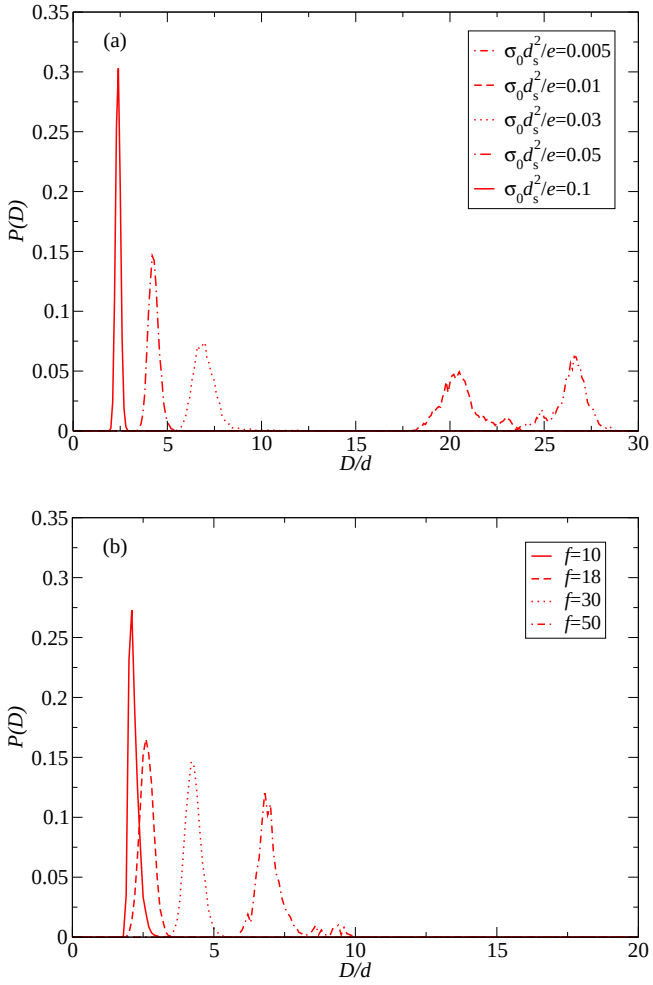

Figure 4.8: Distribution $P(D)$ of a PE-star's instantaneous center-to-surface distance D, exemplarily for the capacitor-like geometry of system I. The two panels of the figure illustrate the influence of (a) the surface charge density σ_0 (for $f = 30$) and (b) the functionality f (for $\sigma_0 d^2/e = 0.05$) on the shape of the profiles $P(D)$. Their approximately Gaussian form persists, but position, width, and height vary strongly when changing the arm number and the strength of the external electric field.

is the star attached to the substrate. The latter reveals how strong the core position of a PE-star is vibrating around its equilibrium value and expresses the broadness of the attractive potential well. For a wider maximum, fluctuations around the average center-to-surface distance are more pronounced. The detected trends are perfectly consistent with our previous findings. For increasing σ_0 or decreasing f the effective interaction develops a deeper and more narrow minimum due to the stronger external electric field or the weaker steric star–wall repulsion (see Fig. 4.8). Hence, the PE-star approaches the surface more closely, the bonding is intensified and thermal fluctuations of the core position almost diminish in the starfish limit.

4.5 Effective PE-star–wall forces

In analogy to Sec. 2.4, we measured effective PE-star–wall forces [4, 100] for system II as a function of the PE-stars' center-to-surface distance D. Exemplary results for $f = 18$ and $\sigma_0 d^2/e = 0.01$ are shown in Fig. 4.9. The general, non-monotonic shape of the force-vs.-distance curve, featuring a divergence of steric origin as $D \to 0$, a minimum, and an almost saturation-like flattening for large distances D, can be understood in terms of the interplay between two counteracting contributions adding to the total effective force, explained in detail in what follows.

For very small D, steric star–wall repulsions analogous to our findings for neutral walls in chapter 2 dominate the behavior. But with increasing distance this repulsion reduces rapidly. Additionally, there are electrostatic attractions present acting between the PE-star and the charged substrate. Indeed, their strength also decreases as D grows due to stronger screening effects induced by the positive wall counterions and the reduction of the PE-star's net charge due to counterion capturing. However, this decay is much slower. Accordingly, there exists a certain value of D for which the two contributions exactly balance each other. The total effective force vanishes, thus determining the star's equilibrium distance $\langle D(f, \sigma_0) \rangle$. As already discussed, it is large for low surface charge densities and high functionalities. In Fig. 4.9, its value as obtained independent from the force measurements (compare also Fig. 4.7) is marked by a black cross and a corresponding error bar. Upon a further increase of D, electrostatic forces dominate and the total effective force becomes attractive with rising absolute value, since the fast decline of the repulsive part still over-compensates for the weakening of the electrostatic attraction due to stronger screening. Since the steric repulsion has a typical range of about the star radius R_s, the latter is an upper boundary for the position of the minimum of the overall force. For stronger external electric fields, this position shifts towards smaller center-to-surface distances. Beyond the minimum, F_eff directly inherits the property of the electrostatic force to decay in strength due to screening induced by the wall counterions present for system II, i.e., its absolute value decreases again.

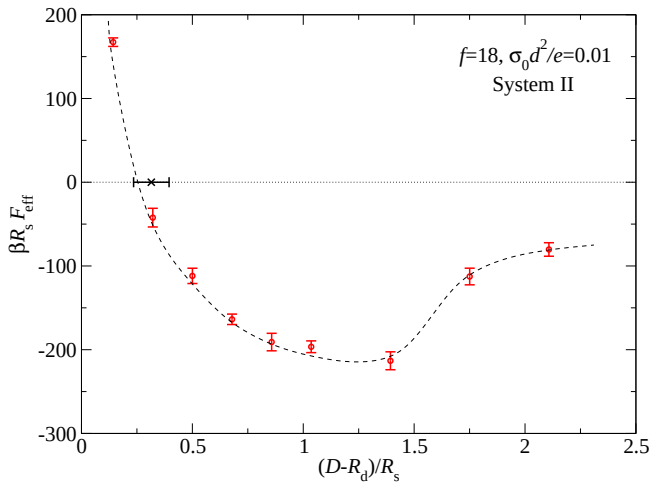

Figure 4.9: Effective force F_{eff} acting between a PE-star and a charged, planar wall as a function of the center-to-surface separation D, exemplarily shown in case of system II for $f = 18$ and a surface charge density $\sigma_0 d^2/e = 0.01$. The red data points are results as obtained by our MD simulations, while the dashed, black line is a guide to the eye. The black cross with its corresponding error bar marks the star's measured equilibrium position for the given parameter combination.

Nevertheless, the force still remains attractive with respect to the lower wall. In the limit of very large D, almost all wall counterions will be situated between the substrate and the star, perfectly screening the external field, and the majority of star counterions will be trapped in the interior of the star. The attraction must therefore disappear.

For system I, the distance-dependence of the force for very small D must also be dictated by the strong steric repulsion between the PE-star and the lower hard wall. But for larger D, we expect a different and less intricate behavior compared to system II. Due to the lack of additional wall counterions, there is hardly any screening of the external electric field. Therefore and since above a certain value of D there is only little deformation of the PE-star and consequentially the number of trapped counterions does not change significantly anymore, the electrostatic attraction pulling the PE-star towards the lower wall does not become weaker with increasing distance. This is in contrast to what we found for system II. Hence, it is unlikely to observe any pronounced, non-monotonic behavior of the total force. Instead, once electrostatic forces dominate and steric repulsions become irrelevant, the total force will remain almost constant.

Finally, in order to verify that for system II and $D \gtrsim R_{\text{s}}$, i.e., beyond the minimum of the force curve, the functional form of the latter is solely determined

$(D-R_\mathrm{d})/R_\mathrm{s}$	N_scr	$\beta R_\mathrm{s} F_\mathrm{scr}$	$\beta R_\mathrm{s} F_\mathrm{eff}$
1.39	113	-174	-213.3
1.75	92	-130	-109.4
2.11	74	-77	-78.5

Table 4.1: Comparison of simulation results for the effective PE-star–wall forces and estimates for the same according to Eq. (4.11) as obtained assuming the wall counterions to mainly govern the behavior, here exemplarily for $f = 18$.

by the attraction due to the screened external electric field and the wall counterions thus crucially influence the physics, we present a simple approximative approach to assess $F_\mathrm{eff}(D)$ for the high-D regime. Let $N_\mathrm{scr}(D)$ be the average number of positively charged ions located in-between the lower plate and the PE-star, i.e., with $z_- \leq z \leq D - R_\mathrm{s}$, as measured in our simulations. Exactly these ions screen the electric field affecting the star. We define an (uniform) effective, distance-dependent surface charge density:

$$\sigma_0^{(\mathrm{scr})}(D) = \sigma_0 - \frac{N_\mathrm{scr}(D)}{M^2}. \tag{4.8}$$

Therewith, an allowedly somewhat crude approximation for the resulting field exerting an attractive force on the PE-star reads as:

$$\mathbf{E}_\mathrm{scr}(D) = -2\pi\sigma_0^{(\mathrm{scr})}(D)\,\hat{\mathbf{z}}. \tag{4.9}$$

As ascertained in Sec. 4.3, for large values of D the weakly deformed PE-stars still maintain the ability to absorb the vast majority of their counterions due to Manning condensation [104–106] and ion capturing. The net charge Q_s^* is reduced considerably compared to its bare value $Q_\mathrm{s} = \alpha f N e$,

$$Q_\mathrm{s}^* = (\alpha f N - N_\mathrm{in})e \equiv N_\mathrm{s}^* e. \tag{4.10}$$

Together with Eq. (4.9), a rough estimate for the (dimensionless) effective force dragging the PE-star center is then given by

$$\beta R_\mathrm{s} F_\mathrm{scr}(D) = -2\pi R_\mathrm{s} N_\mathrm{s}^* \left(\frac{\lambda_\mathrm{B}}{e}\right) \sigma_0^{(\mathrm{scr})}(D). \tag{4.11}$$

For the parameters pertaining to the data shown in Fig. 4.9, we now check the above estimates against actual results. Table 4.1 shows a corresponding comparison for three different center-to-surface distances, including the respective numbers of positive ions evoking the screening. Note that, in case of ($f = 18$)-arm stars, we have $R_\mathrm{s}/d = 28.0$ and $N_\mathrm{s}^* = 68$ (see also Table 2.1). As can be seen, our guess is

not capable of quantitatively reproducing the effective forces, but we have at least qualitative agreement and the general trends are expressed correctly. Consequently, we can conclude that the high-D effective star–wall forces for system II are indeed merely arising from Coulombic interactions and the behavior is thus determined by the screening of the external field due to the wall counterions.

4.6 Configurational phase behavior

As already detected in the previous sections by means of several quantities measured during our simulation runs, PE-stars in planar confinement under the influence of a homogeneous, external electric field experience conformational changes when varying, e.g., the PE-star functionality or the surface charge density. The possible morphologies range from almost spherical configurations, where the PE-stars are loosely bound to the charged substrate, to the opposite extreme of starfish-like, two-dimensional, fully collapsed situations. However, we did so far not present any detailed conclusions concerning possible intermediate configurations or the structural crossovers between different morphologies. Clearly, since we are dealing with continuous configurational changes of single (macro-)molecules, there are no real phase transitions in the sense of statistical mechanics. The latter are defined only within the thermodynamic limit, but a single PE-star consists of a finite number of particles. There are no sharp boundaries separating areas in the (f, σ_0)-plane belonging to a certain class of morphology, but just diffuse crossover regions. Nevertheless, we are going to refer to the crossovers as 'transitions', synonymously, and call the different classes of typical configurations morphological 'phases' or 'states' in what follows for sake of brevity. Thereby, one should always keep in mind how such terminology has to be understood in our case.

Figs. 4.10 and 4.11 show characteristic snapshots for systems I and II, respectively, at all points in the (f, σ_0)-plane where we carried out simulations, exemplarily demonstrating that there indeed are several, distinct classes of arrangements. In particular, a closer inspection reveals the existence of three states besides the aforementioned limiting cases, to be discussed in what follows.

When increasing the strength of the external field, deviations from sphericity must occur. As expected, the average center-to-surface distance of the stars decreases (cf. Fig. 4.7), but for not too high surface charge densities and not too low functionalities the colloidal core does not reach the closest approach possible, which is determined by its finite hard core radius and the range of the additional LJ repulsion acting between the central particle and the wall. In other words, the electrostatic attraction is not yet strong enough to overcome the steric star–wall repulsion also for small D. Hence, there are no arms lying flat on the substrate. Instead, only the outer ends of the chains in the lower hemisphere attach to the plane,

forming acute angles with the surface normal $\hat{\mathbf{z}}$, while the distribution of arms in the upper hemisphere remains more or less undisturbed. The resulting configurations are jellyfish-like, as realized for, e.g., $f = 30$ and $\sigma_0 d^2/e = 0.01$ in case of both setups. The binding to the substrate is still rather weak and the star's position fluctuates considerably around its mean value, see also Fig. 4.8.

Upon a further growth of σ_0 or for a lower arm number f, the stars are pulled directly onto the wall, with their center-to-surface distance now of the order of the core particle's diameter. About $f/2$ arms fully stick to the wall, whereas the remaining chains are still distributed evenly within a hemisphere, as, e.g., for $f = 50$ and $\sigma_0 d^2/e = 0.05$ in both systems I and II. The minimum of the effective potential is rather deep and narrow, thus the anemone-like looking complex is very stable.

For external electrostatic forces even stronger compared to the steric PE-stars–wall repulsion, a bigger fraction of chains folds down to the charged surface. Before ending up in the starfish limit, there are antenna-type configurations appearing, where only a small number of arms sticks out approximately perpendicular to the plane. There is nearly no movement of the star center along the z-axis anymore, as illustrated in Fig. 4.8. The stability of the adherence to the wall is extremely high, already comparable to the case of full collapse. For both setups, such antenna conformations can be observed for, e.g., PE-stars with $f = 18$ arms and a surface charge density $\sigma_0 d^2/e = 0.03$.

A comparison of the snapshot collections for the situation without and with wall counterions, Figs. 4.10 and 4.11, respectively, shows that the arising morphologies and the general trends for the crossovers between them are very much the same. Only the locations of typical crossover regions characterizing the configurational transitions are shifted, as could be expected from our above findings. In this sense, the additional ions do influence the morphological behavior of the PE-stars. In what follows, we will now introduce quantitative criteria to distinguish the occurring classes of conformations and to subsequently describe transitions between them (Secs. 4.6.1 and 4.6.2). The final goal is to draw corresponding morphological phase diagrams (Sec. 4.6.3).

4.6.1 Morphological criterion

The different PE-star morphologies – besides the respective equilibrium center-to-surface distances $\langle D(f, \sigma_0) \rangle$ and the stability of the adhesion to the substrate – mainly differ with respect to the spatial arrangement of the constituent PE-chains, particularly the typical directions the latter are pointing at. Thus, a quantitative criterion to distinguish the ensuing configurational states must conveniently reflect such information. The current orientation of an individual arm, arbitrarily labeled

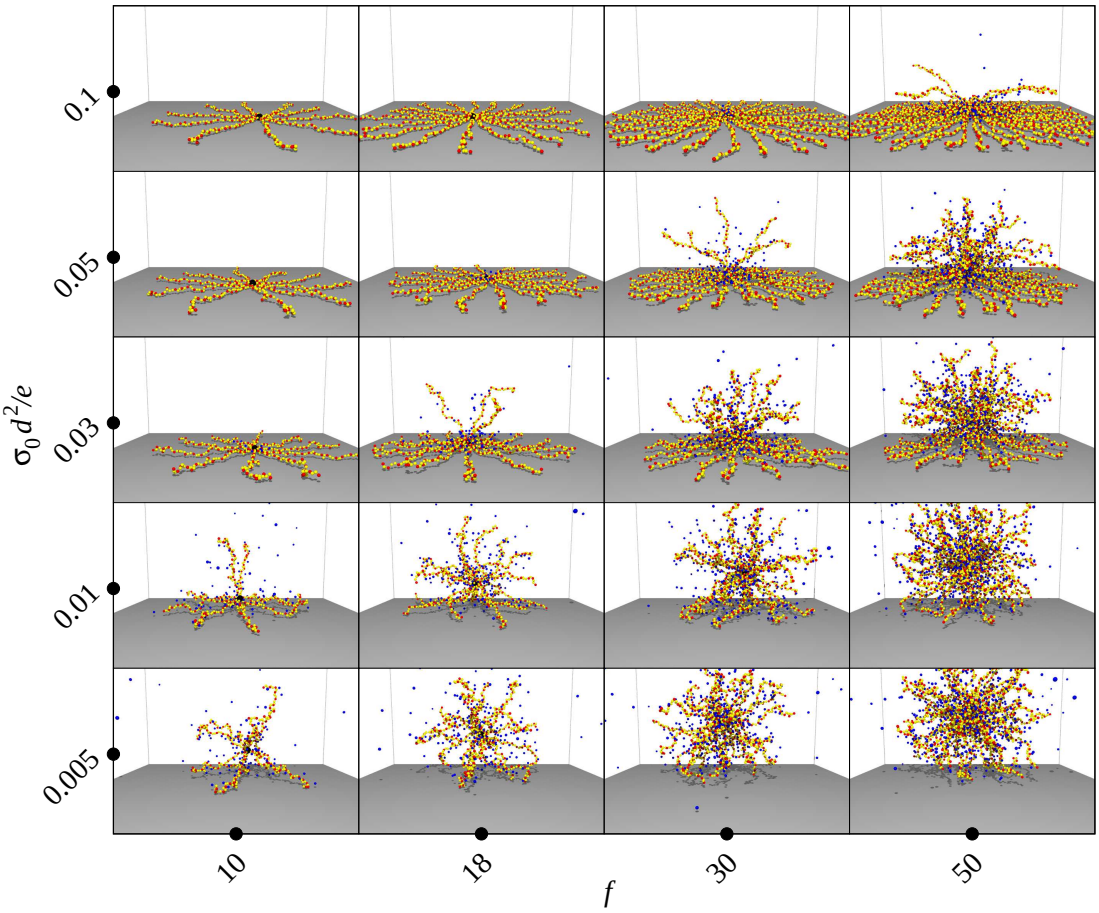

Figure 4.10: Collection of exemplary snapshots for system I and all points in the (f, σ_0)-plane where we carried out MD simulations. There is a distinct dependence of the morphology of the formed complexes on the PE-star functionality f and the surface charge density σ_0, ranging from almost spherical conformations for weak fields and highly-branched stars to flat, starfish-like arrangements in the opposite limit of strong external fields and low arm number.

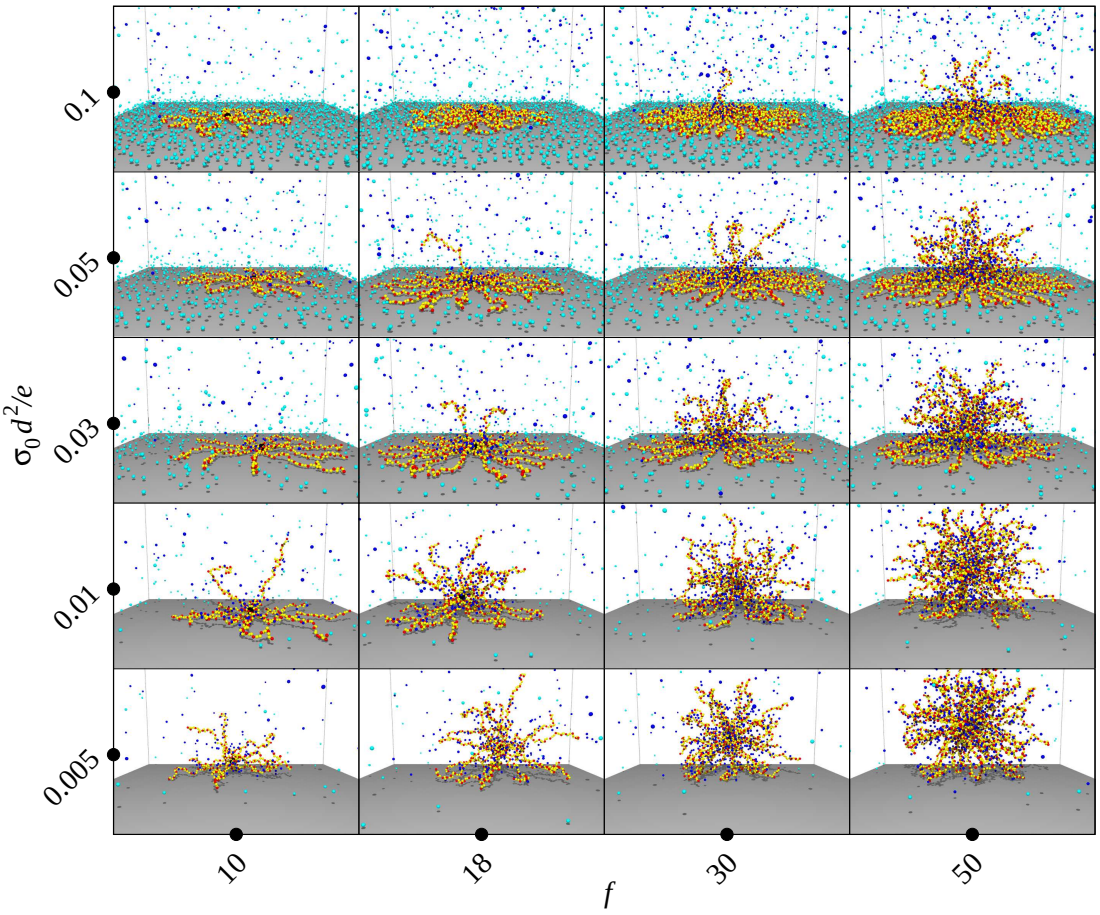

Figure 4.11: The same as Fig. 4.10, but for system II instead of the capacitor-type geometry I, including positively charged wall counterions (light blue). From a comparison of the setups it becomes clear that the general trends concerning the morphological behavior are the same, but the configurational transitions are shifted with respect to their f- and σ_0-dependence.

i with $0 \leq i < f$, can be described by its instantaneous center-to-end vector,

$$\mathbf{R}_i = \mathbf{r}_{i,N} - \mathbf{r}_{\text{core}}, \tag{4.12}$$

where $\mathbf{r}_{i,N}$ denotes the position of the N-th (last) monomer in the chain sequence of chain i and $\mathbf{r}_{\text{core}}$ specifies the location of the colloidal core of the star. Calculating the inner product of $\mathbf{R}_i/|\mathbf{R}_i|$ and the surface normal $\hat{\mathbf{z}}$ of the lower, attracting plane yields the cosine of the angle θ_i between the two. Hence, calculating the time average during our simulation runs characterizes the average orientation of each arm:

$$\langle \cos\theta_i \rangle = \left\langle \frac{\mathbf{R}_i}{|\mathbf{R}_i|} \cdot \hat{\mathbf{z}} \right\rangle. \tag{4.13}$$

Note that, since the PE chains are formally grafted on the colloidal core's surface without any fixed position of their innermost monomers and the arms may thus exchange positions during sufficiently long simulation runs by virtue of thermal fluctuations, one could suppose the averaging to yield $\langle \cos\theta_i \rangle = 0$ for all i independent on the actual PE-star morphology. Due to the very high values of the monomer density close to the center even for the smallest functionalities f considered here, such swapping processes can not take place. Therefore, as long as there is no angular momentum exerted on the star leading to a rotation of the entire star, we obtain $\langle \cos\theta_i \rangle = 0$ if and only if chain i lies flat onto the plane.

It is important to remark that sets of averaged cosines for a PE-star as introduced above not only express orientational data for the individual arms, but also implicitly measure the mean PE-star–wall separation for the given parameters. More precisely, ignoring chain bending or compression and pursuant to simple geometrical relations, it approximately holds:

$$-\min_i \langle \cos\theta_i \rangle = \frac{\langle D(f,\sigma_0) \rangle}{R_{\text{s}}(f,\sigma_0)} \tag{4.14}$$

Consequently, plotting $-1 \leq \langle \cos\theta_i \rangle \leq 1$ as a function of the normalized arm index $0 \leq i/(f-1) \leq 1$ comprehensively depicts the shape of a PE-star and is a convenient quantity to describe the morphology. In order to guarantee optimal comparability of the resulting graphs, we (re-)assign the indices i in such a way that the values of $\langle \cos\theta_i \rangle$ are arranged in descending order. This is possible without tampering the data since the labeling was anyway completely arbitrary.

Fig. 4.12 shows representative results for system I and all five classes of morphologies as yet only qualitatively identified based on simulation snapshots, ranging from almost spherical configurations, part (A), to starfish complexes, part (E). The respective functionalities f and surface charge densities σ_0 are given within the different panels of the figure. The shapes of the curves vary strongly, indeed rendering them an appropriate tool for a quantitative characterization of the configurational states and the continuous transitions between them.

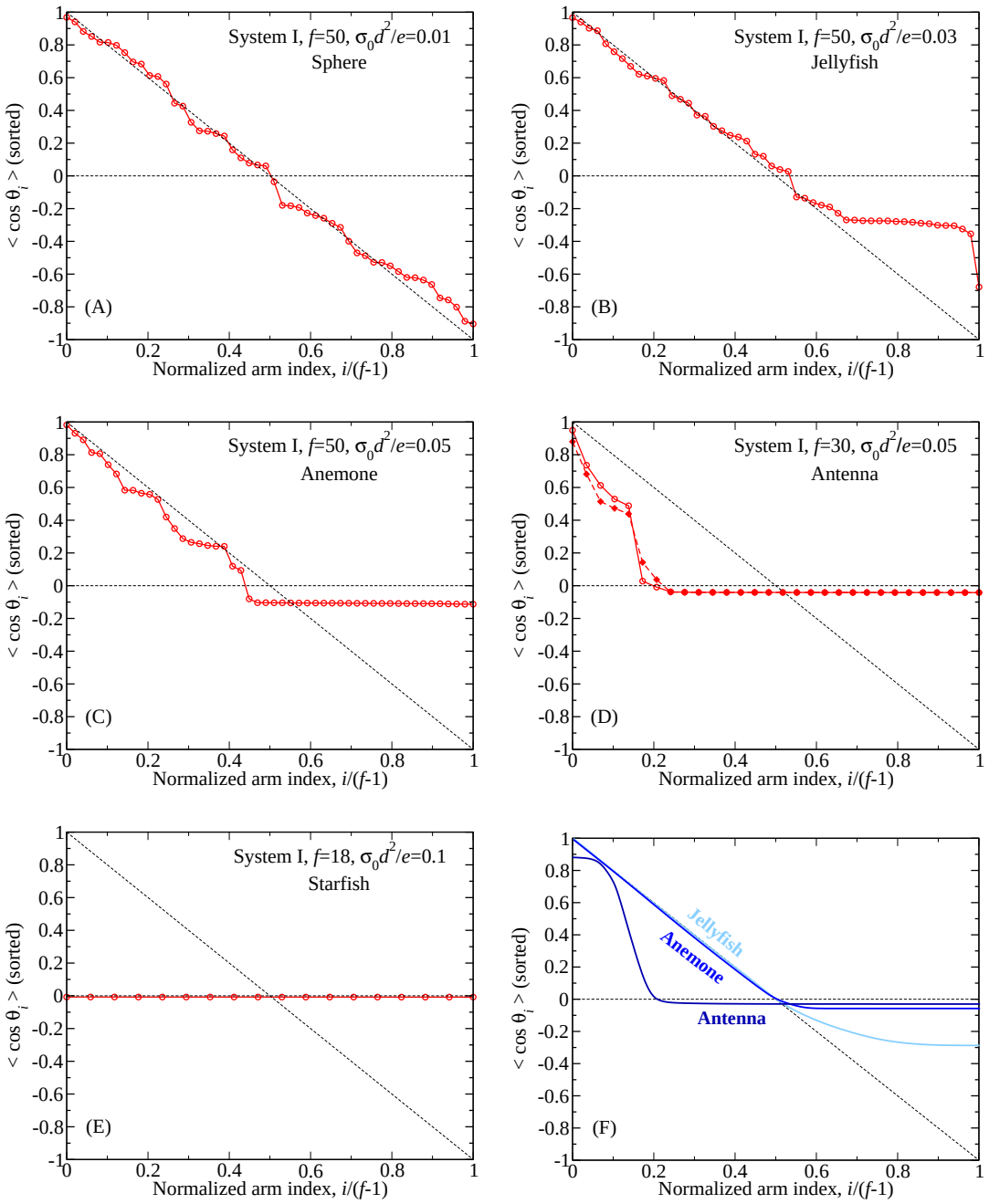

Figure 4.12: Representative graphs visualizing the criterion to distinguish possible types of PE-star configurations. Plotting $\langle \cos \theta_i \rangle$ in descending order against $i/(f-1)$ yields five different classes of functional shapes, each belonging to a separate morphology: sphere (A), jellyfish (B), anemone (C), antenna (D), and starfish (E). The sketch in part (F) of the figure was included in order to clarify the basic differences between the intermediate states (B) to (D). The two curves in part (D) show results obtained starting our simulation runs from different initial configurations.

The typical appearance in both limiting cases, i.e., sphere and starfish, is rather obvious. In the former situation, the values of $\langle\cos\theta_i\rangle$ are evenly covering the entire interval $[-1,1]$, since the PE-chains are uniformly distributed over the entire solid angle $\Sigma = 4\pi$. Accordingly, the resulting graph must approximately coincide with a diagonal running from the upper left to the lower right corner of the plot, see Fig. 4.12(A). In the starfish case, all the arms are adsorbed to the substrate completely and over their full length. The resulting function is constant, equal to a small negative number (almost zero), as mainly determined by the finite radius of the core particle, compare Fig. 4.12(E).

In order to exemplify the functional form of the $\langle\cos\theta_i\rangle$-vs.-$i$ plots for the intermediate states (B) to (D), the sketch in Fig. 4.12(F) was included. As illustrated, the graph bends away from the diagonal upon increasing the strength of the external electric field. This process starts from the high-i end of the re-ordered abscissa and propagates towards lower values of i. For jellyfish-type configurations, the primary shape remains for $i/(f-1) \lesssim 0.5$, while a negative plateau value is reached for higher i. The latter is defined by the aperture angle of the cone opening towards the lower plate on whose surface the 'tentacles' of the jellyfish are located approximately. In particular, the absolute value of the plateau is articulately greater than zero, since the affected PE-chains do not lie flat, and smaller than one. Note that the outlier to the extreme right in Fig. 4.12(B) directly confirms the occurrence of compression effects as suggested in chapter 2 [126, 127]. Individual chains are rather stiff due to their charging and strong bending is thus not favorable. Since all arms belonging to the plateau have about the same length given by the star radius $R_{\rm s}(f,\sigma_0)$, any arm with a value of $\langle\cos\theta_i\rangle$ significantly smaller than the plateau value must clearly be compressed for geometrical reasons.

For anemone-like conformations, the left branch of the graph describing the morphology is still unchanged and runs along the diagonal, i.e., about $f/2$ arms are sticking out of the lower plane evenly distributed in a hemisphere with its center close to the substrate. The plateau value for $i/(f-1) \gtrsim 0.5$ approaches zero, because the other half of the chains is already confined to the surface [Fig. 4.12(C)]. For growing surface charge densities σ_0, more and more chains fold down, the width of the plateau increases, and the plateau value approaches zero even closer. To the left of the plateau follows a step-like jump up to a narrow region with higher values of $\langle\cos\theta_i\rangle$, since a little number of arms still points upwards, now almost perpendicular to the substrate: an antenna-type arrangement is reached [Fig. 4.12(D)].

As already suggested in Sec. 4.2.1, for several different parameter combinations (f,σ_0) we performed simulation runs starting from two alternative initial configurations, namely hemispherical and starfish-like conformations. This allows for an careful check if true equilibrium states are reached and if any hysteresis may influence the f- and σ_0-dependence of the PE-stars' morphological phase behavior. Fig. 4.12(D) exemplarily shows a comparison of such results. Open circles refer to a

hemispherical initial configuration, filled diamonds to a starfish-type one. In general, we can conclude that there is no significant dependence on the initial conditions and hysteresis effects are clearly negligible.

Fig. 4.13 is devoted to a comparison of corresponding plots for systems I and II, or, equivalently, the question how the existence of positively charged wall counterions affects the f- and σ_0-dependence of the conformational behavior. The results immediately support and verify the findings and conclusions of Sec. 4.3. There are no fundamental changes, but for weak external fields the wall counterions induce an earlier onset of the PE-star–wall complexation process and shift the conformational transitions towards lower surface charge densities σ_0 and higher functionalities f. For the parameters in Fig. 4.13(a), though the morphology can be classified as spherical for both setups, the deviations from sphericity are more pronounced in case of the system II. In Fig. 4.13(b), the type of morphology indeed changes. While for the capacitor setup I we observe a jellyfish configuration, the adhesion to the plane is distinctly stronger for system II and we identify an anemone-like structure. By contrast and as expected, in the high-σ_0 regime the impact of the additional ions is exactly the other way around, exemplarily illustrated by Fig. 4.13(c). For system I, we already arrived at the starfish-limit, but for the alternative setup II the PE-star is yet prevented from a full collapse into a two-dimensional state.

Finally, we study the density-dependence of the PE-star morphology which is important from a technological point of view with regard to possible applications. Only if the complexation processes and thus the configurational phase behavior are stable against variation of the PE-star density, at least within a certain range, it is practically possible to make use of our results in order to create PE-star arrays onto a charged substrate and to precisely tune their physical properties. For this purpose, Fig. 4.14 compares $\langle \cos \theta_i \rangle$-vs.-$i$ plots as obtained for system II, exemplarily chosen values of f and σ_0, and two different PE-star densities per surface unit area,

$$\lambda_\mathrm{s} = \frac{N_\mathrm{s}}{M^2}. \tag{4.15}$$

Here, N_s denotes the number of PE-stars in our simulation box and M is the edge length of the confining plates, compare also Secs. 2.2 and 4.2. Note that all other plots throughout this chapter show results as obtained for $\lambda_\mathrm{s} R_\mathrm{s}^2 = 0.05$.

There are no major differences upon changing the density as long as sufficient dilution is guaranteed, i.e., for the density remaining below its corresponding overlap value $\lambda_\mathrm{s}^* R_\mathrm{s}^2(f, \sigma_0) = 1/\pi$. Only for higher PE-star concentrations completely new effects like PE multi-layering on the surface might occur [88, 102]. However, even in the dilute case the (diffuse) crossover regions will in part shift slightly upon increasing the density. Fig. 4.14(a) illustrates a case where the morphological structure of the PE-star–wall complex alters from anemone-like to jellyfish. In contrast, in part (b) the configurational classification as antenna-type persists, but the num-

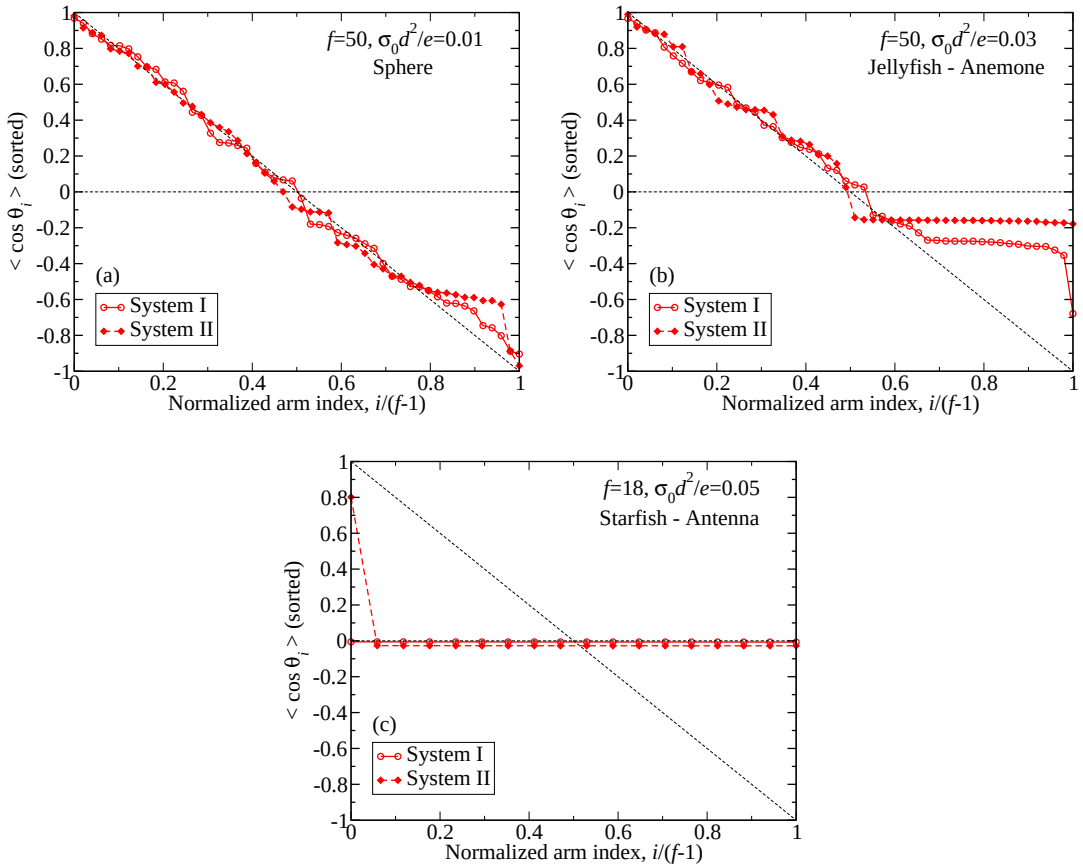

Figure 4.13: Differences in the morphological phase behavior between setups I and II, illustrated by means of three exemplarily chosen parameter combinations. It emerges that the presence of positively charged, freely moving wall counterions indeed influences the f- and σ_0-dependence of the found configurational structures. The observations are in full agreement with previous conclusions based on the measurement of all particle species' density profiles.

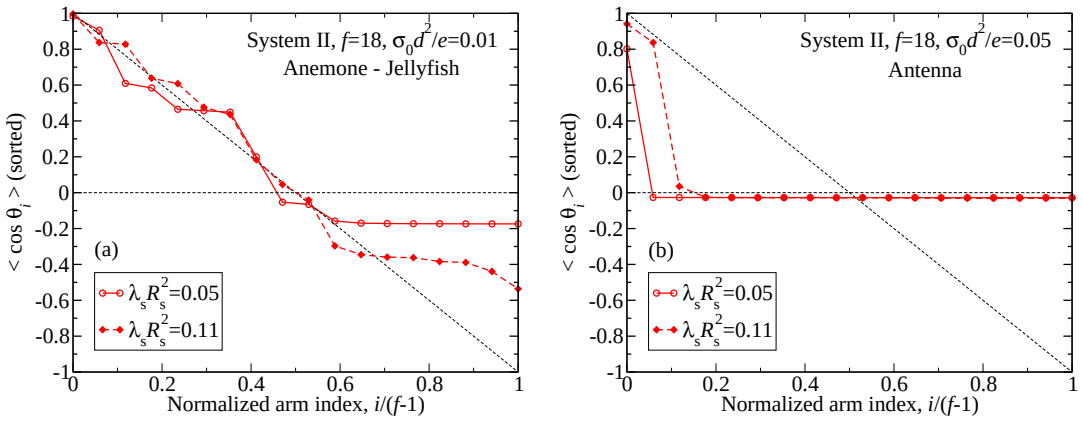

Figure 4.14: Density-dependence of the PE-star morphology, here for functionality $f = 18$ and surface charge densities (a) $\sigma_0 d^2/e = 0.01$ and (b) $\sigma_0 d^2/e = 0.05$. In each case, results for two different values of the star density per substrate unit area, $\lambda_s R_s^2$, as indicated in the legend boxes are shown. As long as the density remains sufficiently low, there are no substantial changes. The anyway diffuse phase boundaries experience a slight shift.

ber of arms sticking out of the attracting plane grows. In general, the basic trend when increasing the density is always the same. The binding of the PE-stars to the substrate becomes weaker and complex formation is impeded, accordingly the crossovers between different morphological classes happen at higher surface charge densities σ_0 and smaller arm numbers f.

4.6.2 Two-dimensional order parameter

In general, it is desirable to introduce a (possibly multi-dimensional) order parameter describing the morphological phase behavior of PE-stars near charged, planar substrates instead of plotting $\langle \cos \theta_i \rangle$ in descending order vs. the normalized arm index $i/(f-1)$. An appropriate possibility to define such order parameter is to fit the latter graphs with the function

$$h(x; x_0, y_0) = \begin{cases} (y_0 - 1)\frac{x}{x_0} + 1 & \text{for } 0 \leq x \leq x_0 \\ y_0 & \text{for } x_0 < x \leq 1. \end{cases} \tag{4.16}$$

Here, x_0 and y_0 are the fit parameters. The procedure is exemplarily demonstrated in the inset of Fig. 4.15. Due to their typical shapes, the graphs are reasonably approximated by $h(x; x_0, y_0)$ for all conformational states (cf. also Fig. 4.12).

Performing the fit for all points in the (f, σ_0)-plane where we carried out simulations thus yields the fit parameters as a function of the functionality and the surface

Morphology	O_1	O_2
Sphere	1	1
Jellyfish	β	1
Anemone	0	1
Antenna	0	γ
Starfish	0	0

Table 4.2: Ideal values for the two-dimensional order parameter $O = (O_1, O_2)$, with positive numbers $\beta < 1$ and $\gamma < 1$. In reality, the values for the different classes of morphologies are not as sharply circumscribed, since the configurational crossovers are continuous.

charge density, $x_0 = x_0(f, \sigma_0)$ and $y_0 = y_0(f, \sigma_0)$. Indeed, we do not consider x_0 and y_0 themselves to describe the configurational behavior of the PE-stars, but use the more convenient definitions

$$O_1 = \left| y_0 - \frac{R_\mathrm{d}}{R_\mathrm{s}(f, \sigma_0)} \right| \tag{4.17}$$

and

$$O_2 = \frac{2x_0}{1 - y_0}, \tag{4.18}$$

acting as components of the two-dimensional order parameter $O = (O_1, O_2)$. In Eq. (4.17), the shift of y_0 by $R_\mathrm{d}/R_\mathrm{s}(f, \sigma_0)$ arises from geometry and is due to the finite radius of the core particles, preventing the arms from sticking to the substrate entirely flat even for fully collapsed configurations. Theoretically, we should always have $0 \leq O_1 \leq 1$ and $0 \leq O_2 \leq 1$. In practice, since the left, descending branch of the $\langle \cos \theta_i \rangle$-vs.-$i$ plots as measured in our simulations might lie above the dashed diagonal to a certain extent, the value of O_2 may exceed the upper boundary a little. The ideal values for the two-dimensional order parameter for the five morphological phases are summarized in Table 4.2.

Fig. 4.15 shows results as obtained based on our simulation data. Here, open and closed symbols pertain to systems I and II, respectively. The dashed ellipses indicate the attribution of data points to different configurational classes. They partly overlap, symbolizing that in reality areas in the (O_1, O_2)-plane belonging to a certain state are not always as sharply circumscribed as Table 4.2 suggests, but smeared out to some extent. Nevertheless, the separation is sufficiently clear, only in case of the transition sphere–jellyfish the interpenetration is distinct and the crossover region is rather broad due to very pronounced conformational fluctuations as typical for weakly bound complexes. On the other hand, the domain occupied by data points for starfish-type configurations is extremely small and well-defined, since the strong

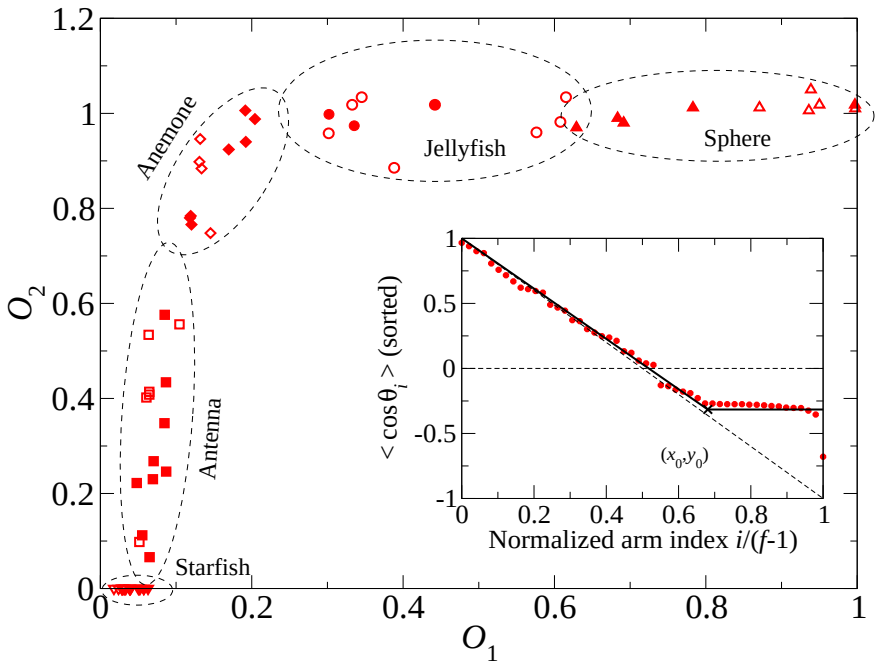

Figure 4.15: Two-dimensional, continuous order parameter (O_1, O_2) as calculated based on the $\langle \cos\theta_i \rangle$-vs.-$i$ plots. Open and closed symbols pertain to systems I and II, respectively. Dashed ellipses indicate the attribution of data points to different morphological classes. The inset depicts the underlying fitting procedure and the definition of the order parameter. For a detailed description, see main text.

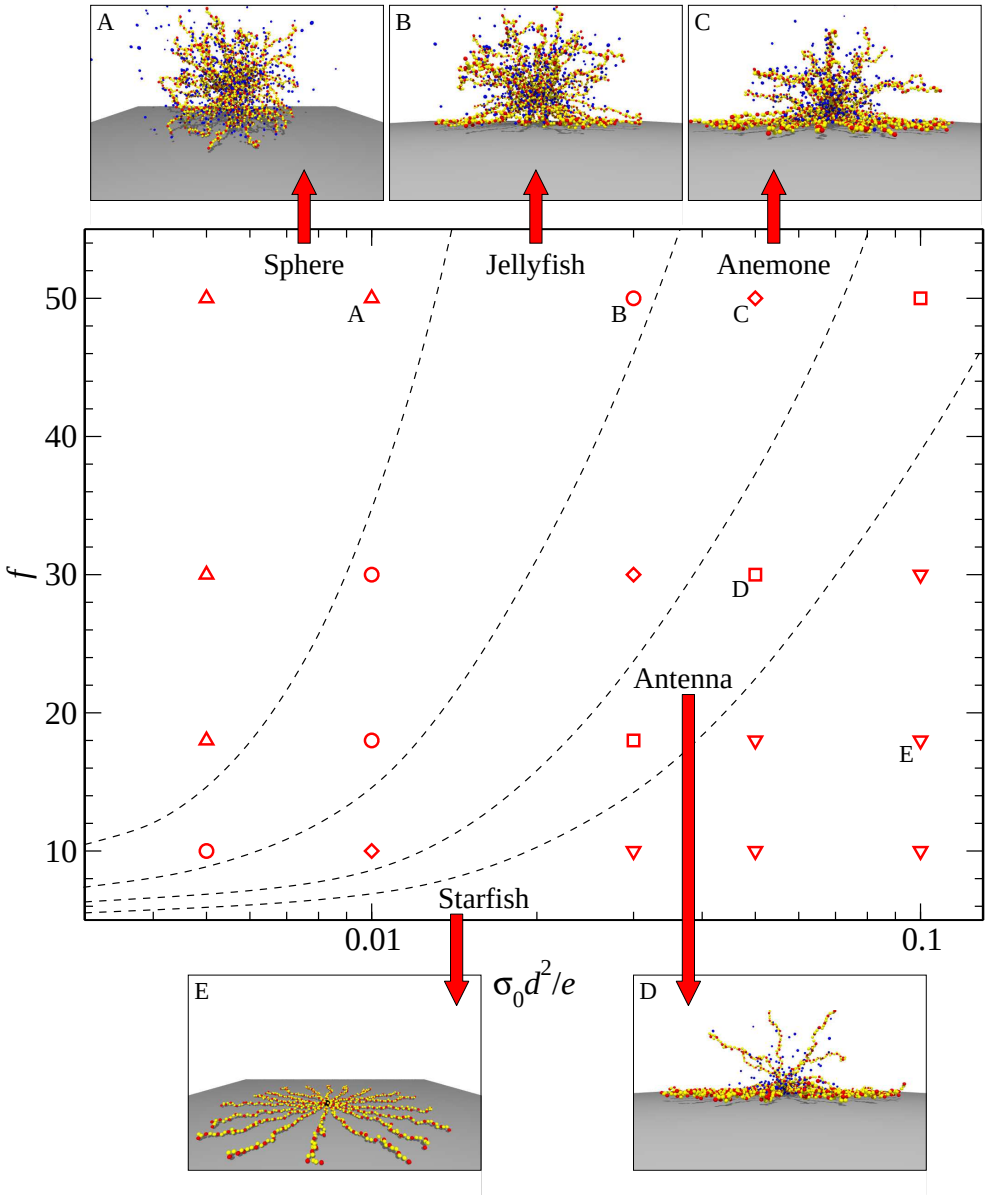

Figure 4.16: Configurational phase diagram for system I and a PE-star density per surface area of $\lambda_s R_s^2 = 0.05$. Dashed lines serve as guide to the eye, separating different classes of morphologies and showing fundamental trends how configurations change upon variation of f and σ_0. Exemplary snapshots are shown for either case, the corresponding parameter combinations are marked by uppercase letters A to E.

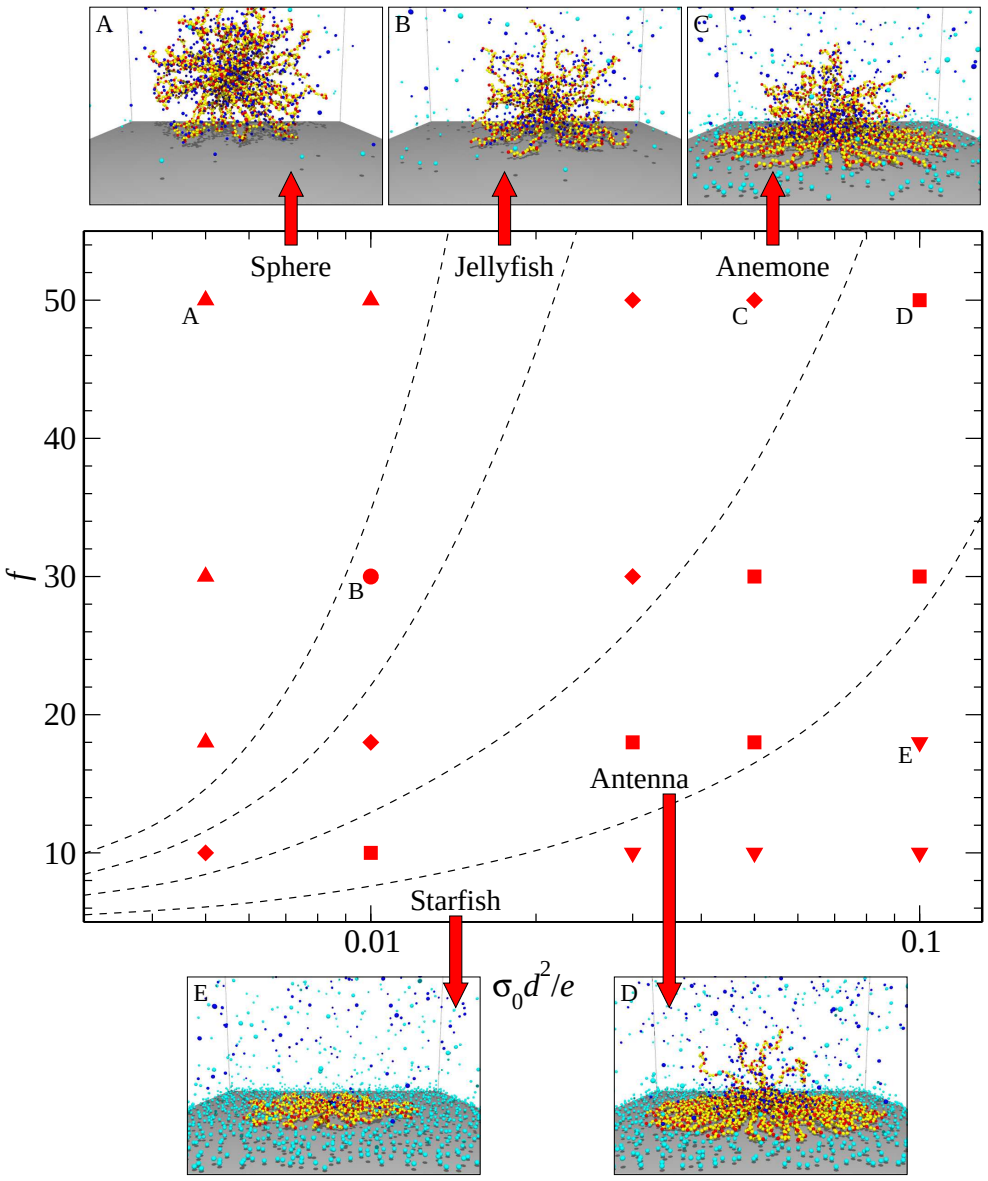

Figure 4.17: The same as Fig. 4.16, but for system II. Phase boundaries move slightly compared to the capacitor-like geometry, see main text for an analysis.

confinement to the surface by virtue of the external electric field efficiently suppresses fluctuations of the monomer positions. Hence, the corresponding graphs for $\langle \cos \theta_i \rangle$ in very good approximation show ideal behavior as depicted in Fig. 4.12(F).

4.6.3 Configurational phase diagrams

Figs. 4.16 and 4.17 are the core pieces of this chapter, showing configurational phase diagrams as obtained based on the quantitative criteria introduced above for setups I and II, respectively. The PE-star density per surface unit area was chosen to be $\lambda_s R_s^2 = 0.05$, the lower one of the values compared in Fig. 4.14. In either plot, data points again belong to positions in the (f, σ_0)-plane where we carried out MD simulations. Note that the σ_0-axis is scaled logarithmically. Dashed lines serve as guides to the eye, separating regions pertaining to different classes of morphologies and illustrating the basic trends for configurational changes upon variation of the PE-star functionality f and the surface charge density σ_0, i.e, the location of the crossover regions. To visualize the decisive differences of the structural states, representative snapshot are shown for each of these and for both systems under investigation. The corresponding parameter combinations are marked by uppercase letters A to E [corresponding to parts (A) to (E) in Fig. 4.12].

In general, the larger the functionality f, the more strongly PE-stars resist complex formation. Consequently, stronger external fields are needed to reach a given degree of complexation, i.e., a certain morphological structure. The phase diagrams reflect this characteristic in the positive slope of the dashed boundaries. Above a critical arm number, with the concrete value depending on the setup, the punishment in terms of free energy is too high to reach the starfish limit for realistic surface charge densities, i.e., for $\sigma_0 d^2/e \lesssim 0.1$. In contrast, for very small f, the PE-stars are rather blurred objects [32, 33], accordingly the steric star–wall repulsion is very soft [126, 127] and completely flat configurations are easily obtained for very small fields. Thus, for low values of σ_0, all boundaries are running nearly in parallel to the horizontal axis. From an application-oriented point of view, it is important to state that the crossover regions symbolized by the dashed lines are sufficiently narrow to render the phase diagrams useful for an exact tailoring of the structural properties of PE-stars adsorbed to a charged substrate. In this connection, cf. also Fig. 4.15, where the overlap of ellipses depicting the belonging to different phases is finite but rather small.

Comparing results for setup II to their counterparts for setup I again reveals that the presence of additional cationic wall counterions compensating for unbalanced surface charges does not bring about fundamental changes, but causes a shift of the boundary regions separating areas for different morphological states. For entropic reasons, stronger complexation is favored if the external field is weak, while it is disfavored in the high-σ_0 regime due to screening effects. Therefore, on the one

hand, the region in the (f, σ_0)-plane for which PE-stars adopt a jellyfish-type shape shrinks considerably for the benefit of anemone-like configurations. As discussed, the latter feature a tighter and much more stable binding to the substrate. On the other hand, the antenna domain grows at the expense of the starfish phase. Because of screening of the external field, it becomes much more difficult to reach the fully collapsed state for highly branched PE-stars. In particular, the critical value of the functionality above which starfish arrangements cannot be observed anymore decreases from $f \approx 50$ for system I to $f \approx 30$ for system II. Accordingly, for larger values of σ_0 the slopes of the phase boundaries are reduced considerably.

4.7 Surface charge dependence of the star radii

So far, we focused on the shapes of the complexes formed upon adsorption of PE-stars onto planar, charged substrates and their classification by morphological criteria, disregarding any quantitative description of the structures' spatial extent. Now, we turn our attention to a measurement of the PE-stars' typical, arm-averaged center-to-end radii as a function of the surface charge density [cf. also Eq. (2.22)]:

$$R_{\mathrm{s}}(f, \sigma_0) = \frac{1}{f} \left\langle \sum_{i=0}^{f-1} (\mathbf{r}_{i,N} - \mathbf{r}_{\mathrm{core}}) \right\rangle . \tag{4.19}$$

As depicted in Fig. 2.3, for PE-stars near neutral walls there is hardly any dependence of the radius $R_{\mathrm{s}} \equiv R_{\mathrm{s}}(\sigma_0 = 0)$ on the center-to-surface separation D. Due to the lack of any mutual attraction between individual monomers and the substrate, the conformations adopted by the star remain hemispherical even for closest proximity to the wall and there is no collapse taking place. The solid angle available for the spatial distribution of the arms is at worst halved compared to a free star, then effectively doubling the functionality. Since the chains are anyway fairly stretched because of the charges sitting along their backbones, for not too high arm numbers the f-dependence of the center-to-end radii is very weak and the resulting change in size is negligible.

In contrast, the presence of an external electric field does not only induce a monotonic decrease of the average distance $\langle D(f, \sigma_0) \rangle$ between the center of a PE-star and the lower wall (cf. Fig. 4.7), but also leads to a complexation as analyzed above in detail, accompanied by pronounced configurational changes. In particular, the gradual collapse culminating in starfish-like morphologies for high surface charge densities σ_0 causes a dramatic increase of the number of arms per occupied solid angle. For the purpose of placing more and more chains in a two-dimensional configuration onto the substrate one would expect an onward stretching and thus a noticeable growth of the arm-averaged center-to-end radius to be required due to steric and electrostatic inter-arm repulsions.

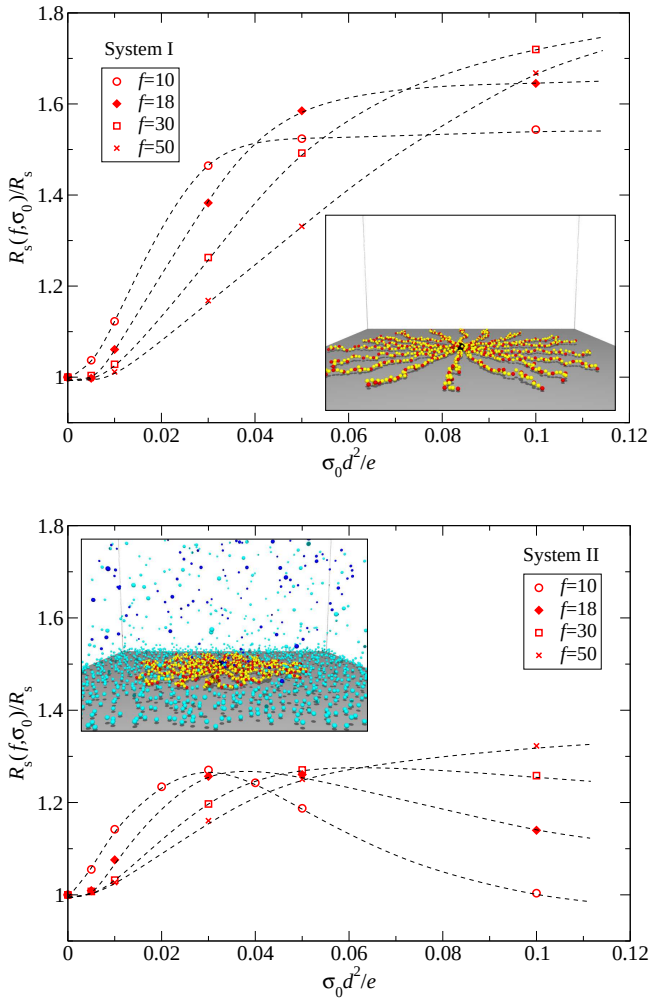

Figure 4.18: Relative radius $R_s(f, \sigma_0)/R_s$ of PE-stars of different functionality, plotted as a function of the surface charge density σ_0 for (a) system I and (b) system II. The black, dashed lines are guides to the eye. The respective insets show exemplary conformations for $f = 18$ and $\sigma_0 d^2/e = 0.1$, illustrating the strongly varying typical sizes.

Fig. 4.18(a) confirms this expectation for the capacitor-type geometry I. The relative radii $R_s(f, \sigma_0)/R_s$ grow as a function of the surface charge density σ_0, arriving at a plateau value once the starfish limit is reached. Then, there is no reason for a further stretching of the PE chains, since the configuration will not fundamentally change anymore even if we continuously step up the strength of the external field. For what values of σ_0 the saturation of the radii sets in crucially depends on the PE-star functionality. The higher f the larger surface charge densities are needed, in accordance with the morphological phase diagram shown in Fig. 4.16. The plateau value itself also rises as f grows, since it is much more difficult to place a larger number of chains in a two-dimensional arrangement. Compared to the situation without an applied external field, i.e., for $\sigma_0 = 0$, the PE-stars expand up to almost twice their original size when they are fully adsorbed to the wall.

In case of system II, the corresponding graphs exhibit a completely different, non-monotonic shape, as illustrated in Fig. 4.18(b). For weak external fields the radii grow analogously to the situation without additional wall counterions, but there is no saturation effect for the high-σ_0 regime. Instead, for a critical value of σ_0 sensitively depending on the functionality f of the PE-stars, the radii reach a maximum and shrink again upon a further increase of the surface charge density. The mechanism leading to such behavior is as follows. For very high values of σ_0, the resulting electric field in-between the walls is strong even though there is screening by the collapsed PE-star. Thus, it might be favorable to additionally bind a certain fraction of wall counterions to the lower plate since the gain in electrostatic energy over-compensates for the loss in entropy caused by the restriction of their mobility (compare Sec. 4.3 and, in particular, Fig. 4.4). All the positively charged ions close to the surface arrange in such a way that their mutual Coulombic repulsion is minimized, thereby the stretching of the PE-star's arms is reduced and its radius decreases. This phenomenon becomes more pronounced for stronger external fields or, equivalently, more wall counterions close to the surface. Clearly, for fixed charging fraction α the bare charge of a PE-star grows linearly with its functionality and consequently higher surface charge densities are needed to see the effect as f grows.

Finally, in order to clarify the differences in the typical PE-star configurations, the insets of Fig. 4.18(a) and (b) show exemplary simulation snapshots for setups I and II, respectively. In both cases, the functionality is $f = 18$ and the surface charge density was chosen to be $\sigma_0 d^2/e = 0.1$. The wall counterion-induced shrinking of the starfish-type complexes is obvious.

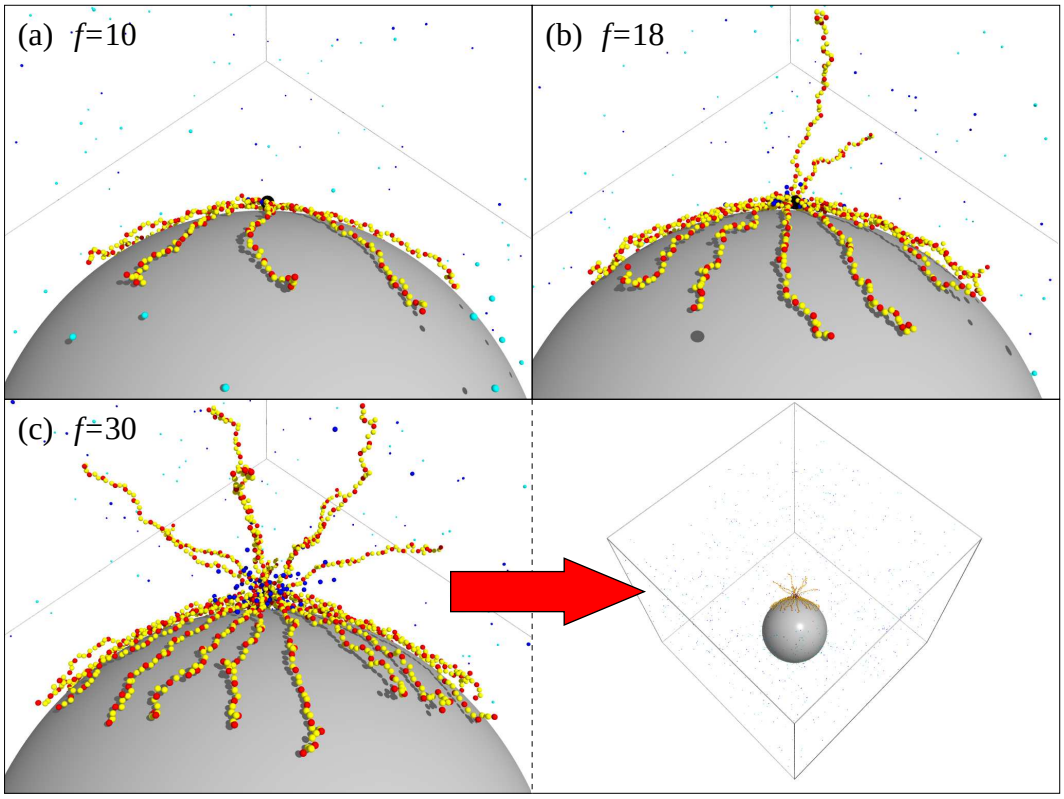

Figure 4.19: Exemplary simulation snapshots for PE-stars near a larger, charged colloid. The functionalities are (a) $f = 10$, (b) $f = 18$, and (c) $f = 30$. For all parameter combinations the size ratio is $q = 0.5$ and the colloid carries a total charge $Q_c/e = -700$. Obviously, the possible morphological states are similar to those observed for the case of planar, charged substrates.

4.8 Influence of wall curvature

The consequential next step is to take into account the influence of wall curvature, i.e., to study the adsorption of PE-stars to curved, charged substrates. As already stated in Sec. 4.2.2, a systematic and detailed investigation of PE-star–colloid complexation processes has just been initiated in the scope of this thesis and is subject of ongoing work. Here, we present exemplary results for selected sets of parameters in order to give an introductory overview of basic phenomena and general trends. In particular, we discuss differences emerging compared to the case of planar substrates and outline possible reasons for the same.

First of all, Fig. 4.19 shows representative MD snapshots for three different PE-star functionalities $f = 10, 18$ and 30, fixed size ratio $q = 0.5$ between the star and

the colloid, and fixed total charge of the colloid $Q_c/e = -700$. As manifest, we find a formation of PE-star–colloid 'bombs', induced by electrostatic attractions between the colloid and the oppositely charged monomer ions. In general, for not too small values of q, there is no obvious reason why the conformational phase behavior (with the terminology 'phase' used in the same sense as in Sec. 4.6) of the PE-stars should differ fundamentally from the case of planar substrates, and the found configurations indeed look very similar to morphologies observed in case of the planar systems I and II, respectively. Based on the snapshots, we may perform a first, qualitative classification of the resulting shapes of the PE-stars. Here, we have (a) starfish, (b) antenna, and (c) again antenna. In the latter case, there are considerably more arms sticking out and although clearly an antenna-type configuration, the state point thus seems to be located somewhat closer to a possible anemone–antenna crossover region.

Since there are both positively and negatively charged free ions present in the system, depicted in Fig. 4.19 as light blue and dark blue small spheres, respectively, it is reasonable to draw a comparison with system II. For this purpose, we firstly need to translate the total charge of the colloid to a corresponding surface charge density. As shown in Sec. 4.2.2, assuming all the Z_c elementary charges to sit onto the colloid's surface, we obtain a value of about $\sigma_0 d^2/e \approx 0.02$, depending on the actual functionality via the f-dependent PE-star radius. Pursuant to the morphological phase diagram in Fig. 4.17, for such surface charge density and $f = 10$ as well as $f = 18$ the morphological phases found for complexation at planar and curved surfaces agree. Indeed, for $f = 30$, we expect a PE-star near a flat substrate to be of mere anemone-type, in contrast to the findings of Fig. 4.19(c). The reason for this different attribution can easily be understood by geometrical arguments. Due to its curvature, there is less energetic punishment when placing a given number of PE chains onto the colloid's surface. Accordingly, a stronger adsorption compared to a planar substrate is favored. For fixed surface charge density more arms fold down and the binding of the star to the colloid is stronger.

4.8.1 Density profiles

Along the lines of Sec. 4.3, we measure one-particle density distributions of all the particle species, $\rho_\alpha(\mathbf{r})$ ($\alpha = \mathrm{m}, \mathrm{mi}, +, -$), with the origin of the coordinate system coinciding with the core position of the star. Due to the underlying geometry, we do not consider a representation with the x- and y-dependencies integrated out, but perform an alternative coarse-graining procedure. Thereby, we average over both the azimuthal and the polar angle, namely:

$$c_\alpha(r) = \int_0^{2\pi} \int_{-\pi/2}^{\pi/2} \mathrm{d}\phi \, \mathrm{d}\theta \, \sin\theta \, \rho_\alpha(\mathbf{r}). \tag{4.20}$$

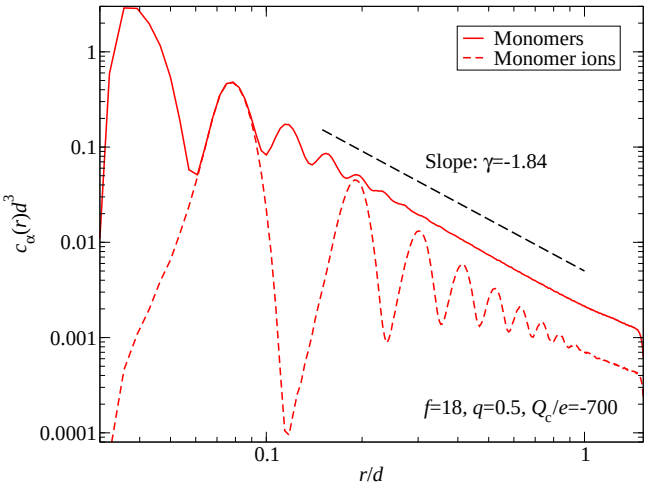

Figure 4.20: Double-logarithmic plot of the monomer and monomer ion density profiles $c_\alpha(r)$ ($\alpha = \mathrm{m}, \mathrm{mi}$) as a function of the distance r from the core position of the PE-star, exemplarily for a star with $f = 18$ arms, a colloid carrying the total charge $Q_\mathrm{c}/e = -700$, and a size ratio $q = 0.5$. The slope of the scaling regime is also shown (dashed line). The value $\gamma = -1.84$ evinces the stretching of the chains.

Even though the PE-stars are deformed upon complex formation, the rotational symmetry with respect to the axis connecting the relative centers of star and colloid is preserved. Moreover, a geometrical estimate easily shows that, provided the size ratio q is not too large and the chains are not too long, there is no significant difference in the center-to-end length of a fully adsorbed PE-chain and its respective contour length. Hence, the averaging does not bring about a significant loss in information. Again, a computation of $c_\alpha(r)$ during simulation runs is straightforward. Partitioning the system in shells of equal width Δr around the core of the star, calculating the average number of particles in each shell, and normalizing by dividing by the changing volume of the shells directly yields the desired result.

Fig. 4.20 illustrates such angle-averaged monomer and monomer ion density profiles for a PE-star with $f = 18$ arms, a colloid carrying $Z_\mathrm{c} = 700$ elementary charges $-e$, and a star-to-colloid size ratio $q = 0.5$. The axes are scaled in a double-logarithmic fashion. Clearly, both curves must resemble each other, since the monomer ions are distributed regularly along the backbones of the chains. The slope of the scaling regime is found to be $\gamma \approx -1.84$, reflecting the stretching of the arms. It is almost unchanged compared to the value $\cong -1.8$ for isolated PE-stars [32, 33, 109, 115–117], i.e., the presence of the colloid and the subsequent distortion of the PE-star's spatial arrangement does not bring about dramatic changes of the typical extension of individual arms.

Furthermore, distinct oscillations stand out, particularly in case of the monomer ion density profile, while for isolated PE-stars similar features can be found only to a minor degree. Such behavior results from the fact that the movement of a considerable fraction of PE-chains is obviously constrained to the colloidal surface by strong attractive electrostatic forces. Clearly, this trapping almost completely suppresses fluctuations of the discrete monomeric positions, and especially of the inter-monomer bond angles. These fluctuations would otherwise lead to a blurring of the density distributions, smearing out the oscillatory shape of the curves.

4.8.2 Configurational phase behavior

In order to quantitatively describe the morphological behavior of the complexes formed by a PE-star and an oppositely charged colloid of larger diameter, i.e., for a size ratio $q < 1$, we again need a convenient mathematical criterion. It must at the same time express both the equilibrium center-to-surface distance $\langle D(f, q, Q_\mathrm{c})\rangle$ and the typical orientations of all the individual PE-chains, labeled i, or more precisely speaking of their respective center-to-end vectors $\mathbf{R}_i$. We achieve this by appropriately modifying the criterion introduced in Sec. 4.6.1. Thereby, we have to take into account that, due to geometry, $\hat{\mathbf{z}}$ is not a preferred direction anymore. Instead, let

$$\hat{\mathbf{n}} = \frac{\mathbf{r}_\mathrm{core} - \mathbf{r}_\mathrm{c}}{|\mathbf{r}_\mathrm{core} - \mathbf{r}_\mathrm{c}|} \tag{4.21}$$

be a unit vector defining the axis instantaneously connecting the centers of PE-star, position vector $\mathbf{r}_\mathrm{core}$, and colloid, position vector $\mathbf{r}_\mathrm{c}$. Therewith, for each arm we calculate the time-averaged cosine of the enclosed angle θ_i' between $\mathbf{R}_i$ and $\hat{\mathbf{n}}$:

$$\langle \cos\theta_i' \rangle = \left\langle \frac{\mathbf{R}_i}{|\mathbf{R}_i|} \cdot \hat{\mathbf{n}} \right\rangle . \tag{4.22}$$

Note that the limiting plateau value for arms completely attached to the surface over their full length is in general not close to zero anymore, as it was for the case of planar substrates. On purely geometrical grounds, we obtain

$$\cos\theta_\mathrm{p}' = -\frac{R_\mathrm{s}(f, q, Q_\mathrm{c})}{2R_\mathrm{c}}, \tag{4.23}$$

whereby we already took into account that, because of the grafting to the core particle, an outright collapse of one or more PE-chains requires the center-to-surface distance of star and colloid to be small. Furthermore, we have to point out that $\cos\theta_\mathrm{p}'$ is not equal to half the size ratio $q/2$, since the relation $R_\mathrm{s}(f, q, Q_\mathrm{c}) \geq R_\mathrm{s}$ always holds. It rather depends on the set of parameters under consideration, i.e., it varies with f, q, and Q_c.

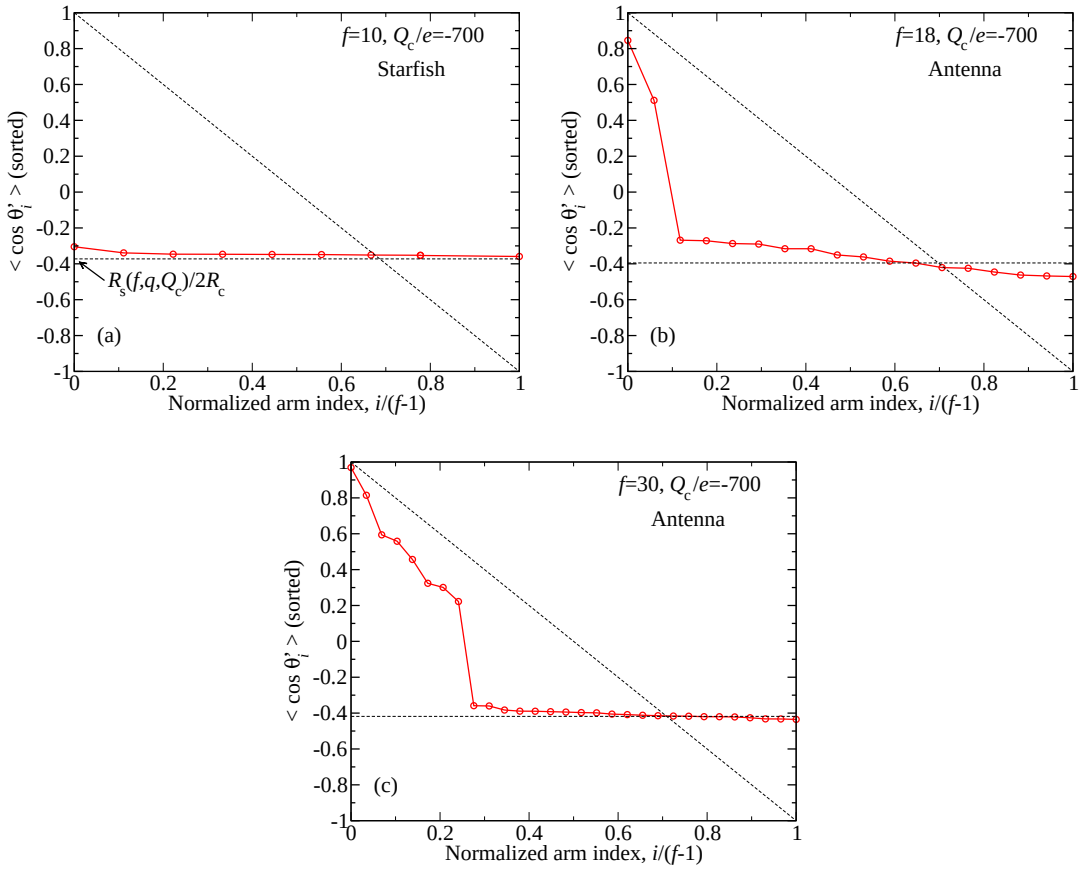

Figure 4.21: Illustration of the conveniently modified criterion to classify PE-star morphologies in case of complexation with an oppositely charged colloid of larger radius. For arms fully attached to the colloidal surface the plateau value reached deviates from zero and can be calculated by geometrical considerations. The exemplarily chosen parameter combinations are specified within the plots.

As before, we plot $\langle \cos \theta_i' \rangle$ in descending order as a function of the normalized arm index $i/(f-1)$, with the indices (re-)assigned accordingly. Fig. 4.21 depicts results obtained in this manner for the same parameters as already used in Fig. 4.19. Except for the baseline shift, the general shapes of the curves conform to analogous data for planar walls as shown in Figs. 4.12 to 4.14. Furthermore, they quantitatively confirm the above qualitative classification based on an inspection of exemplary snapshots. In this sense, the modified criterion indeed serves as a convenient tool to distinguish ensuing configurational phases when studying PE-star–colloid complex formation. In principle, by systematically scanning the (f, q, Q_c)-space and for each state point attributing the conformations to one of the possible morphological classes a corresponding phase diagram might be drawn. This will be the subject of future work.

4.9 Conclusions

We have investigated via extensive, monomer-resolved molecular dynamics (MD) simulations the complex formation of star-branched PE's and oppositely charged surfaces of different geometries. We analyzed in detail the complexation characteristics, the resulting morphological behavior, and, particularly, their dependence on physical parameters like the functionality of the PE-stars and the surface charge density.

For planar, charged substrates, we found a gradual collapse of the PE-stars upon increasing the strength of the external field or decreasing the functionality. Thereby, the PE-stars typically run through five distinct classes of morphologies, ranging from spherical arrangements with rather large center-to-wall distances to fully adsorbed starfish-type configurations. In the latter case, all the monomers are located in close proximity to the attracting wall and the PE-stars lose the ability to act as super-absorber for their counterions. Such behavior is in strong contrast to the case of PE-stars near neutral walls, whose properties are surprisingly robust against variation of the center-to-surface separation.

Transitions between different configurational states are continuous, featuring diffuse crossover regions. We developed convenient quantitative criteria, i.e., continuous order parameters, to reliably distinguish and classify the ensuing conformations. Thus, we were able to generate corresponding morphological phase diagrams by a systematic examination of the relevant parameter space. It emerged that one can indeed precisely steer the shape of the PE-stars. A closer study of the role of additionally included wall counterions revealed that there is in fact a noticeable, quantitative influence on the blurred phase boundaries, but no fundamental change in the basic trends. Moreover, the general behavior of the PE-stars was found to be stable against variation of the density (per unit surface area) of the PE-stars, at

least as long as sufficient dilution is guaranteed, rendering the system appropriate for technical applications like the use as microlens arrays or the tailoring of functional surface coatings.

For weakly curved surfaces, i.e., charged colloids of a size larger than the PE-star radius, we observed the constitution of 'bomb'-like complexes with the star sitting on the colloidal surface. We modified the morphological order parameter to fit the new situation, and exemplarily demonstrated its ability to characterize the configurational properties of the arising structures. In general, we expect curved substrates to favor a stronger adsorption compared to the case of planar walls. Thereby, the calculation of a full conformational phase diagram lies beyond the scope of this thesis and is subject of ongoing work.

Chapter 5

Conclusions and outlook

Within the realm of this thesis, we have investigated the influence of confinement on the conformations and the structural and phase behavior of star-branched polyelectrolytes (PE's), whereby we varied both the geometry of the confining walls and their surface properties. In general, we performed our studies by means of monomer-resolved molecular dynamics (MD) simulations, a theoretical mean-field approach, and liquid integral equation theory.

In chapter 2, we measured in our simulations and analyzed theoretically the repulsive forces exerted by flat, impenetrable, hard walls on multi-arm PE-stars. We found that the presence of the confining planes does not crucially affect the ability of the osmotic PE-stars to reabsorb the majority of the released counterions. Thus, the stars remain almost electroneutral. This holds even for very close proximity to the wall. Therefore, only a weakly populated counterion cloud emerges outside the spatial region occupied by a PE-star. For that reason, long-range contributions to the effective forces stemming from a distortion of the diffuse counterion layer are negligible and the total forces have a typical range of the order of the PE-star radius.

A detailed analysis of the mechanisms giving rise to the soft star–wall repulsions showed that, akin to the well-understood PE-star–PE-star case [32, 33], the functional form of the force-vs.-distance curves is mainly governed by the entropy of the absorbed counterions and the reduction of the volume available to them due to the star approaching the wall. But at the same time, we discovered a novel, additional mechanism to be at work. Due to the presence of neighboring arms, it can be favorable for a fraction of the stiff PE-chains to compress within a certain range of center-to-surface distances instead of bending away from the wall. This compression effect is a direct result of the impenetrable character of the wall. Clearly, such compression leads to an additional repulsive contribution to the total force. Only for PE-stars very close to the wall the compressed chains must 'slip away' to one side again and re-orient themselves. Consequentially, the compression process stops and the corresponding force contribution vanishes.

In chapter 3, we dealt with binary mixtures between PE-stars and neutral, spherical, hard colloids of much larger diameter than the stars. Based on our above findings for the effective interaction between PE-stars and planar walls, we put forward a Derjaguin-type approximation to calculate the effective PE-star–colloid cross-interaction, whereby the compression contribution turned out to decisively influence the resulting potential. Knowledge of the latter, together with corresponding intra-species interaction potentials as known from the literature [32, 33, 36, 54], then allows for a mesoscopic description of the two-component mixture by dint of an integral equation theory approach, yielding information on structure and thermodynamics of the system. As we could verify, the cross-interaction obtained here is sufficiently repulsive to bring about regions of a fluid–fluid demixing instability. This macroscopic phase separation can be understood by the occurrence of depletion effects and corresponding effective potentials between the colloids in an one-component description, featuring attractive tails which are induced by the presence of PE-stars in the mixture. These potentials are very similar to the effective colloid–colloid depletion interactions encountered in colloid–polymer mixtures [137].

In chapter 4, we have changed the properties of the confining walls drastically and introduced surface charges of opposite sign with respect to the PE-stars. The emanating electric fields induce an adsorption of the PE's to the substrates and thus the formation of complexes. Thereby, we investigated in detail the characteristics of such complexation processes and the resulting morphological behavior of the PE-stars via MD simulations. In particular, we studied the stability of the arising configurations, their dependence on externally controllable physical parameters like the functionality of the PE-stars and the surface charge density, and how sharp the necessarily continuous crossovers between different morphological states are. In order to rationalize the configurational phases (with the terminology used in the sense of Sec. 4.6) and the corresponding crossovers, we developed quantitative morphological criteria appropriate to distinguish and classify the ensuing conformations.

In case of planar charged walls, when increasing the external electric field or, for fixed surface charge density σ_0, decreasing the functionality f, the PE-stars undergo a gradual collapse. This ranges from almost spherical arrangements for low values of the surface charge density and high arm numbers to completely flat, two-dimensional, starfish-type configurations in the opposite limit. In-between these two extreme states we were able to identify three additional and well-discriminable intermediate classes of morphologies. In this sense, the complexation process is very much different from that for linear PE-chains, where no such intermediate states can be found [165]. We showed that, if we approach regions in (f, σ_0)-space where a fully collapsed situation is reached, the average center-to-surface separation decreases, fluctuations of the same diminish almost completely, and the binding of the stars to the substrate becomes more and more stable. In addition, the PE-stars were found to lose the ability to act as super-absorbers for their counterions.

This particular behavior is in strong contrast to the above case of PE-stars near neutral walls, where the properties of the PE-stars are surprisingly robust against variation of the center-to-surface separation. By systematically scanning the relevant parameter space we generated morphological phase diagrams and it emerged that one can indeed precisely and easily steer the shape of the PE-stars. Thereby, we demonstrated that the addition of freely moving wall counterions to the solution or the variation of the PE-star density can lead to noticeable, quantitative changes in the location of the diffuse state boundaries, but the fundamental trends persist. This renders the system convenient for several possible applications, e.g., the use as microlens arrays or the design and tailoring of specialized surface coatings [91–94].

For PE-stars in the vicinity of charged colloids with a size larger than the star radius (similar to chapter 3), we also observed an adsorption to the weakly curved surface, resulting in 'bomb'-like compounds. We exemplarily substantiated the applicability of the conveniently modified morphological criteria in this case, but a calculation of the full conformational phase diagram lies beyond the scope of this thesis and is subject of ongoing work. Nevertheless, we want to point out again that the available data, as in case of planar substrates, suggest an adsorption process and ensuing morphologies very different from that for linear PE-chains [165].

Besides completing systematic studies of the morphological behavior of PE-stars near larger colloids carrying opposite charges, there are several other possible directions of research arising through and motivated by the thesis at hand. As far as binary PE-star–colloid mixtures are concerned, the specific form of the cross-interaction can in general be expected to distinctly determine the structure of the mixture and its stability. It might be possible to enforce micro-phase separation with finite wavelength, i.e., cluster formation, instead of macroscopic phase separation by suitably tuning it. In this respect, a detailed investigation of the effective forces between a PE-star and an oppositely charged colloid seems to be promising. Moreover, for both planar and curved, charged substrates, it is an evident question what influence salt might have on the complexation phenomena found in chapter 4, since a strong screening of the electric fields due to additional ions can be expected to hinder a collapse of the PE-stars. A related problem is the investigation of the effects of multivalent counterions instead of monovalent ones, as was assumed within the framework of our considerations. Another issue that has already attracted attention in the colloid–PE-chain context and which is also interesting in our case is that of charge inversion, also termed overcharging of the colloid due to the associating PE [60–63]. For PE-stars with a total charge smaller than that carried by a colloid this requires the formation of multi-complexes, i.e., a situation where more than one star is adsorbed to the colloid. Such multi-complexes are also interesting from a morphological point of view, not only against the background of charge inversion. And finally, since we have only regarded static properties up to now, a promising field of analysis are the coagulation kinetics for the wall–PE-star or colloid–PE-star

complexation processes. In the past, a great deal of work was already devoted to this topic for other systems of oppositely charged particles [165, 170].

Appendix A

Calculation of the electrostatic potential $\Phi_{\rm in}$

Consider a sphere of radius $R_{\rm s}$, with a spherical cap chopped off at a plane perpendicular to the z-axis and a distance D away from the center. The latter is at the same time taken to be the origin O of the coordinate axes. This chopped sphere of total volume $\Omega_{\rm in}$ is assumed to carry a total net charge $Q_{\rm s}$, whereby the charge density $\varrho_{\rm in}(\mathbf{r}')$ decays as $(r')^{-2}$ with the separation r' from midpoint and is instantly cut-off at the borders. As shown in the main text, a simple normalization condition yields

$$\varrho_{\rm in}(r') = \frac{Q_{\rm s}}{2\pi R_{\rm s}(r')^2}\left\{1+\frac{D}{R_{\rm s}}\left[1-\log\left(\frac{D}{R_{\rm s}}\right)\right]\right\}^{-1}, \tag{A.1}$$

i.e., the charge density and all deduced quantities depend on the geometry through $\cos\theta_0 = D/R_{\rm s}$. In chapter 2, we briefly outlined the procedure used to obtain the corresponding electrostatic potential $\Phi_{\rm in}(\mathbf{r})$ [see Eq. (2.14)], now we explicitly show the technical details for the calculation, akin to derivations put forward in Ref. [33] for a very similar problem. Fig. A.1 sketches the geometry at hand and introduces some notation used in what follows.

In general, the electrostatic potential $\Phi(\mathbf{r})$ due to a charge density $\varrho(\mathbf{r})$ in a dielectric medium of permittivity ϵ is given by the expression

$$\Phi(\mathbf{r}) = \frac{1}{\epsilon}\int \mathrm{d}^3r'\,\frac{\varrho(\mathbf{r}')}{|\mathbf{r}'-\mathbf{r}|}. \tag{A.2}$$

In order to perform the above integration for a chopped sphere, we follow a *divide and conquer* paradigm and firstly decompose the sphere in a succession of infinitesimally thin discs (height $\mathrm{d}z'$) perpendicular to the z-axis and with their respective centers $C = (x', y', z')$ located along the same. Clearly, the radius a of one such disc depends

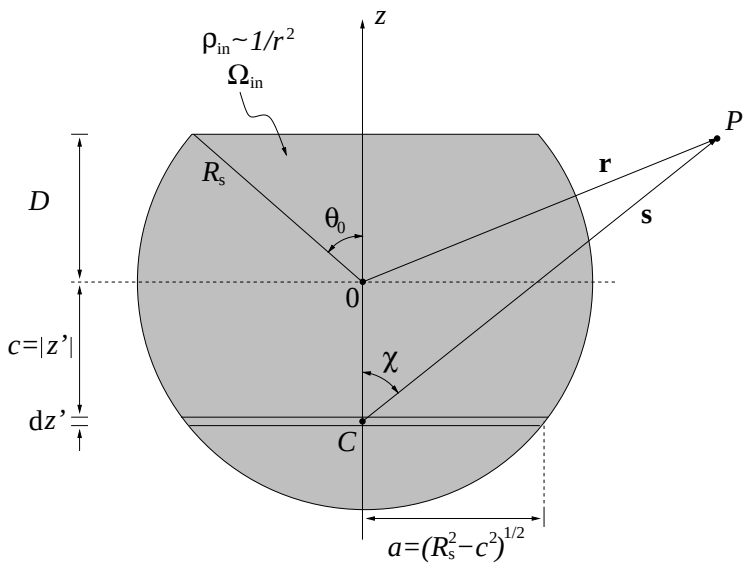

Figure A.1: Sketch of a chopped sphere, illustrating the basic geometry and the procedure used to calculate of the electrostatic potential $\Phi_{\mathrm{in}}(\mathbf{r})$.

on its distance $c = |z'|$ with respect to the point O and reads as

$$a = \left(R_{\mathrm{s}}^2 - c^2\right)^{1/2}. \tag{A.3}$$

Each such disc carries an elementary charge $\mathrm{d}Q_{\mathrm{disc}}(z')$, which by straight-forward computations can be proven to have a value

$$\mathrm{d}Q_{\mathrm{disc}}(z') = \frac{Q_{\mathrm{s}}}{R_{\mathrm{s}}} \log\left(\frac{R_{\mathrm{s}}}{c}\right) \left\{1 + \frac{D}{R_{\mathrm{s}}}\left[1 - \log\left(\frac{D}{R_{\mathrm{s}}}\right)\right]\right\}^{-1} \mathrm{d}z'. \tag{A.4}$$

The contribution $\mathrm{d}\Phi_{\mathrm{disc}}(\mathbf{r}; z')$ of one disc to the electrostatic potential at a point P thus also depends parametrically on the disc center location z'. Employing cylindrical coordinates $\mathbf{r} = (\rho, \phi, z)$ and due to azimuthal symmetry, we have

$$\mathrm{d}\Phi_{\mathrm{disc}}(\mathbf{r}; z') = \mathrm{d}\Phi_{\mathrm{disc}}(\rho, z; z'). \tag{A.5}$$

For the steps to come, it is convenient to translate the sought-for potential to a shifted system of coordinates with the origin O' and the disc center C coinciding. We introduce the vector $\mathbf{s} = (\rho, \phi, z - z')$ connecting C and the observation point P; its magnitude is obviously related to the original coordinates by

$$s = \left[\rho^2 + (z - z')^2\right]^{1/2}. \tag{A.6}$$

Consequently, the cosine of the angle χ enclosed by the z-axis and the vector $\mathbf{s}$ is

$$\cos\chi = \frac{z - z'}{s} = \frac{z - z'}{\left[\rho^2 + (z - z')^2\right]^{1/2}}. \tag{A.7}$$

Therewith, denoting the function which expresses the potential $\mathrm{d}\Phi_{\mathrm{disc}}$ in the new system of axes as $\mathrm{d}\Psi$, we may write:

$$\mathrm{d}\Phi_{\mathrm{disc}}(\rho, z; z') = \mathrm{d}\Psi(s, \chi; z'). \tag{A.8}$$

As we will see, $\mathrm{d}\Psi(s, \chi; z')$ can be obtained analytically for each disc following from its further decomposition into concentric rings with radius ξ and charge $\mathrm{d}q(\xi; z')$ centered at point C. Note that, due to the inhomogeneous charge density $\sim (r')^{-2}$ inside the chopped sphere all the discs also have inhomogeneous charge densities as a function of ξ themselves, namely

$$\varrho_{\mathrm{disc}}(\xi; z') = \frac{\mathrm{d}Q_{\mathrm{disc}}(z')}{\pi} \frac{1}{\xi^2 + c^2} \left\{ \log \left[1 + \left(\frac{a}{c} \right)^2 \right] \right\}^{-1}. \tag{A.9}$$

Consequently, the charge carried by a ring with radius ξ results as

$$\mathrm{d}q(\xi; z') = \frac{2\,\mathrm{d}Q_{\mathrm{disc}}(z')\,\xi}{\xi^2 + c^2} \left\{ \log \left[1 + \left(\frac{a}{c} \right)^2 \right] \right\}^{-1} \mathrm{d}\xi. \tag{A.10}$$

In general, the electrostatic potential of a charged ring is known from literature [119, 120]. For our special case and the geometry at hand it can be written as

$$\mathrm{d}\phi_{\mathrm{ring}}(s, \chi; \xi; z') = \begin{cases} \mathrm{d}\phi^{<}_{\mathrm{ring}}(s, \chi; \xi; z') & s < \xi \\ \mathrm{d}\phi^{>}_{\mathrm{ring}}(s, \chi; \xi; z') & s > \xi. \end{cases} \tag{A.11}$$

Thereby, with $P_m(x)$ being the Legendre polynomial of order m and taking into account the relation $P_{2k+1}(0) = 0$, the term $\mathrm{d}\phi^{<}_{\mathrm{ring}}(s, \chi; \xi; z')$ is then given by

$$\begin{aligned} \mathrm{d}\phi^{<}_{\mathrm{ring}}(s, \chi; \xi; z') = & \frac{2\,\mathrm{d}Q_{\mathrm{disc}}(z')\,\mathrm{d}\xi}{\epsilon} \left\{ \log \left[1 + \left(\frac{a}{c} \right)^2 \right] \right\}^{-1} \\ & \times \left\{ \sum_{k=0}^{\infty} P_{2k}(0) P_{2k}(\cos\chi) \frac{s^{2k}}{\xi^{2k}\,(\xi^2 + c^2)} \right\}. \end{aligned} \tag{A.12}$$

Analogously, we receive for $\mathrm{d}\phi^{>}_{\mathrm{ring}}(s, \chi; \xi; z')$ the expression

$$\begin{aligned} \mathrm{d}\phi^{>}_{\mathrm{ring}}(s, \chi; \xi; z') = & \frac{2\,\mathrm{d}Q_{\mathrm{disc}}(z')\,\mathrm{d}\xi}{\epsilon} \left\{ \log \left[1 + \left(\frac{a}{c} \right)^2 \right] \right\}^{-1} \\ & \times \left\{ \sum_{k=0}^{\infty} P_{2k}(0) P_{2k}(\cos\chi) \frac{1}{s^{2k+1}} \frac{\xi^{2k+1}}{(\xi^2 + c^2)} \right\}. \end{aligned} \tag{A.13}$$

Using Eqs. (A.11) to (A.13), an integration over all the corresponding rings, i.e., from $\xi = 0$ to $\xi = a$, directly yields the desired function $\mathrm{d}\Psi(s, \chi; z')$:

$$\mathrm{d}\Psi(s, \chi; z') = \int_{\xi=0}^{\xi=a} \mathrm{d}\phi_{\mathrm{ring}}(s, \chi; \xi; z'). \tag{A.14}$$

Again, we get a split definition and the resulting potential is

$$\mathrm{d}\Psi(s, \chi; z') = \begin{cases} \mathrm{d}\Psi^{<}(s, \chi; z') & s < a \\ \mathrm{d}\Psi^{>}(s, \chi; z') & s > a, \end{cases} \tag{A.15}$$

with the two different parts reading as

$$\begin{aligned} \mathrm{d}\Psi^{<}(s, \chi; z') =& \frac{2\,\mathrm{d}Q_{\mathrm{disc}}(z')}{\epsilon c} \left\{ \log\left[1 + \left(\frac{a}{c}\right)^2\right]\right\}^{-1} \\ & \times \left\{ \sum_{k=0}^{\infty} P_{2k}(0) P_{2k}(\cos\chi) A_k^{<}(s; z') \right\} \end{aligned} \tag{A.16}$$

and, accordingly,

$$\begin{aligned} \mathrm{d}\Psi^{>}(s, \chi; z') =& \frac{2\,\mathrm{d}Q_{\mathrm{disc}}(z')}{\epsilon c} \left\{ \log\left[1 + \left(\frac{a}{c}\right)^2\right]\right\}^{-1} \\ & \times \left\{ \sum_{k=0}^{\infty} P_{2k}(0) P_{2k}(\cos\chi) A_k^{>}(s; z') \right\}. \end{aligned} \tag{A.17}$$

Here, we introduced the short hand notation

$$A_k^{<}(s; z') = C_k(s; z') \left(\frac{c}{s}\right)^{2k+1}; \tag{A.18}$$

$$A_k^{>}(s; z') = C_k(s; z') \left(\frac{c}{s}\right)^{2k+1} + D_k(s; z') \left(\frac{s}{c}\right)^{2k}, \tag{A.19}$$

with the additional abbreviations

$$C_k(s; z') = \frac{(-1)^k}{2} \log\left[1 + \left(\frac{a}{c}\right)^2\right] + \sum_{j=1}^{k} \frac{(-1)^{k+j}}{2j} \left(\frac{a}{c}\right)^{2j}; \tag{A.20}$$

$$\begin{aligned} D_k(s; z') =& (-1)^k \left[\arctan\left(\frac{a}{c}\right) - \arctan\left(\frac{s}{c}\right)\right] \\ & - \sum_{j=1}^{k} \frac{(-1)^{j+k}}{2j-1} \left[\left(\frac{a}{c}\right)^{1-2j} - \left(\frac{s}{c}\right)^{1-2j}\right]. \end{aligned} \tag{A.21}$$

Based on the above findings, the total potential $\Phi_{\text{in}}(\mathbf{r})$ caused by the chopped sphere at an arbitrary observation point P can obtained by carrying out a z'-integration in the following fashion:

$$\Phi_{\text{in}}(\mathbf{r}) = \int_{z'=-R_{\text{s}}}^{z'=D} \mathrm{d}\Psi\left(s;\chi;z'\right). \tag{A.22}$$

This integral cannot be calculated analytically and we thus have to employ an one-dimensional numerical integration scheme instead. For this purpose, we need to rewrite all k- and j-sums in Eqs. (A.15) to (A.21) in such a way that they become manifestly convergent. More precisely speaking, the functions $A_k^{<}(s;z')$ and $A_k^{>}(s;z')$ defined in Eqs. (A.18) and (A.19), respectively, have to be expressed in terms of new variables $x<1$ raised to positive powers in order to gain formulas suitable for the numerical integration. Thereby, it is necessary to expand, depending on whether we have $s<c$ or $s>c$, the logarithmic or the inverse tangent functions. The corresponding results are given below.

Case I: $c<a<s$.

$$A_k^{>}(s;z') = E_k(s;z') + F_k(s;z'), \tag{A.23}$$

where

$$E_k(s;z') = \frac{(-1)^k}{2}\log\left[1+\left(\frac{a}{c}\right)^2\right]\left(\frac{s}{c}\right)^{2k+1}; \tag{A.24}$$

$$F_k(s;z') = \sum_{j=1}^{k}\frac{(-1)^{j+k}}{2j}\left(\frac{c}{a}\right)^{2(k-j)+1}\left(\frac{a}{s}\right)^{2k+1}. \tag{A.25}$$

Case II: $c<s<a$.

$$A_k^{<}(s;z') = G_k(s;z') + H_k(s;z') + I_k(s;z'), \tag{A.26}$$

where

$$G_k(s;z') = \frac{(-1)^k}{2}\log\left[1+\left(\frac{s}{c}\right)^2\right]\left(\frac{s}{c}\right)^{2k+1}; \tag{A.27}$$

$$H_k(s;z') = \sum_{j=1}^{k}\frac{(-1)^{j+k}}{2j}\left(\frac{c}{s}\right)^{2(k-j)+1}; \tag{A.28}$$

$$I_k(s;z') = \sum_{j=k+1}^{\infty}\frac{(-1)^{k+j}}{2j-1}\left(\frac{c}{s}\right)^{2(j-k)-1}\left[\left(\frac{s}{a}\right)^{2j-1}-1\right]. \tag{A.29}$$

Case III: $s < c < a$ or $s < a < c$.

$$A_k^<(s;z') = J_k(s;z') + K_k(s;z') + L_k(s;z'), \tag{A.30}$$

where

$$J_k(s;z') = \sum_{j=k+1}^{\infty} \frac{(-1)^{j+k+1}}{2j} \left(\frac{s}{c}\right)^{2(j-k)-1}; \tag{A.31}$$

$$K_k(s;z') = (-1)^k \left(\frac{s}{c}\right)^{2k} \left[\arctan\left(\frac{a}{c}\right) - \arctan\left(\frac{s}{c}\right)\right]; \tag{A.32}$$

$$L_k(s;z') = \sum_{j=1}^{k} \frac{(-1)^{j+k+1}}{2j-1} \left(\frac{s}{c}\right)^{2(k-j)+1} \left[\left(\frac{s}{a}\right)^{2j-1} - 1\right]. \tag{A.33}$$

Case IV: $a < s < c$.

$$A_k^>(s;z') = M_k(s;z'), \tag{A.34}$$

where

$$M_k(s;z') = \sum_{j=k+1}^{\infty} \frac{(-1)^{j+k+1}}{2j} \left(\frac{a}{s}\right)^{2j} \left(\frac{s}{c}\right)^{2(j-k)-1}. \tag{A.35}$$

Case V: $a < c < s$. For this special case, we can directly use the result for $A^>(s,\chi;z')$ as given in Eq. (A.19), since the fractions a/c and c/s appearing in the sums are already smaller than unity and there is no additional rewriting necessary.

Appendix B

Calculation of the electrostatic potential Φ_{out}

Consider a hollow sphere of inner radius R_{s} and outer radius R_{W}, with a spherical cap chopped off at a plane perpendicular to the z-axis and a distance D away from the center O. This spherical shell of volume Ω_{out} is assumed to carry an uniform charge density, i.e.,

$$\varrho_{\mathrm{out}}(\mathbf{r}') = \begin{cases} \varrho_{\mathrm{out}} & \mathbf{r}' \in \Omega_{\mathrm{out}} \\ 0 & \mathbf{r}' \notin \Omega_{\mathrm{out}}. \end{cases} \tag{B.1}$$

In order to calculate the corresponding potential $\Phi_{\mathrm{out}}(\mathbf{r})$ [cf. Eq. (2.14)], we can make use of the superposition principle in the following fashion. As shown in Fig. B.1, the hollow region can be apprehended from the electrostatic point of view as the superposition of two solid chopped spheres with radii R_{s} and R_{W} and uniform charge densities $\varrho_{\mathrm{in}} = -\varrho_{\mathrm{out}}$ and ϱ_{out}, respectively. The resulting effective charge density then exactly equals the initial one given by Eq. (B.1). By this means, the problem is reduced to the calculation of the electrostatic potential of a chopped sphere with a homogeneous distribution of charges. This task can be solved easily using the method presented in Appendix A for the somewhat more involved case of an inhomogeneous charge density $\sim (r')^2$. The electrostatic potential $d\Phi_{\mathrm{disc}}(\mathbf{r}; z')$ of one of the discs the sphere is fractionalized into is in principle still obtained in exactly the same way, we simply need to replace Eqs. (A.4), (A.10), (A.16), and (A.17) by their respective counterparts valid for constant charge densities.

When regarding a chopped sphere of radius R_{s} carrying a total net charge Q_{s}, the expression for the charge $\mathrm{d}Q_{\mathrm{disc}}(z')$ of a cut-out disc with radius $a = (R_{\mathrm{s}}^2 - c^2)^{1/2}$ follows from elementary calculations and reads as

$$\mathrm{d}Q_{\mathrm{disc}}(z') = \frac{3Q_{\mathrm{s}}a^2}{4R_{\mathrm{s}}^3} \left\{ \frac{1}{2} + \frac{3}{4}\left(\frac{D}{R_{\mathrm{s}}}\right) - \frac{1}{4}\left(\frac{D}{R_{\mathrm{s}}}\right)^3 \right\}^{-1} \mathrm{d}z'. \tag{B.2}$$

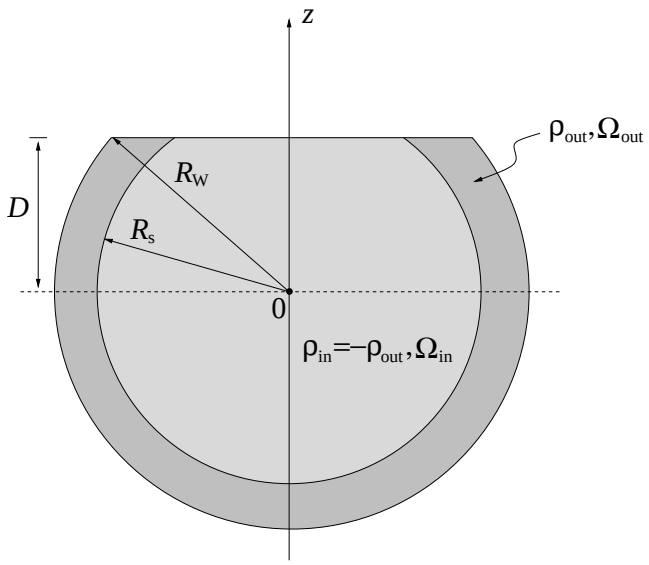

Figure B.1: Sketch of two superimposed chopped spheres. When choosing their respective uniform charge densities as $\varrho_{\mathrm{in}} = -\varrho_{\mathrm{out}}$ and ϱ_{out}, the total electrostatic potential is that of a hollow chopped sphere with a homogeneous charge density ϱ_{out}.

Accordingly, when decomposing such disc in concentric rings of radius ξ, each of them is charged by an amount $\mathrm{d}q(\xi; z')$. Here, we obtain

$$\mathrm{d}q(\xi; z') = \frac{2\xi\, \mathrm{d}Q_{\mathrm{disc}}(z')}{a^2}\mathrm{d}\xi. \tag{B.3}$$

Therewith, we then receive for the sought-for potential $\mathrm{d}\Psi(s, \chi; z')$

$$\begin{aligned}\mathrm{d}\Psi^{<}(s, \chi; z') =& \frac{2\,\mathrm{d}Q_{\mathrm{disc}}(z')}{\epsilon a}\sum_{k=0}^{\infty} P_{2k}(0)P_{2k}(\cos\chi) \\ & \times\left\{\frac{4k+1}{2(k+1)(2k-1)}\left(\frac{s}{a}\right) - \frac{1}{2k-1}\left(\frac{s}{a}\right)^{2k}\right\}\end{aligned} \tag{B.4}$$

and

$$\mathrm{d}\Psi^{<}(s, \chi; z') = \frac{2\,\mathrm{d}Q_{\mathrm{disc}}(z')}{\epsilon s}\sum_{k=0}^{\infty}\frac{P_{2k}(0)P_{2k}(\cos\chi)}{2(k+1)}\left(\frac{a}{s}\right)^{2k}. \tag{B.5}$$

There is no need for a supplementary rewriting of the above formulas (B.4) and (B.5), since the convergence of all the sums is obvious. The simple substitution $R_{\mathrm{s}} \to R_{\mathrm{W}}$ directly yields the result for a chopped sphere of radius R_{W}.

Bibliography

[1] R. J. Hunter, *Foundations of Colloid Science* (Clarendon Press, Oxford, 1987).

[2] S. A. Safran and N. A. Clark, editors, *Physics of Complex and Supermolecular Fluids* (Whiley Interscience, New York, 1987).

[3] W. B. Russel, D. A. Saville, and W. R. Schowalter, *Colloidal dispersions* (Cambridge University Press, Cambridge, 1989).

[4] C. N. Likos, Phys. Rep. **348**, 267 (2001).

[5] T. A. Witten, Rev. Mod. Phys. **71**, S367 (1999).

[6] G. Riess, Prog. Polym. Sci. **28**, 1107 (2003).

[7] S. R. Bhatia, A. Mourchid, and M. Joanicot, Curr. Opin. Colloid Interface Sci. **6**, 471 (2001).

[8] Y. Kakizawa and K. Kataoka, Adv. Drug. Deliv. Rev. **54**, 203 (2002).

[9] P. M. Biesheuvel and A. Wittemann, J. Phys. Chem. **109**, 4209 (2005).

[10] L. D. Landau and E. M. Lifshitz, *Course of Theoretical Physics: Statistical Physics*, 3rd ed. (Pergamon Press, Oxford, 1980).

[11] A. Y. Grosberg and A. R. Khokhlov, *Statistical Physics of Macromolecules* (American Institute of Physics Press, New York, 1994).

[12] M. P. Allen and D. J. Tildesley, *Computer Simulation of Liquids* (Oxford University Press, Oxford, 1987).

[13] D. Frenkel and B. Smit, *Understanding Molecular Simulation* (Academic Press, San Diego, 1996).

[14] D. C. Rapaport, *The Art of Molecular Dynamics Simulation* (Cambridge University Press, Cambridge, 1995).

[15] W. G. McMillan and J. E. Mayer, J. Chem. Phys. **13**, 276 (1945).

[16] J. G. Kirkwood and F. P. Buff, J. Chem. Phys. **19**, 774 (1951).

[17] J. K. G. Dhont, *An Introduction to Dynamics of Colloids* (Elsevier, Amsterdam, 1996).

[18] G. S. Grest, L. J. Fetters, J. S. Huang, and D. Richter, Adv. Chem. Phys. **XCIV**, 67 (1996).

[19] M. Daoud and J. P. Cotton, J. Phys. (Paris) **43**, 531 (1982).

[20] T. A. Witten and P. A. Pincus, Macromolecules **19**, 2509 (1986).

[21] C. N. Likos, H. Löwen, M. Watzlawek, B. Abbas, O. J. J. Allgaier, and D. Richter, Phys. Rev. Lett. **80**, 4450 (1998).

[22] A. Jusufi, M. Watzlawek, and H. Löwen, Macromolecules **32**, 4470 (1999).

[23] M. Laurati, J. Stellbrink, R. Lund, D. Richter, and E. Zaccarelli, Phys. Rev. Lett. **94**, 195504 (2005).

[24] M. Watzlawek, *Phase Behavior of Star Polymers* (Shaker Verlag, Aachen, 2002).

[25] F. Oosawa, *Polyelectrolytes* (Marcel Dekker Inc., New York, 1971).

[26] P. Pincus, Macromolecules **24**, 2912 (1991).

[27] J. K. Wolterink, J. van Male, M. A. C. Stuart, L. K. Koopal, E. B. Zhulina, and O. V. Borisov, Macromolecules **35**, 9176 (2002).

[28] J. K. Wolterink, F. A. M. Leermakers, G. J. Fleer, L. K. Koopal, E. B. Zhulina, and O. V. Borisov, Macromolecules **32**, 2365 (1999).

[29] O. V. Borisov and E. B. Zhulina, J. Phys. II (Paris) **7**, 449 (1997).

[30] O. V. Borisov and E. B. Zhulina, Eur. Phys. J. B **4**, 205 (1998).

[31] N. P. Shusharina, P. Linse, and A. R. Khokhlov, Macromolecules **33**, 3892 (2000).

[32] A. Jusufi, C. N. Likos, and H. Löwen, Phys. Rev. Lett. **88**, 018301 (2002).

[33] A. Jusufi, C. N. Likos, and H. Löwen, J. Chem. Phys. **116**, 11011 (2002).

[34] A. R. Denton, Phys. Rev. E **67**, 011804(E) (2003).

[35] H. Wang and A. R. Denton, Phys. Rev. E **70**, 041404 (2004).

[36] N. Hoffmann, C. N. Likos, and H. Löwen, J. Chem. Phys. **121**, 7009 (2004).

[37] A. Jusufi, C. N. Likos, and M. Ballauff, Colloid Polym. Sci. **282**, 910 (2004).

[38] M. Roger, P. Guenoun, F. Muller, L. Belloni, and M. Delsanti, Eur. Phys. J. E **9**, 313 (2002).

[39] O. V. Borisov and E. B. Zhulina, Macromolecules **35**, 4472 (2002).

[40] E. B. Zhulina and O. V. Borisov, Macromolecules **35**, 9191 (2002).

[41] O. V. Borisov and E. B. Zhulina, Macromolecules **36**, 10029 (2003).

[42] A. Jusufi, J. Chem. Phys. **124**, 044908 (2006).

[43] P. Guenoun, F. Muller, M. Delsanti, L. Auvray, Y. J. Chen, J. W. Mays, and M. Tirrell, Phys. Rev. Lett. **81**, 3872 (1998).

[44] W. Groenewegen, S. U. Egelhaaf, A. Lapp, and J. R. C. van der Maarel, Macromolecules **33**, 3283 (2000).

[45] W. Groenewegen, A. Lapp, S. U. Egelhaaf, and J. R. C. van der Maarel, Macromolecules **33**, 4080 (2000).

[46] J. R. C. van der Maarel, W. Groenewegen, S. U. Egelhaaf, and A. Lapp, Langmuir **16**, 7510 (2000).

[47] T. Abraham, S. Giasson, J. F. Gohy, and R. Jérôme, Langmuir **16**, 4286 (2000).

[48] Q. de Robillard, X. Guo, M. Ballauff, and T. Narayanan, Macromolecules **33**, 9109 (2000).

[49] X. Guo and M. Ballauff, Phys. Rev. E **64**, 051406 (2001).

[50] N. Dingenouts, R. Merkle, X. Guo, T. Narayan, G. Goerick, and M. Ballauff, J. Appl. Crystallogr. **36**, 578 (2003).

[51] M. Heinrich, M. Rawiso, J. G. Zilliox, P. Lesieur, and J. P. Simon, Eur. Phys. J. E **4**, 131 (2001).

[52] A. V. Korobko, W. Jesse, S. U. Egelhaaf, A. Lapp, and J. R. C. van der Maarel, Phys. Rev. Lett. **93**, 177801 (2005).

[53] O. V. Borisov and E. B. Zhulina, Eur. Phys. J. E **4**, 205 (1998).

[54] C. N. Likos, N. Hoffmann, A. Jusufi, and H. Löwen, J. Phys.: Condens. Matter **15**, S233 (2003).

[55] T. Furukawa and K. Ishizu, Macromolecules **38**, 2911 (2005).

[56] D. Gottwald, C. N. Likos, G. Kahl, and H. Löwen, Phys. Rev. Lett. **92**, 068301 (2004).

[57] D. Gottwald, C. N. Likos, G. Kahl, and H. Löwen, J. Chem. Phys. **122**, 074903 (2005).

[58] J. Kleimann, C. Gehin-Delval, H. Auweter, and M. Borkovec, Langmuir **21**, 3688 (2005).

[59] E. Gurovitch and P. Sens, Phys. Rev. Lett. **82**, 339 (1999).

[60] E. M. Mateescu, C. Jeppesen, and P. Pincus, Europhys. Lett. **46**, 493 (1999).

[61] S. Y. Park, R. F. Bruinsma, and W. M. Gelbart, Europhys. Lett. **46**, 454 (1999).

[62] T. T. Nguyen and B. I. Shklovskii, J. Chem. Phys. **114**, 5905 (2001).

[63] T. T. Nguyen and B. I. Shklovskii, J. Chem. Phys. **115**, 7298 (2001).

[64] R. R. Netz and J.-F. Joanny, Macromolecules **32**, 9026 (1999).

[65] K.-K. Kunze and R. R. Netz, Phys. Rev. Lett. **85**, 4389 (2000).

[66] H. Schiessel, R. F. Bruinsma, and W. M. Gelbart, J. Chem. Phys. **115**, 7245 (2001).

[67] R. J. Allen and P. B. Warren, Europhys. Lett. **64**, 468 (2003).

[68] R. J. Allen and P. B. Warren, Langmuir **20**, 1997 (2004).

[69] H. Holthoff, S. U. Egelhaaf, M. Borkovec, P. Schurtenberger, and H. Sticher, Langmuir **12**, 5541 (1996).

[70] S. H. Behrens, D. I. Christl, R. Emmerzael, P. Schurtenberger, and M. Borkovec, Langmuir **16**, 2566 (2000).

[71] F. Bouyer, A. Robben, W. L. Yu, and M. Borkovec, Langmuir **17**, 5225 (2001).

[72] W. Lin, P. Galletto, and M. Borkovec, Langmuir **20**, 7465 (2004).

[73] R. Pericet-Camara, G. Papastavrou, and M. Borkovec, Langmuir **20**, 3264 (2004).

[74] W.-F. Dong, J. K. Ferri, T. Adalsteinsson, M. Schönhoff, G. B. Sukhorukov, and H. Möwald, Chem. Mater. **17**, 2603 (2005).

[75] G. Decher and J. B. Schlenoff, editors, *Multilayer Thin Films* (Wiley-VCH, Weinheim, 2003).

[76] C. G. de Kruif, F. Weinbreck, and R. de Vries, Curr. Opin. Colloid Interface Sci. **9**, 340 (2004).

[77] A. Wittemann, B. Haupt, and M. Ballauff, Phys. Chem. Chem. Phys. **5**, 1671 (2003).

[78] R. Podgornik, T. Åkesson, and B. Jönsson, J. Chem. Phys. **102**, 9423 (1995).

[79] P. Welch and M. Muthukumar, Macromolecules **33**, 6159 (2000).

[80] M. Jonsson and P. Linse, J. Chem. Phys. **115**, 3406 (2001).

[81] M. Jonsson and P. Linse, J. Chem. Phys. **115**, 10975 (2001).

[82] T. Wallin and P. Linse, Langmuir **12**, 305 (1996).

[83] T. Wallin and P. Linse, J. Chem. Phys. **109**, 5089 (1998).

[84] A. Akinchina and P. Linse, Macromolecules **35**, 5183 (2002).

[85] T. Sakaue, K. Yoshikawa, S. H. Yoshimura, and K. Takeyasu, Phys. Rev. Lett. **87**, 078105 (2001).

[86] P. Chodanowski and S. Stoll, J. Chem. Phys. **115**, 4951 (2001).

[87] J. Dzubiella, A. G. Moreira, and P. A. Pincus, Macromolecules **36**, 1741 (2003).

[88] R. Messina, C. Holm, and K. Kremer, Langmuir **19**, 4473 (2003).

[89] R. Messina, C. Holm, and K. Kremer, Phys. Rev. E **65**, 041805 (2002).

[90] R. Messina, J. Chem. Phys. **117**, 11062 (2002).

[91] J. Kim, M. J. Serpe, and L. A. Lyon, J. Am. Chem. Soc. **126**, 9512 (2004).

[92] M. J. Serpe, J. Kim, and L. A. Lyon, Adv. Mater. **16**, 184 (2004).

[93] J. Kim, M. J. Serpe, and L. A. Lyon, Angew. Chem. Int. Ed. **44**, 1333 (2005).

[94] J. Kim, S. Nayak, and L. A. Lyon, J. Am. Chem. Soc. **127**, 9588 (2005).

[95] G. M. Torrie, J. P. Valleau, and G. N. Patey, J. Chem. Phys. **76**, 4615 (1982).

[96] M. Konieczny, C. N. Likos, and H. Löwen, J. Chem. Phys. **121**, 4913 (2004).

[97] M. J. Stevens and K. Kremer, Phys. Rev. Lett. **71**, 2228 (1993).

[98] G. S. Grest, K. Kremer, and T. A. Witten, Macromolecules **20**, 1376 (1987).

[99] G. S. Grest, Macromolecules **27**, 3493 (1994).

[100] A. Jusufi, J. Dzubiella, C. N. Likos, C. von Ferber, and H. Löwen, J. Phys.: Condens. Matter **13**, 6177 (2001).

[101] W. Essafi, F. Lafuma, and C. E. Williams, J. Phys. II (Paris) **5**, 1269 (1995).

[102] R. Messina, Macromolecules **37**, 621 (2004).

[103] J. Lekner, Physica A **176**, 485 (1991).

[104] G. S. Manning, J. Chem. Phys. **51**, 924 (1969).

[105] G. S. Manning, J. Chem. Phys. **51**, 934 (1969).

[106] G. S. Manning, J. Chem. Phys. **51**, 3249 (1969).

[107] T. Odijk and A. H. Houwaart, J. Polym. Sci. Polym. Phys. Ed. **16**, 627 (1978).

[108] R. G. Winkler, M. Gold, and P. Reineker, Phys. Rev. Lett. **80**, 3731 (1998).

[109] R. M. Nyquist, B.-Y. Ha, and A. Liu, Macromolecules **32**, 3481 (1999).

[110] J. Jiang, H. Liu, and Y. Hu, J. Chem. Phys. **110**, 4952 (1999).

[111] M. Deserno, C. Holm, and S. May, Macromolecules **33**, 199 (2000).

[112] E. Y. Kramarenko, A. R. Khokhlov, and K. Yoshikawa, Macromol. Theory Simul. **9**, 249 (2000).

[113] P. G. de Gennes, *Scaling Concepts in Polymer Physics* (Cornell University Press, Ithaca, 1979).

[114] M. Doi and S. F. Edwards, *The Theory of Polymer Dynamics* (Clarendon Press, Oxford, 1986).

[115] N. V. Brilliantov, D. V. Kuznetsov, and R. Klein, Phys. Rev. Lett. **81**, 1433 (1998).

[116] L. Harnau and P. Reineker, J. Chem. Phys. **112**, 437 (2000).

[117] Y. Kantor and M. Kardar, Phys. Rev. Lett. **83**, 745 (1999).

[118] F. S. Csajka and C. Seidel, Macromolecules **33**, 2728 (2000).

[119] J. D. Jackson, *Classical Electrodynamics*, 2nd ed. (Wiley, New York, 1975).

[120] W. K. H. Panofsky and M. Phillips, *Classical Electricity and Magnetism*, 2nd ed. (Addison-Wesley, Reading, MA, 1962).

[121] J.-P. Hansen and H. Löwen, Annu. Rev. Phys. Chem. **51**, 209 (2000).

[122] Y. Levin and M. E. Fisher, Physica A **225**, 164 (1996).

[123] M. N. Tamashiro, Y. Levin, and M. Barbosa, Physica A **258**, 341 (1998).

[124] T. T. Nguyen and B. I. Shklovskii, J. Chem. Phys. **114**, 5905 (2001).

[125] G. Gorodyska, A. Kiriy, S. Minko, C. Tsitsilianis, and M. Stamm, Nano Lett. **3**, 365 (2003).

[126] M. Konieczny and C. N. Likos, J. Chem. Phys. **124**, 214904 (2006).

[127] M. Konieczny and C. N. Likos, Macromol. Symp. **245-246**, 276 (2006).

[128] A. Fortini, M. Dijkstra, and R. Tuinier, J. Phys.: Condens. Matter **17**, 7783 (2005).

[129] J.-P. Hansen and I. R. McDonald, *Theory of Simple Liquids*, 2nd ed. (Academic Press, London, 1986).

[130] J. L. Lebowitz and J. S. Rowlinson, J. Chem. Phys. **41**, 133 (1964).

[131] F. J. Rogers and D. A. Young, Phys. Rev. A **30**, 999 (1984).

[132] T. Biben and J.-P. Hansen, J. Phys.: Condens. Matter **3**, 65 (1991).

[133] N. W. Ashcroft and D. Stroud, Solid State Phys. **33**, 2 (1978).

[134] C. N. Likos and N. W. Ashcroft, J. Chem. Phys. **97**, 9303 (1992).

[135] T. Biben and J.-P. Hansen, Phys. Rev. Lett. **66**, 2215 (1991).

[136] A. B. Bathia and D. E. Thornton, Phys. Rev. B **2**, 3004 (1970).

[137] J. Dzubiella, C. N. Likos, and H. Löwen, J. Chem. Phys. **116**, 9518 (2002).

[138] J. S. Rowlinson and F. L. Swinton, *Liquids and Liquid Mixtures* (Butterworth, London, 1982).

[139] N. F. Carnahan and K. E. Starling, J. Chem. Phys. **51**, 635 (1969).

[140] A. J. Archer, C. N. Likos, and R. Evans, J. Phys.: Condens. Matter **14**, 12031 (2002).

[141] C. Mayer, C. N. Likos, and H. Löwen, Phys. Rev. E **67**, 0414025 (2004).

[142] I. D'Amico and H. Löwen, Physica A **237**, 25 (1997).

[143] E. Allahyarov, I. D'Amico, and H. Löwen, Phys. Rev. Lett. **81**, 1334 (1998).

[144] E. Allahyarov and H. Löwen, J. Phys.: Condens. Matter **13**, L277 (2001).

[145] P. Attard, J. Chem. Phys. **91**, 3083 (1989).

[146] J. Dzubiella, C. N. Likos, and H. Löwen, Europhys. Lett. **58**, 133 (2002).

[147] J. M. Méndez-Alcaraz and R. Klein, Phys. Rev. E **61**, 4095 (2000).

[148] A. König and N. W. Ashcroft, Phys. Rev. E **63**, 041203 (2001).

[149] S. Mossa, F. Sciortino, P. Tartaglia, and E. Zaccarelli, Langmuir **20**, 10756 (2004).

[150] F. Sciortino, S. Mossa, E. Zaccarelli, and P. Tartaglia, Phys. Rev. Lett. **93**, 055701 (2004).

[151] R. P. Sear and W. M. Gelbart, J. Chem. Phys. **110**, 4582 (1999).

[152] A. Imperio and L. Reatto, J. Chem. Phys. **124**, 164712 (2006).

[153] A. Imperio and L. Reatto, J. Phys.: Condens. Matter **16**, 3769 (2004).

[154] R. L. C. Vink, A. Jusufi, J. Dzubiella, and C. N. Likos, Phys. Rev. E **72**, 030401(R) (2005).

[155] F. Lo Verso, D. Pini, and L. Reatto, J. Phys.: Condens. Matter **17**, 771 (2005).

[156] F. Lo Verso, R. L. C. Vink, D. Pini, and L. Reatto, Phys. Rev. E **73**, 061407 (2006).

[157] G. Gompper and M. Schick, Phys. Rev. B **41**, 9148 (1990).

[158] R. M. Hornreich, R. Liebermann, H. G. Schuster, and W. Selke, Z. Phys. B **35**, 91 (1979).

[159] R. van Roij and J.-P. Hansen, Phys. Rev. Lett. **79**, 3082 (1997).

[160] R. van Roij, M. Dijkstra, and J.-P. Hansen, Phys. Rev. E **59**, 2010 (1999).

[161] A. R. Denton, Phys. Rev. E **62**, 3855 (2000).

[162] P. R. ten Wolde and D. Frenkel, Science **277**, 1975 (1997).

[163] D. Frenkel, Physica A **263**, 26 (1999).

[164] M. Konieczny and C. N. Likos, J. Phys.: Condens. Matter **19**, 076106 (2007).

[165] J. Kleimann, G. Gehin-Delval, H. Auweter, and M. Borkovec, Langmuir **21**, 3688 (2005).

[166] A. Kiryi, G. Gorodyska, S. Minko, M. Stamm, and C. Tsitsilianis, Macromolecules **36**, 8704 (2003).

[167] F. A. Plamper, A. Walther, A. H. E. Müller, and M. Ballauff, Nano Lett. **7**, 167 (2007).

[168] H. M. Harreis, A. A. Kornyshev, C. N. Likos, H. Löwen, and G. Sutmann, Phys. Rev. Lett. **89**, 018303 (2002).

[169] A. Y. Grosberg, T. T. Nguyen, and B. I. Shklovskii, Rev. Mod. Phys. **74**, 329 (2002).

[170] A. Fernandéz-Barbero and B. Vincent, Phys. Rev. E **63**, 011509 (2000).

Acknowledgments

Herewith, I want to express my deepest gratitude to the various people who, during the last three years, contributed to the making of this thesis by their help and support.

First, I want to thank Prof. Dr. Christos N. Likos for the great opportunity to work with him. It was an enormous honor and a tremendous pleasure to have had him as my teacher and supervisor. His patient guidance and the innumerable, inspiring scientific discussions were invaluable in writing my thesis.

I am also very grateful to Prof. Dr. Hartmut Löwen for his support by numerous helpful suggestions, comments, and discussions.

I would like to thank Prof. Dr. Karl-Heinz Spatschek and Prof. Dr. Christoph Dellago for kindly accepting to referee this thesis.

I owe very special thanks to Dr. Norman Hoffmann and Dr. Christian Mayer for being marvelous colleagues and even better friends. They not only fundamentally supported my work with hints, comments and countless fruitful discussions, but it was also great fun sharing an office with them.

I also want express my thankfulness to all my other colleagues at the *Institut für Theoretische Physik II* for answering my multitudinous questions and for contributing to an excellent, more than pleasant working atmosphere. I always enjoyed working and spending coffee breaks with all of them. Moreover, I owe particular gratitude to Martin Rex and Sven van Teeffelen for critically reading the manuscript of the thesis and for various hints on how to improve it.

I want to thank Stephan Theiss for his worthwhile support during the last seven years, not only in the form of an interesting and challenging job, but also by his active help in many ways.

I thank Prof. Dr. Alexei A. Kornyshev for hosting me at his group at Imperial College London. The stay was a great learning experience.

I want to thank my friends for providing me with their support and for reminding me that there is a life beyond physics and work.

I am extremely grateful to my family. They supported my work on this thesis by being there for me. Their love and help always encouraged me.

Finally, I want to thank Astrid for her inestimable support, for enriching my life and making it happy every single day.

Die hier vorgelegte Dissertation habe ich eigenständig und ohne unerlaubte Hilfe angefertigt. Die Dissertation wurde in der vorgelegten oder in ähnlicher Form noch bei keiner anderen Institution eingereicht. Ich habe bisher keine erfolglosen Promotionsversuche unternommen.

Düsseldorf, den 14.03.2007

(Martin Konieczny)